Synthesis, Structure, and Proton Conductivity of Meta- and Pyrophosphates

Vajeeston Nalini

Dissertation for the degree of Doctor of Philosophy

2010

Functional Energy Related Materials in Oslo (FERMiO)
Centre for Materials Science and Nanotechnology (SMN)
Department of Chemistry
Faculty of Mathematics and Natural Sciences
University of Oslo
Norway

Series of dissertations submitted to the
Faculty of Mathematics and Natural Sciences, University of Oslo
No. 1001

ISSN 1501-7710

Cover: Inger Sandved Anfinsen.
Printed in Norway: AiT e-dit AS.

Produced in co-operation with Unipub.
The thesis is produced by Unipub merely in connection with the
thesis defence. Kindly direct all inquiries regarding the thesis to the copyright
holder or the unit which grants the doctorate.

Preface

This thesis is the product of the practical work for the degree of Doctor of Philosophy (PhD) at the Functional Energy Related Materials in Oslo, Centre for Materials Science and Nanotechnology, Department of Chemistry, University of Oslo (UiO), Norway. The experimental work has been carried out during the period of August 2005 to September 2009 under the supervision of Professors Truls Norby and Helmer Fjellvåg.

First of all I wish to express my gratitude to my supervisor, Professor Truls Norby for his unwavering encouragement and invaluable suggestions during this work. I would also like to include my gratitude to my co-supervisor, Professor Helmer Fjellvåg for his valuable support.

I express special thanks to Associate Professor Reidar Haugsrud, for his continuous support and fruitful discussion on scientific problems and results.

Furthermore I am deeply indebted to present and former fellow students and colleagues at the group for Solid State Electrochemistry at Functional Energy Related Materials in Oslo for their help and consistent support during experiments.

I deeply acknowledge the FUNMAT@UiO program at University of Oslo, Norway for the financial support.

Finally I want to thank my family. The encouragement and support from my beloved husband Vajeeston and our joyful children Yudhishtiran and Yashwini is a powerful source of inspiration and energy. A special thought is devoted to my parents and sister for a never-ending support. I also want to thank my relatives for their invaluable help for caring my father in critical situation and in turn helped me to continue my PhD programme without break.

Oslo, June 2010
Vajeeston Nalini

Table of Contents

Summary

The work constituting this thesis has mainly been focused on synthesis, structural and electrical characterization of undoped and acceptor doped LaP_3O_9 and tetra valent metal pyrophosphates MP_2O_7 (M = Ti, Zr and Sn). The poly-crystalline samples were prepared via traditional solid state method and by the phosphoric acid route. The samples prepared by conventional sintering were highly porous, and to increase the density, the spark plasma sintering method was applied for a few samples. A combination of techniques such as x-ray powder diffraction, neutron powder diffraction, scanning electron microscopy (SEM), transmission electron microscopy (TEM), thermogravimetry and impedance spectroscopy have been used to characterize the samples.

Structural investigation revealed that LaP_3O_9 is an orthorhombic structure and all the pyrophosphates are cubic superstructures at ambient temperature. The high temperature phase transition was observed in Ti and Sn pyrophosphates by neutron powder diffraction (NPD) and conductivity measurements. NPD results confirm that TiP_2O_7 undergoes a phase transformation at high temperature similar to Zr and Sn pyrophosphates. At low temperature, the material exists as a cubic superstructure with a unit cell parameter of 23.533(1) Å that upon arrival at 800 ^oC has transformed into a closely related high temperature modification with a smaller unit cell of 7.9641(3) Å.

The electrical conductivity was measured as a function of partial pressures of oxygen, water vapor and D_2O. Electrochemical impedance spectroscopy showed that the conductivity was due to grain interiors and that highly series-resistive grain boundaries can be excluded as a significant contribution to the overall conductivity. Acceptor doping appears not to be significant for the defect structures of pyrophosphate samples. Signs of abnormally high proton conductivities at low temperatures as reported in literature have not been observed.

The water vapor dependency and isotope effect confirmed that the conductivity was mainly protonic for all the measured phosphates and the $p(O)_2$-dependency indicated that the samples are mainly proton conductors under oxidizing conditions. n-type conductivity was observed for TiP_2O_7 and SnP_2O_7 in reducing atmospheres at high temperatures. The $p(H_2O)$ dependency of the conductivity of pyrophosphates has been modeled assuming that protons charge compensated by oxygen interstitials are the dominating defects. In ZrP_2O_7 proton conductivity was also confirmed by transport number measurements. The amount of

water uptake was observed by thermogravimetry, allowing extraction of parameters of the thermodynamics of hydration. This furthermore allowed calculation of proton mobility parameters. From thermogravimetry versus temperature at constant $p(H_2O)$ = 0.1 atm the standard entropy and enthalpy of hydration into protons and oxygen interstitials in Fe-doped TiP_2O_7 were found to be −147 ± 6 J/mol K and −40 ± 4 kJ/mol, respectively, at low temperature and −185 ± 13 J/mol K and −77 ± 15 kJ/mol, respectively, at high temperature. By combining thermodynamics from thermogravimetry and conductivity the apparent enthalpy of proton migration was $\Delta H_{m,H+}$ = 79 ± 3 kJ/mol at 500−700 °C and 61 ± 5 kJ/mol at 700−1000 °C, while the apparent mobility pre-exponential was $\mu_{0,H+}$ = 470 ± 150 cm^2 K/V s at low temperatures and 58 ± 30 cm^2 K/V s at higher temperatures. The change in the parameters between low and high temperature is assigned to the phase transformation. The standard hydration entropy and enthalpy of Sc-doped SnP_2O_7 were found to be −148 ± 5 J/mol K and −37 ± 5 kJ/mol, respectively. Using thermodynamics and conductivity data, the apparent enthalpy of proton migration and the apparent mobility pre-exponential were estimated to be 88 ± 3 kJ/mol and 38 ± 7 cm^2 K/V s, respectively at 500−900 °C.

The conductivity of metaphosphates was modeled assuming that the acceptor dopants are charge compensated by protons and oxygen vacancies. Modeling of the conductivity yields the standard hydration entropy and enthalpy associated with the dissolution of one mole of water: ΔS^0 = −100 ± 10 J/mol K and ΔH^0 = −70 ± 10 kJ/mol, respectively. The apparent enthalpy of proton migration comes out as $\Delta H_{m,H+}$ = 50 ± 5 kJ/mol and the apparent pre-exponential of mobility is $\mu_{0,H+}$ = 7 ± 3 cm^2 K/V s. Modeling of the TG data gives a standard hydration entropy of ΔS^0 = −110 ± 10 J/mol K and enthalpy ΔH^0 = −67 ± 10 kJ/mol. The hydration parameters of Sr-doped LaP_3O_9 are close to the entropy (−90 J/mol K) and enthalpy (−83 kJ/mol) changes of Sr-doped $LaPO_4$. Generally, hydration enthalpies become less negative with decreasing basicity. In accordingly, the magnitude of the exothermic hydration enthalpy of Sr-doped LaP_3O_9 is smaller than that of Sr-doped $LaPO_4$. In rare earth oxides the hydration parameters are moreover related to the stability of the materials. Compared to other oxides and rare earth phosphates, LaP_3O_9 is less stable and hydration enthalpy correspondingly less negative.

Chapter 1

Introduction

1.1 Background

Environmental concern is now driving the use of renewable and clean energy. Even with limited transmission lines the electric energy demands are ever increasing with many obstacles for new capacity and steady progress in power deregulation and utility restructuring to the distributed generation which is becoming ever more popular. Fuel cell power generation is expected to play a vital role because of several advantages such as reusability of exhaust heat, high efficiency, low environmental pollution, fuel diversity and modularity.

More than 160 years ago, the successful conversion of chemical energy into electrical energy in a primitive fuel cell was first demonstrated (*1*). However, in spite of the attractive system efficiencies and environmental benefits associated with fuel-cell technology, it has been proved to be difficult to develop the early scientific experiments into commercially viable industrial products. Those difficulties have often been associated with the lack of appropriate materials or manufacturing routes that would enable the cost of electricity per kWh to compete with the existing technology (*2*).

The types of fuel cells are described in Fig. 1.1 below. The alkaline fuel cell (AFC), polymeric-electrolyte-membrane fuel cell (PEMFC) and phosphoric-acid fuel cell (PAFC) stacks essentially require relatively pure hydrogen to be supplied to the anode. Accordingly, the use of hydrocarbon or alcohol fuels requires an external fuel processor to be incorporated into the system. This item increases the complexity as well as cost of the system and decreases the overall efficiency as shown in Fig. 1.2. In contrast, molten-carbonate fuel cells (MCFCs) and solid oxide fuel cells (SOFCs) operating at higher temperatures have the advantage that both CO and H_2 can be electrochemically oxidized at the anode. Moreover, the fuel-processing reaction can be accomplished within the stack,

which enables innovative thermal integration/management design features to provide excellent system efficiencies (~50%) (*3*).

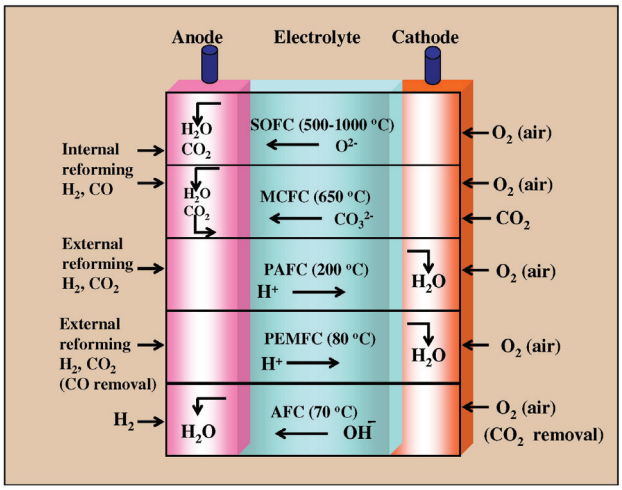

Fig. 1.1 Different types of fuel cells (*3*).

The fuels should be introduced directly into the anode compartment of the high-temperature fuel cells (SOFC and MCFC). For the better thermal management of the stack, separate reformer compartments have been used and these are thermally integrated within the stack to produce a mixture of fuel and syngas (H_2 and CO). For the lower-temperature

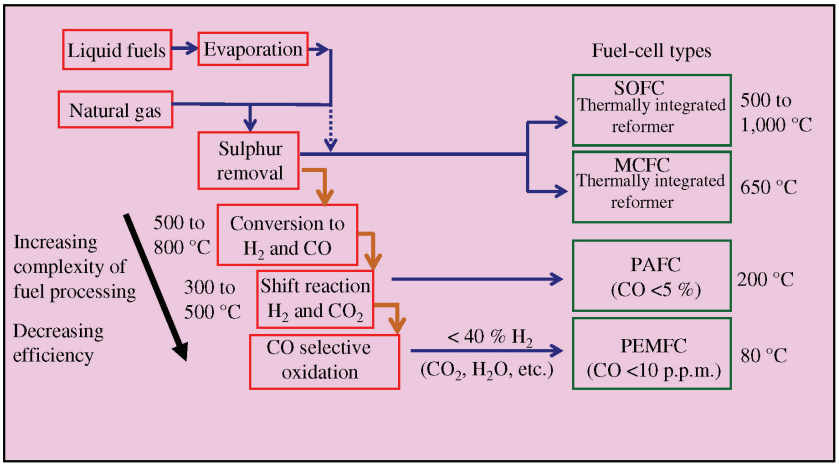

Fig. 1.2 Types of fuel cells and fuel processing (*3*).

fuel cells (PAFC and PEMFC), external reformers are required. Some of the fuel has to be consumed in these external reformers to maintain the operating temperature. Moreover, dilution of the H_2 fuel reduces performance of the cells, resulting in significant efficiency losses compared with operation on pure H_2.

1.2 Protonic ceramic fuel cell (PCFC)

This new type of fuel cell is based on a ceramic electrolyte material that exhibits high proton conductivity at elevated temperatures. PCFCs share the thermal and kinetic advantages of high temperature operation at 700 ^{o}C with molten carbonate and solid oxide fuel cells, while exhibiting all of the intrinsic benefits of proton conduction in PEM and phosphoric acid fuel cells. The high operating temperature is necessary to achieve very high electrical fuel efficiency with hydrocarbon fuels. PCFCs can operate at high temperatures and electrochemically oxidize fossil fuels directly to the anode. This eliminates the intermediate step of producing hydrogen through the costly reforming process. Gaseous molecules of the hydrocarbon fuel are absorbed on the surface of the anode in the presence of water vapor, and hydrogen atoms are efficiently stripped off to be absorbed into the electrolyte, with carbon dioxide as the primary reaction product. Additionally, PCFCs have a solid electrolyte so the membrane cannot dry out as with PEM fuel cells, or liquid can not leak out as with PAFCs. The operation principle in such a proton conductor based fuel cell is schematically shown in the figure below (Fig. 1.3).

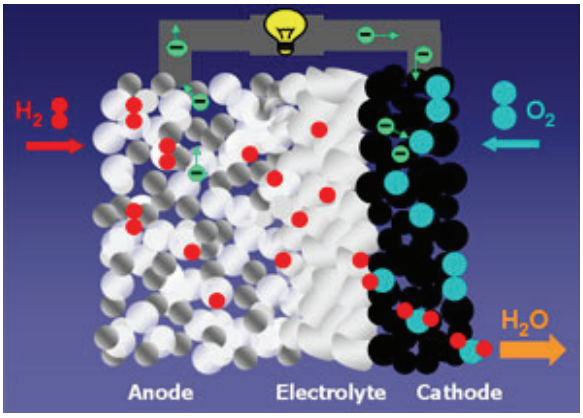

Fig. 1.3 Illustration of a protonic ceramic fuel cell (*4*)

Proton conducting electrolytes are also used in hydrogen sensors, hydrogen pumps, hydrogen gas controllers, steam electrolyzers, hydrogenation/dehydrogenation, and so on apart from the applications in fuel cells. Besides technological applications, proton conduction has an intrinsic part of life processing systems including photosynthesis of green plants. Mixed conducting materials are used in gas separation membranes.

1.3 Gas separation membranes

The gas separation membranes made by using proton and oxide ion conductors are mainly hydrogen and oxygen separation membranes. Hydrogen separation membranes extract hydrogen from mixtures of gases using a hydrogen partial pressure gradient as the driving force. This can be achieved using high pressure on the feed side and low pressure on the permeate side. Fig. 1.4 illustrates the utilization of the combined use of hydrogen and oxygen separation membranes in fossil fuel power plants. The air flowing inside the tubes becomes a $H_2 + N_2$ mixture ready for a fuel cell or gas turbine. The methane flowing in the outer chamber is transformed into CO_2, which can be dried and compressed for sequestration (*5*).

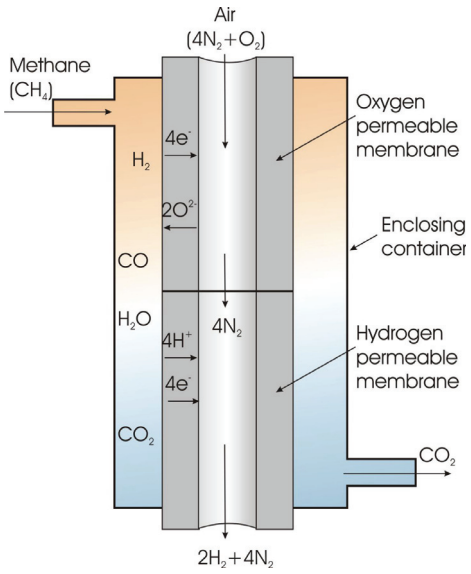

Fig. 1.4 Schematic representation of sequential use of mixed oxide ion-electron conductor for oxygen separation and mixed proton-electron conductor for hydrogen separation (*5*).

1.4 The present work

Motivation

Solid proton (H^+) conductors as electrolytes in fuel cells provide considerable advantages over aqueous or polymer H_3O^+ conductors because of higher operating temperature which results in cooling efficiency and higher heat value with less water management, less electrode poisoning, and overheat robustness. The research has been carried out for many years leading the discovery of protons and proton transport at high temperatures in materials with nominally no protons, e.g. many oxides. These works have been conducted mainly at temperatures around 600 ^oC and higher. The best material so far is barium cerate, $BaCeO_3$ (*6*). A gap from 200 to 600 ^oC exists between the low temperature proton conductors which contain water, and the high temperature proton conductors which are nominally free from protons. Finding a material with useful proton conductivity in this range would be extremely important for application developments.

The main aim of this study is to investigate materials with proton conductivities higher than 0.001 S/cm at some temperature between 200 and 700 ^oC, that have pure protonic or mixed protonic and electronic conduction, and that are stable in wet hydrogen as well as in air. The candidacy of materials follows certain strategies regarding presence and dynamics of protons and protonic defects, and an important scientific goal is to test these strategies and the models they are based on.

Many acidic alkali sulfate, selenate, phosphate, and arsenate salts have been identified as proton conductors (*7-10*). However, their temperature range of operation and stability are limited, as they are water soluble, and they are mechanically weak. Until now it remains a challenge to identify materials that combine sufficient proton conductivity and thermodynamic stability. Promising proton conductivity has been reported in phosphate based materials. Recently tetravalent metal pyrophosphates (MP_2O_7, M = Si, Ge, Sn, Ti, Zr and Ce) were reported to exhibit a remarkably high proton conductivity at intermediate temperatures (*11-15*). This has motivated us to study the proton conductivity in pyrophosphates in more detail. Moreover significant proton conductivity has been reported for rare earth metaphosphates, LnP_3O_9 (*16-18*). However, the defect structures of metaphosphates are not yet fully understood. In order to understand the defect structures in these metaphosphates we also include LaP_3O_9 in the present study.

The research presented in this thesis is focused on synthesis, structural investigation, proton conductivity and defect structure in phosphates, especially in LaP_3O_9 and tetravalent metal pyrophosphates (Ti, Zr and Sn).

Chapter 2

An overview of proton conducting oxidic materials

The field of proton conductors, or more precisely the effect of hydrogen on physical or chemical properties, emerged more than half a century ago. For example, in 1954 Mollwo (*19*) found that heating zinc oxide crystals in hydrogen changed the luminescent properties of the crystals and increased their conductivity. He obtained diffusion constants for the process, reported that the conductivity increased with the square root of the hydrogen pressure and obtained a value for the heat of solution of hydrogen in zinc oxide. Thomas and Lander (*20*) extended the work of Mollwo in 1956 and reported that hydroxyl groups are formed from the hydrogen and the lattice oxide ions. In 1958, Rudolph (*21*) found effects of hydrogen gas on the electrical conductivity of strontium-barium oxides. This was explained by the dissolution of hydrogen gas forming OH^- -ions on normal oxygen lattice sites with the positively charged protons as the charge carriers.

In 1967 Stotz and Wagner (*22*) developed a formalism for protonic defects in oxides. They stated that hydrogen in oxides would be ionized to protons and exist as interstitials with one positive effective charge in the structure, hence, contributing to the electroneutrality and conductivity of the sample. Later, Wagner (*23*) investigated ZrO_2 doped with Y_2O_3 and found that protons were taken up in the structure, but could not find any effect of this on the electrical properties. Later in the sixties and in the seventies hydrogen defects or effects of hydrogen activity were found in a number of oxides, such as TiO_2 (*24-26*), MoO_3 (*27*) and ThO_2 (*28*).

2.1 Proton conductivity in perovskite oxides

In 1974 Pope and Simkovich (*29*) applied a concentration cell method in order to explain the degradation of dielectric properties of $BaTiO_3$ in wet atmospheres. They found that different water vapor pressure on each side of the electrolyte gave rise to an EMF. This was the first report on mobile protonic species in perovskite-type oxides. But the real breakthrough came with Takahasi and Iwahara (*30*) when they in 1980 reported that the

conductivity in $La_{0.9}Ca_{0.1}YO_3$ and $SrCe_{0.95}In_{0.05}O_3$ was dominated by protons up to 800 ^oC in the presence of water vapor or hydrogen. Perovskite oxides such as $SrCeO_3$ (*31*) and $BaCeO_3$ (*6*) were the first oxides reported showing pure and high proton conductivity. The latter compounds, mainly 10 mol-% yttrium doped $BaCeO_3$ (conductivity = 10^{-2}–10^{-3} at 600−1000 ^oC) have remained the state-of-the art proton conducting material in oxides.

Proton conductivity in complex mixed perovskites with the general formulas, $A_2(B'B'')O_{6-\delta}$ and $A_3(B'B_2'')O_{9-\delta}$ have been investigated for more than a decade (*32, 33*). Among these complex phases the most promising proton conductivity ($\approx 10^{-3}$ S/cm at 300 ^oC) was found in $Ba_3Ca_{1.18}Nb_{1.82}O_{9-\delta}$ (BCN18) (*33-35*) and subsequently tested as an electrolyte in a lab-scale fuel cell (*36*). Other materials, such as $Ba_2YSnO_{6-\delta}$ (*37*), $Ba_2InSnO_{6-\delta}$ (*38*), $Sr_3CaZr_{0.5}Ta_{1.5}O_{9-\delta}$ (*39*) and $Sr_2(Sc_{1.1}Nb_{0.9})O_{6-\delta}$ (*33*) also show appreciable proton conductivity below 300 ^oC. In systems containing mixed ion, site ordering of these ions may cause formation of superstructures. Such supercells may limit the proton mobility and reduce proton conductivity (*40*). The degree of ordering, however, can be changed by introducing non-stoichiometry (*40*).

2.2 Proton conductivity in non-perovskites

Apart from perovskites there is a growing interest to develop new proton conducting materials. Recently some non-perovskite-structured oxides including rare earth orthoniobates and orthotantalates, $RE_{1-x}A_xMO_4$ (RE = La, Nd, Gd, Tb, Er and Y; A = Ca, Sr and Ba; x = 0.01−0.05; M = Nb and Ta) have been investigated. Among these samples, Ca-doped $LaNbO_4$ showed the highest proton conductivity ($\sigma_{H+} \approx 10^{-3}$ S/cm) below 800 ^oC in wet atmosphere (*41*) while in $La_{1-x}Ba_{1+x}GaO_{4-x/2}$ and $La_{1-x}Sr_{1+x}GaO_{4-x/2}$ (*42, 43*) the proton conductivity was, $\sigma_{H+} = 10^{-4}$ S/cm at ≈ 500−600 ^oC. Modest proton conductivity ($\sigma_{H+} \approx 10^{-5}$ S/cm at 400 ^oC) has been observed in the Brownmillerite phases $Ba_2In_2O_5$ (*44*) and $(Ba_{1-x}La_x)_2In_2O_{5+x}$ (*45*).

Proton conductivity in pyrochlore oxides were first discovered in the middle of 90's by Shimura et al. (*46*) in $Ln_2Zr_{2-x}Y_xO_{7-\delta}$ (Ln = La, Nd, Gd and Sm) samples and the reported proton conductivity was 10^{-3} S/cm at 800 ^oC under wet H_2 atmosphere. In addition to this, higher proton conductivity ($\sigma_{H+} \approx 10^{-2}$ S/cm at 600 ^oC) was obtained from dc four-probe method under wet H_2 atmosphere on Ca-doped $La_2Zr_2O_7$ (*47*).

Fluorite type structured $La_xWO_{3+1.5x}$ ($x \approx 6$) (*48*) and $Ce_{0.8}M_{0.2}O_{2-\delta}$ (M = Y, La, Sm and Gd) (*49*) have been reported to exhibit high proton conductivity, $\sigma_{H+} \approx 10^{-3}$–$10^{-2}$ S/cm at ≈ 650–900 °C under wet atmospheres. In contrast, significantly lower proton conductivity $\sigma_{H+} \approx 10^{-4}$ S/cm at ≈ 750 °C was obtained in some fluorite related structures (*50-52*).

2.3 Proton conducting phosphates

CsH_2PO_4 seems to be one of the most conductive compounds in a family of acid salts of alkaline metals with general formula $M_xH_y(AO_4)_z$ (M = Li, Na, K, Rb, Cs and NH_4; A = P, S, Se and As) (*53-57*). These solid acid salts undergo a superionic phase transition at 50–230 °C accompanied by a sharp increase in conductivity. The superionic phases exhibit general features due to the existence of a disordered hydrogen bond network. The range of CsH_2PO_4 superionic phase is limited as it decomposes under dry conditions to form $Cs_2H_2P_2O_7$, and conductivity decreases significantly at temperatures above 230 °C.

A number of rare earth phosphates, $LnPO_4$ (Ln = La, Ce, Pr, Nd and Sm) acceptor-doped with alkaline cations (*58-68*) have been reported to exhibit considerable proton conductivity, $\sigma_{H+} \approx 10^{-5}$–$10^{-3.5}$ S/cm, at 500–900 °C under wet atmosphere. Moreover the modest proton conductivity was reported in $Ba_3La(PO_4)_3$ (*69*). In addition reasonable proton conductivity has been reported in $Ba_3Ce(PO_4)_3$ (*70*) ($\sigma_{H+} \approx 1.5 \cdot 10^{-4}$ S/cm at 600 °C in wet H_2 atmosphere). Previously unrecognized amorphous grain boundary films are shown to provide rapid proton conduction paths in poly-crystalline lanthanum phosphates. Experiments revealed that the amorphous P-rich grain boundary films to be stable in air at 500 °C, with conductivity reaching $2.5 \cdot 10^{-3}$ S/cm at 500 °C, many orders of magnitude higher than in the crystalline bulk (*71*).

Followed by orthophosphates, significant proton conductivities have been reported for metaphosphates (YP_3O_9, LaP_3O_9 and GdP_3O_9) (*16-18*). Among these samples, orthorhombic Sr-doped LaP_3O_9 showed the highest proton conductivity ($\sigma_{H+} \approx 5 \cdot 10^{-3}$ S/cm) at 700 °C even under practically dry conditions (*16*) while in YP_3O_9 and GdP_3O_9 (*18*) the proton conductivities were, $\sigma_{H+} = 5 \cdot 10^{-6}$ and $6 \cdot 10^{-6}$ S/cm, respectively, at 700 °C in wet atmosphere. Proton conductivity has also been reported in $Ca(PO_3)_2$ and it was identified as candidate material for humidity sensors (*72*).

Nagao et al. (*11, 12, 15*) recently reported very high proton conductivities in tetra valent metal (Si, Ti, Ge and Sn) pyrophosphates synthesized by the phosphoric acid route. Among these materials, In^{3+} doped tin pyrophosphate showed the highest proton conductivity ($\sigma_{H+} \approx 10^{-2}$–$10^{-1}$ S/cm at 250 ^{o}C even under dry atmosphere). Moreover, high proton conductivity was reported in CeP_2O_7 ($\sigma_{H+} = 10^{-2}$ S/cm at 250 ^{o}C) and 5 mol-% Y-doped ZrP_2O_7 ($\sigma_{H+} = 1.5 \cdot 10^{-4}$ S/cm at 340 ^{o}C) (*13, 14*). In sharp contrast to these findings, Tao (*73*) reported significantly lower proton conductivity ($\sigma_{H+} = 6.5 \cdot 10^{-6}$ S/cm at 900 ^{o}C) in In^{3+} doped tin pyrophosphate prepared by an aqueous solution method (*73*).

Chapter 3

Theory and background

This chapter contains the theoretical background of point defect chemistry, and describes the defect structures of oxides in general and of phosphates specifically. The defect structure of orthophosphates as described in literature is first presented, before the defect structure of meta- and pyrophosphates derived in this study is outlined. This is followed by the theoretical background for the experimental techniques.

3.1 Defect chemistry

A perfect crystal may be defined as one in which all the atoms are at rest in their correct lattice positions (*74*). A perfect crystal may hypothetically be obtained at absolute zero; at real temperatures all crystals are imperfect. Recently, it has been realized that many interesting physical properties of solids are controlled by faults or defects in the crystal structures (*75*). Indeed both the physics and chemistry of the solids are decisively influenced by the defects that occur in the materials.

Defects can be broadly divided into two classes, giving rise to stoichiometric and non-stoichiometric compounds.

3.1.1 Defects in stoichiometric compounds

If we consider a stoichiometric system the crystal composition is unchanged when introducing defects. Generally, two types of defects are found in stoichiometric ionic inorganic solids, namely, Schottky and Frenkel defects.

3.1.1.1 Schottky defects

Schottky defect is a type of point defect in a crystal lattice named after Walter H. Schottky. The defect forms when oppositely charged ions leave their lattice sites, creating vacancies. These vacancies are formed in stoichiometric units (Fig. 3.1a), to maintain an overall neutral charge in the ionic solid. For example, if a cation is removed from its lattice site, in order to maintain the charge balance, an anion must be removed from its lattice site or vice-versa. The vacancies are then free to move about as their own entities. Each vacancy is a separate Schottky defect. Normally these defects will lead to a decrease in the density of the crystal. This type of defect is commonly found in low concentrations in alkali metal halides (*74*).

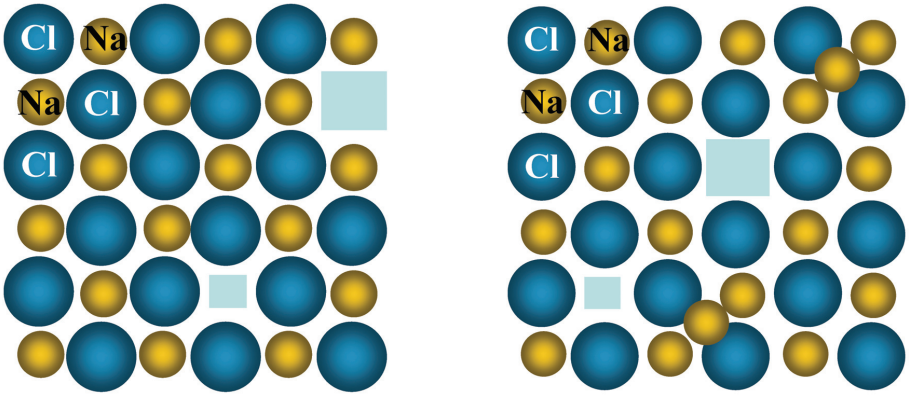

Fig. 3.1 (a) Schottky defects in NaCl (b) Cation Frenkel defects in NaCl

3.1.1.2 Frenkel defects

A Frenkel defect, also called a Frenkel pair or Frenkel disorder, is a compound crystallographic defect in which an interstitial lies near the vacancy. A Frenkel defect forms when an atom or ion leaves its place in the lattice (leaving a vacancy), and lodges nearby in the crystal (becoming an interstitial). For example, consider a lattice formed by X and M ions. Suppose an M ion leaves the M sublattice, leaving the X sublattice unchanged. The number of interstitials formed will equal the number of vacancies formed. This can be illustrated with the example of sodium chloride (Fig. 3.1b). It arises when an

ion is missing from its normal position and occupies an interstitial site between the lattice points.

Although Schottky and Frenkel disorder may be simultaneously present in stoichiometric compounds, one type of disorder usually predominates. As a rough rule Schottky disorder is favored in crystals where the cations and anions are of comparable size, while Frenkel disorder predominates when the sizes of the cations and anions are appreciably different. Another factor is that Schottky disorder tends to dominate when the structure is very effectively packed so that the interstitials that are part of Frenkel pairs are hard to form. Both Schottky and Frenkel defects are intrinsic defects because they are present in pure material and a certain minimum number must be present from thermodynamic considerations.

3.1.2 Defects in non-stoichiometric compounds

Non-stoichiometric compounds are chemical compounds with an elemental composition that cannot be represented by a ratio of well-defined natural numbers, and therefore violate the law of definite proportions. Often, they are solids that contain crystallographic point defects that result in the excess or deficiency of an element. Since solids are overall electrically neutral, the defects are compensated by a change in the charge of other atoms in the solid, either by changing their oxidation state, or by replacing them with atoms of different elements with a different charge (*75*). Non-stoichiometric systems can be formed by introducing dopants or impurities. Such defects, occurring in non-stoichiometric compounds, are sometimes denoted as extrinsic defects. In this case, the dopants either occupy interstitial sites or substitute for atoms or ions in the parent lattice. For example, by partial substitution of higher valence cations for lower valence host cations, cation vacancies or interstitial anions will form and the higher valence cation is called a donor-dopant. In contrast, by exchange of higher valence cations with lower valence cations, one can create oxygen vacancies or electronic holes as charge compensating defects in the dry state and in this case the substitute cation is called an acceptor-dopant. Non- stoichiometric defects are illustrated in Fig. 3.2.

In order to describe defects in a short way, and to include vacancies when writing chemical formulas and setting up e.g. equilibrium conditions, it is necessary to have a notation which is simple and self consistent. The Kröger-Vink notation is widely used and the following Table 3.1 summarizes the notation (*76*):

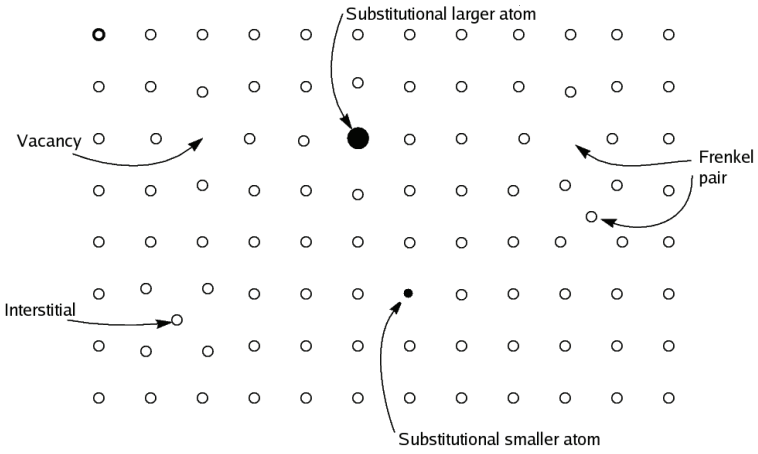

Fig. 3.2 Defects can cause solids to be non-stoichiometric.

Table 3.1 Summary of the Kröger-Vink notation.

Defect type	Notation	Defect type	Notation
Non-metal vacancies at non metal site	v_X	Impurity non-metal (Y) at non-metal site	Y_X
Metal vacancies at metal site	v_M	Impurity metal (A) at metal site	A_M
Neutral vacancies	v_M^x v_X^x	Non-metal vacancies with positive effective charge*	$v_X^\bullet$
Metal vacancies with negative effective charge*	$v_M^/$	Interstitial metal	M_i
Interstitial non-metal	X_i	Interstitial metal with positive effective charge*	$M_i^\bullet$
Interstitial non-metal with negative effective charge*	$X_i^/$	Free positive hole	$h^\bullet$
Free electron	$e^/$	Substitutional hydroxide	$OH_O^\bullet$

*The effective charge is the charge that the defect has with respect to the normal crystal lattice.

3.2 Formation of defects and equilibrium reactions

The defect structures in stoichiometric compounds contain equivalent concentrations of negatively and positively charged point defects. These are formed as a result of internal equilibrium in the crystal and do not involve reactions with the surroundings. For this reason the defect structures in stoichiometric compounds are also termed internal disorder.

3.2.1 Intrinsic defect reactions

As described earlier, the Schottky disorder involves the presence of equivalent amounts of cation and anion vacancies. In an oxide MO this means that the crystal contains equal concentrations of metal and oxygen vacancies. The overall formation of such a defect pair within the crystal involves the transfer of a pair of cations and anions on regular lattice sites from the bulk to the surface. In reality the defects are formed at external and internal surfaces or dislocations and subsequently diffuse into the crystal until they are randomly distributed. The formation of Schottky-defects may be written

$$M_M + O_O = v_M'' + v_O^{\bullet\bullet} + M_M + O_O \tag{3.1}$$

However, in this equation M_M and O_O on both sides may be cancelled, and the net equation therefore becomes

$$0 = v_M'' + v_O^{\bullet\bullet} \tag{3.2}$$

where 0 (nil) designates a perfect crystal.

For the Frenkel disorder the predominant defects are either limited to the cations and anions, and the disorder involves the presence of equal numbers of vacancies and interstitial ions in a sublattice in a crystal. In the formation of a Frenkel defect pair, a cation on a normal site is transferred to an interstitial site, and no new lattice sites are created in the process. If, the interstitial ion and the resulting vacancy are assumed to be doubly charged, the formation of a Frenkel defect pair may be written

$$M_M = v_M^{//} + M_i^{\bullet\bullet} \tag{3.3}$$

3.2.1.1 Intrinsic ionization of electrons

The excitation of an electron from the valence band to the conduction band, thereby leaving an electron hole in the valence band, is written

$$0 = e^{/} + h^{\bullet} \tag{3.4}$$

The electronic defects may be localized. In these cases the reactions are connected with individual atomic sites. For instance the intrinsic ionization of Fe^{3+} ions into Fe^{2+} and Fe^{4+} ions would be written

$$2Fe_{Fe}^{x} = Fe_{Fe}^{\bullet} + Fe_{Fe}^{/} \tag{3.5}$$

3.2.2 Extrinsic defect reactions

Extrinsic defect reactions deal with possible interactions between the sample and the surrounding atmosphere. Oxygen vacancies are created when oxygen in regular lattice sites are released to the surrounding gas phase

$$O_O^x = v_O^{\bullet\bullet} + 2e^{/} + \tfrac{1}{2}O_{2(g)} \tag{3.6}$$

If excess oxygen is taken up from the gas phase, oxygen interstitials are created

$$\tfrac{1}{2}O_{2(g)} = O_i^{//} + 2h^{\bullet} \tag{3.7}$$

If Eqs. (3.6) and (3.7) are combined they are reduced to the anion Frenkel disorder. Oxides which are nominally free of hydrogen may form hydrogen containing defects if exposed to a hydrogen containing atmosphere. The formation of interstitial protons from water vapor may, for an oxide nominally dominated by oxygen vacancies, be expressed by

$$H_2O_{(g)} + v_O^{\bullet\bullet} + 2O_O^x = 2OH_O^{\bullet} \quad (3.8)$$

Another type of extrinsic defect is formed when a metal sub-lattice is partly filled with metal ions of another element. It may be a result of impurities or a deliberate action, i.e. doping. The introduction of either lower valence elements or higher valence elements are termed acceptor and donor doping, respectively, and may drastically alter the defect structure. The acceptor doping of an oxygen deficient metal oxide (MO_{2-x}) with lower valent metal oxide (Ml_2O_3) may be described by

$$Ml_2O_3 = 2Ml_M^{/} + v_O^{\bullet\bullet} + 3O_O^x \quad (3.9)$$

3.3 Protonic defects and their transport

A proton is an elementary positive particle with radius of only 10^{-15} m (10^5 times smaller than any other chemical species). Protons cannot persist in the free state in a chemical environment, but are attracted into nearby electron clouds. In oxides and other oxidic materials, such an attraction will lead to formation of the hydroxide ion, OH^-. As such, the proton residing on a normal oxygen ion can be considered as an interstitial proton, $H_i^{\bullet}$ (but with the interstitial site strongly displaced towards a particular oxygen ion) or as a substitutional hydroxide ion, $OH_O^{\bullet}$. Protons may be transported in two distinctly different ways; as separate species ("free" proton transport) or as passengers on mobile host species (vehicle mechanisms).

Protons can migrate in the form of larger species (e.g. H_3O^+), which is commonly called a vehicle mechanism (*77*). Some variants of the vehicle mechanism generally dominate in aqueous solution, in other liquids or in melts. In solids, a vehicle mechanism is usually to be expected in open structures (channels, layers etc) where large ions and molecules can pass easily (e.g. SiO_2, β-Al_2O_3 etc) (*78*). In the tightly packed oxides and phosphates, proton transfer takes place by the so called Grotthuss mechanism (free proton transport), which consists of two-steps, a proton transfer between the neighboring oxygen sites followed by a reorientation of hydroxide ions (*77*). A schematic picture of the Grotthuss mechanism is shown in Fig. 3.3. The proton is the only mobile specie while the

oxygen ion is localized at its crystallographic position. The rotation and reorientation are believed to involve small activation energies and the jump itself is considered to be the rate-determining step.

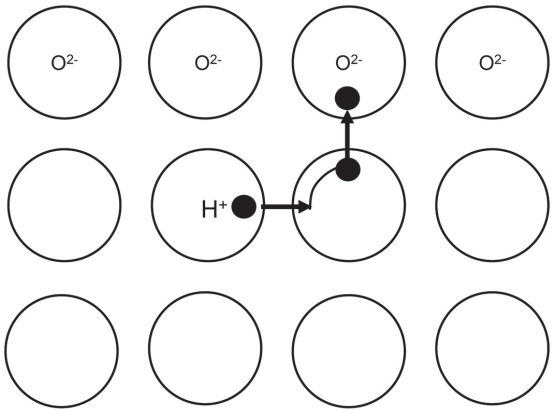

Fig. 3.3 Schematic illustration of free proton transport (Grotthuss mechanism) (*79*).

3.4 Mobility of protons

The mobility of protons in the materials was investigated by studying the effect of replacing water with deuterium dioxide (D_2O) on the conductivity (commonly referred to as "the isotope effect"). In a pure proton conductor with a constant concentration of protons, the conductivity shows Arrhenius behavior of the form:

$$\sigma T = \mathrm{A}\exp(\frac{-\mathrm{E}}{kT}) \tag{3.10}$$

with A being the pre-exponential and E the activation enthalpy for proton jumps. The large hydrogen-to-deuterium conductivity ratio (~2.8) reported by Lee et al. (*80*) on Cu^{2+} and Fe^{3+}-doped $KTaO_3$, gave clear evidences that conduction is due to simple proton hopping and not to migration of a vehicle such as OH^-. If the latter had been the case, the ratio of the conductivities would be nearly unity, since the mass ratio of OD^- and OH^- is very close to unity. The classical isotope effect will only affect the pre-exponential A as this term contains the mass of the transported species ($A_D/A_H = \sqrt{2}$). But in a quantum mechanical

treatment of the zero-point energies of charge carriers, the activation enthalpy for the deuteron is expected to be ~0.055 eV higher than for the proton, as commonly observed experimentally.

Slade and Singh (*81*) measured the isotope effect of Y and Gd doped $BaCeO_3$ at 600 to 900 ^oC and found an even greater difference in the activation enthalpies (0.131 and 0.086 eV for Y and Gd doped, respectively). This was tentatively interpreted in terms of tunneling conduction, which would favor proton conductivity. However, Bonanos (*82*) pointed out that their measurements were done in the very temperature interval were the conductivities shifts from being purely protonic to being affected by oxygen ions. Taking into account that the protonic component of the total conductivity is reduced when exchanging with deuterons and that the oxygen ion component is unaltered, Bonanos (*82*) showed that the high activation enthalpy differences could be explained within the classical model.

Nowick and Vaysleyb (*83*) reviewed the isotope effect of $KTaO_3$, $SrCeO_3$, $SrZrO_3$ and some mixed perovskites. It was pointed out that under frozen-in conditions; all conductivity data showed a strict Arrhenius behavior (Eq. (3.10)). The hydrogen-deuterium conductivity ratio (σ_H/σ_D) ranged from ~1.5 to ~3.5, while the ratio of the pre-exponentials (A_H/A_D) was found generally to be slightly lower than 1 (contrary to the classical value of $\sqrt{2}$ arising from the difference in mass of the two isotopes). The large σ_H/σ_D were explained by the use of a semi-classical theory, introducing different zero-point energies for the O-H and O-D vibrations. As mentioned earlier this gives a difference of the activation enthalpy for deuteron and proton jumps of $\Delta E = E_D - E_H \approx 0.055$ eV. This was found to coincide qualitatively with the experiments showing differences of 0.02−0.06 eV. The deviation from the $\sqrt{2}$ value for the A_D/A_H could be qualitatively explained by expanding the semi-classical approach with quantum vibrational partition functions as shown by Bell (*84*). The value of A_D/A_H would then be in the range $½ < A_H/A_D < \sqrt{2}$, with a strong probability of being close to unity. Within the experimental uncertainties the so-called "escape theory" also proved to give a satisfactory explanation of the experimental results. In contrast to the semi-classical theory this theory considers the microscopic collision processes of the jumping atom. The energy of the proton is assumed modified by quasi-elastic collisions with the surrounding atoms (cage). Considering a range of interactions between the proton and the surrounding cage, one might expect $1/\sqrt{2} < A_H/A_D < 1$, which were also found to agree with experimental results (*83*).

Furthermore, the escape theory effect involves pre-exponentials of diffusion of about one order of magnitude lower than the classically predicted values. This may explain the apparent discrepancies between measured and expected proton conductivities that have tended to be interpreted as a result of lower-than-expected concentration of mobile protons (e.g. ref. (*85*)).

3.5 Diffusivity, mobility and conductivity; The Nernst-Einstein relation

For species with an activated diffusion, the self-diffusion coefficient *D*, mechanical mobility *B*, charge mobility *u*, and conductivity σ are linked through the Nernst-Einstein relation

$$\sigma_i = z_i F c_i u_i = (z_i F)^2 c_i B_i = \frac{(z_i F)^2 c_i D_i}{RT} \tag{3.11}$$

where $D = D_0 \exp\frac{-E}{RT}$ defines the temperature dependence and activation energy E. The Faraday constant F = 96485 C/mol, expressing the charge per mole of charges, and the defect concentration c_i must thus be brought into the form of a molar volume concentration.

3.6 Conductivity

The conductivity of a material is commonly measured at high temperatures in isotherms or isobars. AC 2-electrode measurements on disks can yield the sample conductivity if the frequency is high enough that the electrode polarization is eliminated. Impedance spectroscopy can give more information, both to ensure that one is not the victim of parasitics or artifacts and in some cases to deconvolute the impedance of the sample into contributions from grain interior, grain boundaries, and electrodes. Impedance spectroscopy can reveal the resistance across grain boundaries, but it cannot give information about parallel conductivity along grain boundaries.

The total conductivity is

$$\sigma = \sum_{i} \sigma_i = \sum_{i} z_i F c_i u_i \tag{3.12}$$

where z_i is the number of charges of the carrier i, c_i is its concentration (in mol/cm^3) and u_i is its charge mobility in cm^2/V s. As mentioned before, the concentration c_i can be calculated from the mole fraction of the carrier and the molar density of the material: $c_i = [i]d_{M,i}$. For diffusing species (ions or ionic defects, including protons, and small polaron electronic carriers) the charge mobility μ_i is given as

$$\mu_i = \mu_{0,i} \frac{1}{T} \exp\left(\frac{-\Delta H_{m,i}}{RT}\right) \tag{3.13}$$

The mobility of the electronic defects may be treated according to the band-structure of the compound. It is common to divide the mobilities of the electronic defects into three classes, depending on their temperature dependencies. Free- or band-type mobility occurs in so-called broad bands. Such mobilities are relatively high, and show negative temperature dependencies. For the large polaron mechanism the electrons or hole creates and are themselves trapped by shallow lattice distortions. This mechanism is often found for intermediate mobilities. Also for this mechanism the mobility decreases with increasing temperature. The small polaron hopping mechanism describes the migration of electrons when there are deep traps at localized sites in the lattice. The migration then involves an activated process, for which the Nernst-Einstein relation ship applies, and Eq. (3.13) expresses the temperature dependences. Conductivity measured vs T and $p(H_2O)$ can give information about the mobility as well as hydration thermodynamics if one can properly apply the defect model at play and assign the total conductivity to contributions from the relevant charge carriers. Conductivity vs $p(O_2)$ is less informative in this respect, but can help deconvolute the total conductivity into electronic and ionic parts, as the ionic part (including the protonic) is usually $p(O_2)$-independent while the electronic ones have $p(O_2)$-dependencies.

3.7 Defect structures of proton-conducting oxides

When hydrogen dissolves in oxides, it forms $OH_O^{\bullet}$ which is the charge carrier that gives the proton conductivity. The simplest case would be to dissolve protons compensated by electrons originating directly from hydrogen gas.

$$H_{2(g)} + 2O_O^x = 2OH_O^{\bullet} + 2e^{/}; \qquad K_{2H2e} = \frac{[OH_O^{\bullet}]^2 n^2}{p(H_2)[O_O^x]^2} \tag{3.14}$$

This reaction was reported for ZnO (*20*), and it was found that protons and electrons are the dominating defects in hydrogen atmospheres, so that the electroneutrality condition and concentrations are expressed as

$$[OH_O^{\bullet}] = n = K_{2H2e}^{1/4} p(H_2)^{1/4} [O_O^x]^{1/2} \tag{3.15}$$

It may be shown that one may only hope to achieve this situation when the material is already dominated by electrons (and some positive point defects, such as oxygen vacancies) under hydrogen-free reducing conditions. By increasing $p(H_2)$, the native positive defects are replaced by the protonic ones. Protons compensated by electrons are, however, hardly known in systems other than ZnO, and instead one tends to use acceptor-doped oxides in which the concentrations of protons and all other positive defects are enhanced by the doping. The acceptors are most often substitutionally dissolved lower-valent cations, while, in principle, interstitial anions or substitutional higher-valent anions (e.g. N^{3-} substituting O^{2-}) can also be used. The acceptor is represented as $A^{/}$.

Assuming that the acceptors are compensated by oxygen vacancies in the absence of hydrogen-containing gases, the reaction with water vapor is given by

$$H_2O(g) + v_O^{\bullet\bullet} + O_O^x = 2OH_O^{\bullet}; \quad K = \exp\frac{\Delta S^0}{R}\exp\frac{-\Delta H^0}{RT} = \frac{[OH_O^{\bullet}]^2}{[v_O^{\bullet\bullet}][O_O^x]p(H_2O)} \tag{3.16}$$

The equilibrium constant, *K*, for the reaction, and the limiting electroneutrality condition

$$2[\mathrm{v}_{\mathrm{O}}^{\bullet\bullet}] + [\mathrm{OH}_{\mathrm{O}}^{\bullet}] = [\mathrm{A}^{/}] = \text{constant} \tag{3.17}$$

yield (assuming $[\mathrm{v}_{\mathrm{O}}^{\bullet\bullet}] + [\mathrm{OH}_{\mathrm{O}}^{\bullet}] << [\mathrm{O}_{\mathrm{O}}^{x}] \approx [\mathrm{O}]$) a simplified expression for $[\mathrm{OH}_{\mathrm{O}}^{\bullet}]$

$$[\mathrm{OH}_{\mathrm{O}}^{\bullet}] = \frac{[\mathrm{O}]Kp(\mathrm{H_2O})\left(-1+\sqrt{1+\dfrac{8[\mathrm{A}^{/}]}{[\mathrm{O}]Kp(\mathrm{H_2O})}}\right)}{4} \tag{3.18}$$

where [O] is the concentration of oxygen sites. From this, and knowing the equilibrium constant K (or better ΔS^0 and ΔH^0), the dependences on temperature, $p(\mathrm{H_2O})$, and acceptor concentration $[\mathrm{A}^{/}]$ can be calculated. Further, concentrations of other defects can be calculated from the electroneutrality condition or from equilibrium with protons.

$$[\mathrm{v}_{\mathrm{O}}^{\bullet\bullet}] = \frac{[\mathrm{A}^{/}] - [\mathrm{OH}_{\mathrm{O}}^{\bullet}]}{2} \tag{3.19}$$

where $[\mathrm{OH}_{\mathrm{O}}^{\bullet}]$ is inserted from Eq. (3.18). The concentration of defect electrons is in turn obtained from their equilibrium with oxygen vacancies, or from their equilibrium (Eq. (3.14)) with hydrogen above, to become

$$\mathrm{n} = \frac{K_{2\mathrm{H2e}}^{1/2} p_{\mathrm{H_2}}^{1/2}[\mathrm{O}]}{[\mathrm{OH}_{\mathrm{O}}^{\bullet}]} = \frac{K_{2\mathrm{H2e}}^{1/2} p_{\mathrm{H_2O}}^{1/2}[\mathrm{O}]}{K_{\mathrm{H_2O}}^{1/2} p_{\mathrm{O_2}}^{1/4}[\mathrm{OH}_{\mathrm{O}}^{\bullet}]} \tag{3.20}$$

where, again, $[\mathrm{OH}_{\mathrm{O}}^{\bullet}]$ is inserted from Eq. (3.18). Finally, the concentration of electron holes, p, is found from the intrinsic electronic ionization equilibrium as $\mathrm{p} = K_{\mathrm{in}}/\mathrm{n}$.

In some acceptor-doped materials, electron holes may also become dominating defects at high oxygen activities, so that the electroneutrality is expressed as

$$2[\mathrm{v}_{\mathrm{O}}^{\bullet\bullet}] + [\mathrm{OH}_{\mathrm{O}}^{\bullet}] + \mathrm{p} = [\mathrm{A}^{/}] = \text{constant} \tag{3.21}$$

A situation with all these three positively charged defects being important in compensating the acceptors may possibly be found in some perovskites. The solution to the

defect concentrations becomes complex, but can be brought into analytical form. The lack of practical importance leads us instead to limit ourselves to the more common case in which electron holes alone compensate the acceptors

$$\mathrm{p} = [\mathrm{A}^{/}] = \text{constant} \tag{3.22}$$

whereby, via Eq. (3.14) and $K_{\mathrm{in}} = \mathrm{n}\cdot\mathrm{p}$, the minor concentration of protons becomes

$$[\mathrm{OH}_{\mathrm{O}}^{\bullet}] = \frac{K_{2\mathrm{H2e}}^{1/2} p(\mathrm{H}_2)^{1/2}[\mathrm{O}][\mathrm{A}^{/}]}{K_{\mathrm{in}}} \tag{3.23}$$

3.8 Defect structures of proton-conducting orthophosphates

In orthophosphates such as $LaPO_4$, acceptor substitution and hydration are believed to involve oxygen deficiency in the form of a pyrophosphate ion defect located over two adjacent orthophosphate ion sites, $(\mathrm{P_2O_7})_{2\mathrm{PO_4}}^{\bullet\bullet}$, and hydrogen phosphate groups at orthophosphate ion sites, $(\mathrm{HPO_4})_{\mathrm{PO_4}}^{\bullet}$ (*62*),

$$\frac{1}{2}\mathrm{M_2P_2O_7} \rightarrow \mathrm{M}_{\mathrm{Ln}}^{/} + \frac{1}{2}(\mathrm{P_2O_7})_{2\mathrm{PO_4}}^{\bullet\bullet} \tag{3.24}$$

$$\frac{1}{2}(\mathrm{P_2O_7})_{2\mathrm{PO_4}}^{\bullet\bullet} + \frac{1}{2}\mathrm{H_2O(g)} = (\mathrm{HPO_4})_{2\mathrm{PO_4}}^{\bullet} \tag{3.25}$$

$$K_1 = \left[(\mathrm{HPO_4})_{2\mathrm{PO_4}}^{\bullet}\right]\left[(\mathrm{P_2O_7})_{2\mathrm{PO_4}}^{\bullet\bullet}\right]^{\frac{-1}{2}} p(\mathrm{H_2O})^{\frac{-1}{2}} \tag{3.26}$$

Considering Eqs. (3.24) and (3.25), one can say the situation is similar to one found in many acceptor doped proton conducting oxides (*77, 86, 87*). That is, $(\mathrm{P_2O_7})_{2\mathrm{PO_4}}^{\bullet\bullet}$ plays a similar role as oxygen vacancies in oxides, while $(\mathrm{HPO_4})_{2\mathrm{PO_4}}^{\bullet}$ corresponds to interstitial protons (or hydroxide ions). In dry atmosphere and higher temperatures, $P_2O_7^{4-}$ and PO_4^{3-}

may have the same equilibrium with oxygen gas as oxygen vacancies and oxide ions have in oxides:

$$\frac{1}{2}(\mathrm{P_2O_7})^{\bullet\bullet}_{2\mathrm{PO_4}} + \frac{1}{4}\mathrm{O_{2(g)}} \rightarrow (\mathrm{PO4})^{\mathrm{x}}_{\mathrm{PO4}} + \mathrm{h}^{\bullet} \tag{3.27}$$

$$K_2 = \mathrm{p}\left[(\mathrm{P_2O_7})^{\bullet\bullet}_{2\mathrm{PO_4}}\right]^{\frac{-1}{2}}\left[(\mathrm{PO4})^{\mathrm{x}}_{\mathrm{PO4}}\right]p(\mathrm{O_2})^{\frac{-1}{4}} \tag{3.28}$$

where p denotes the concentration of electron holes.

If we assume only $P_2O_7^{4-}$ and HPO_4^{2-} are dominant positive defects and electronic defects are present in minor concentrations, the electroneutrality condition can be approximated by:

$$\left[(\mathrm{HPO_4})^{\bullet}_{\mathrm{PO_4}}\right] + 2\left[(\mathrm{P_2O_7})^{\bullet\bullet}_{2\mathrm{PO_4}}\right] = \left[\mathrm{Sr}^{/}_{\mathrm{La}}\right] = \text{constant} \tag{3.29}$$

The concentration of each defect can be derived from Eqs. (3.26), (3.28) and (3.29) with the knowledge of the doping level and the values of the equilibrium constants. When hydrogen phosphate groups are dominant defects, the concentrations of the defects can be expressed as follows:

$$\left[(\mathrm{HPO_4})^{\bullet}_{\mathrm{PO_4}}\right] = \left[\mathrm{Sr}^{/}_{\mathrm{La}}\right] \tag{3.30}$$

$$\left[(\mathrm{P_2O_7})^{\bullet\bullet}_{2\mathrm{PO_4}}\right] = K_1^{-2}\left[\mathrm{Sr}^{/}_{\mathrm{La}}\right]^2 p(\mathrm{H_2O})^{-1} \tag{3.31}$$

$$\mathrm{p} = K_1^{-1}K_2\left[\mathrm{Sr}^{/}_{\mathrm{La}}\right]\left[(\mathrm{PO4})^{\mathrm{x}}_{\mathrm{PO4}}\right]p(\mathrm{H_2O})^{-1}p(\mathrm{O_2})^{\frac{1}{4}} \tag{3.32}$$

When $P_2O_7^{4-}$ are dominant defects, the concentrations of the defects can be described as follows:

$$\left[(\mathrm{P_2O_7})^{\bullet\bullet}_{2\mathrm{PO_4}}\right] = \frac{\left[\mathrm{Sr}^{/}_{\mathrm{La}}\right]}{2} \tag{3.33}$$

$$\left[(\mathrm{HPO_4})^{\bullet}_{\mathrm{PO_4}}\right] = K_1\left(\frac{\left[\mathrm{Sr}^{/}_{\mathrm{La}}\right]}{2}\right)^{\frac{1}{2}} p(\mathrm{H_2O})^{\frac{1}{2}} \tag{3.34}$$

$$\mathrm{p} = K_2\left(\frac{\left[\mathrm{Sr}^{/}_{\mathrm{La}}\right]}{2}\right)^{\frac{1}{2}} p(\mathrm{O_2})^{\frac{1}{4}} \tag{3.35}$$

The effective negative charge of the acceptor substituent in Sr-doped $LaPO_4$ is predominantly compensated by hydrogen phosphate groups in wet atmosphere. In this case, proton conductivity is supposed to be independent of $p(H_2O)$ and $p(O_2)$, as predicted from Eq. (3.30). The hydration reaction (Eq. (3.25)), is generally exothermic so that $P_2O_7^{4-}$ is considered to rule in Sr-doped $LaPO_4$ at higher temperatures. Then Eqs. (3.34) and (3.35) show that the proton conductivity increases with increasing $p(H_2O)$ and that the electron hole conduction increases with increasing $p(O_2)$.

3.9 Defect structures of lanthanum metaphosphate

The conductivity behavior of lanthanum metaphosphate resembles the orthophosphates and many oxides, and a similar defect structure presumably prevails. The effective negative charge of the acceptor substituent in Sr-doped LaP_3O_9 is predominantly compensated by protons in wet atmosphere and oxygen vacancies in dry atmosphere. In the case of metaphosphates we may see these defects as $(\mathrm{P_3O_8})^{\bullet\bullet}_{\mathrm{P_3O_9}}$ playing a similar role as oxygen vacancies in oxides, while $(\mathrm{HP_3O_9})^{\bullet}_{\mathrm{P_3O_9}}$ corresponds to the interstitial protons (or substitutional hydroxide ions). The materials hydrate as water vapor interacts with $(\mathrm{P_3O_8})^{\bullet\bullet}_{\mathrm{P_3O_9}}$ groups according to:

$$\mathrm{H_2O_{(g)}} + (\mathrm{P_3O_9})^{\mathrm{x}}_{\mathrm{P_3O_9}} + (\mathrm{P_3O_8})^{\bullet\bullet}_{\mathrm{P_3O_9}} = 2(\mathrm{HP_3O_9})^{\bullet}_{\mathrm{P_3O_9}} \tag{3.36}$$

The equilibrium constant K for the reaction is expressed as

$$K_3 = \frac{\left[(\mathrm{HP_3O_9})^{\bullet}_{\mathrm{P_3O_9}}\right]^2}{\left[(\mathrm{P_3O_9})^{\mathrm{x}}_{\mathrm{P_3O_9}}\right]\left[(\mathrm{P_3O_8})^{\bullet\bullet}_{\mathrm{P_3O_9}}\right] p(\mathrm{H_2O})} = \exp\frac{\Delta S^{0}_{3}}{R}\exp\frac{-\Delta H^{0}_{3}}{RT} \tag{3.37}$$

The electroneutrality condition of Sr-doped LaP_3O_9 with oxygen vacancies and protons then reads

$$\left[(HP_3O_9)^{\bullet}_{P_3O_9}\right] + 2\left[(P_3O_8)^{\bullet\bullet}_{P_3O_9}\right] = \left[Sr'_{La}\right] \tag{3.38}$$

By inserting the above expression (Eq. (3.38)) for the hydration equilibrium constant (Eq. (3.37)), we obtain the concentration of protonic defects expressed as

$$\left[(HP_3O_9)^{\bullet}_{P_3O_9}\right] = \frac{\left[(P_3O_9)^{x}_{P_3O_9}\right] K_3 p(H_2O)\left(-1+\sqrt{1+\frac{8[Sr'_{La}]}{\left[(P_3O_9)^{x}_{P_3O_9}\right] K_3 p(H_2O)}}\right)}{4} \tag{3.39}$$

At high $p(H_2O)$, the proton concentration is constant, equal to the dopant concentration, and the conductivity expectedly protonic and independent of $p(H_2O)$.

$$\left[(HP_3O_9)^{\bullet}_{P_3O_9}\right] = \left[Sr'_{La}\right] \tag{3.40}$$

$$\left[(P_3O_8)^{\bullet\bullet}_{P_3O_9}\right] = \left[Sr'_{La}\right]^2 K_3^{-1}\left[(P_3O_9)^{x}_{P_3O_9}\right]^{-1} p(H_2O)^{-1} \tag{3.41}$$

At low $p(H_2O)$ we have,

$$2\left[(P_3O_8)^{\bullet\bullet}_{P_3O_9}\right] = \left[Sr'_{La}\right] \tag{3.42}$$

as limiting case, and by inserting the Eq. (3.42) into the expression for the hydration equilibrium constant (Eq. (3.37)), we obtain

$$\left[(HP_3O_9)^{\bullet}_{P_3O_9}\right] = K_3^{\frac{1}{2}}\left[(P_3O_9)^{x}_{P_3O_9}\right]^{\frac{1}{2}}\left(\frac{\left[Sr'_{La}\right]}{2}\right)^{\frac{1}{2}} p(H_2O)^{\frac{1}{2}} \tag{3.43}$$

3.10 Defect structures of proton-conducting pyrophosphates

In pyrophosphates, the pyrophosphate group is not a defect, it is the host anion. It may be hydrated to form hydrogen pyrophosphate defects at pyrophosphate sites, denoted as $(HP_2O_7)^{\bullet}_{P_2O_7}$. These may charge compensate acceptor dopants. However, our results indicate that the protons dissolve in quantities exceeding the dopant level. This means that water dissolves as protons and some negative defect, for instance an interstitial oxide ion. This has been suggested as a prevailing situation in undoped Y_2O_3, an oxide with native oxygen deficiency (empty interstitial oxygen sites) (*88*):

$$2O_O^x + v_i^x + H_2O_{(g)} = O_i'' + 2OH_O^{\bullet} \tag{3.44}$$

In a pyrophosphate, the interstitial oxygen may be denoted as phosphate ions at pyrophosphate sites, $(2PO_4)^{//}_{P_2O_7}$. The hydration reaction can in this case be written

$$3(P_2O_7)^x_{P_2O_7} + H_2O_{(g)} = (2PO_4)^{//}_{P_2O_7} + 2(HP_2O_7)^{\bullet}_{P_2O_7} \tag{3.45}$$

with the equilibrium constant expressed as

$$K_4 = \frac{\left[(2PO_4)^{//}_{P_2O_7}\right]\ \left[(HP_2O_7)^{\bullet}_{P_2O_7}\right]^2}{\left[(P_2O_7)^x_{P_2O_7}\right]^3 p(H_2O)} = \exp\frac{\Delta S_4^0}{R}\exp\frac{-\Delta H_4^0}{RT} \tag{3.46}$$

The electroneutrality condition of an acceptor-doped pyrophosphate with oxygen interstitials and protons can accordingly be written as

$$2\left[(2PO_4)^{//}_{P_2O_7}\right] + \left[A'\right] = \left[(HP_2O_7)^{\bullet}_{P_2O_7}\right] \tag{3.47}$$

At low $p(H_2O)$, the proton concentration is constant, equal to the dopant concentration, and the conductivity expectedly protonic and independent of $p(H_2O)$.

$$\left[A'\right] = \left[(HP_2O_7)^{\bullet}_{P_2O_7}\right] \tag{3.48}$$

$$\left[(2PO_4)^{//}_{P_2O_7}\right] = \frac{K_4\left[(P_2O_7)^{x}_{P_2O_7}\right]^3 p(H_2O)}{\left[A^{/}\right]^2} \tag{3.49}$$

At high $p(H_2O)$ we have,

$$2\left[(2PO_4)^{//}_{P_2O_7}\right] = \left[(HP_2O_7)^{\bullet}_{P_2O_7}\right] \tag{3.50}$$

as limiting case, and by inserting the Eq. (3.50) into the expression for the hydration equilibrium constant (Eq. (3.46), we obtain

$$2\left[(2PO_4)^{//}_{P_2O_7}\right] = \left[(HP_2O_7)^{\bullet}_{P_2O_7}\right] = 2^{1/3} K_4^{1/3}\left[(P_2O_7)^{x}_{P_2O_7}\right] p(H_2O)^{1/3} \tag{3.51}$$

We have combined the equilibrium constant with the full electroneutrality condition, and obtain the following 3rd order equation for the concentration of protons:

$$\left[(HP_2O_7)^{\bullet}_{P_2O_7}\right]^3 - \left[A^{/}\right]\left[(HP_2O_7)^{\bullet}_{P_2O_7}\right]^2 - 2K_4 p(H2O)\left[(P_2O_7)^{x}_{P_2O_7}\right]^3 = 0 \tag{3.52}$$

$$\left[(HP_2O_7)^{\bullet}_{P_2O_7}\right] = \frac{\left[A^{/}\right]}{3} + \frac{2^{\frac{1}{3}}\left[A^{/}\right]^2}{3\left(2\left[A^{/}\right]^3 + 27\times 2K_4 p(H2O)\left[(P_2O_7)^{x}_{P_2O_7}\right]^3 + 3\sqrt{3}\sqrt{2K_4(pH2O)\left[(P_2O_7)^{x}_{P_2O_7}\right]^3}\sqrt{4\left[A^{/}\right]^3 + 27\times 2K_4(pH2O)\left[(P_2O_7)^{x}_{P_2O_7}\right]^3}\right)^{\frac{1}{3}}} + \frac{\left(2\left[A^{/}\right]^3 + 27\times 2K_4 p(H2O)\left[(P_2O_7)^{x}_{P_2O_7}\right]^3 + 3\sqrt{3}\sqrt{2K_4(pH2O)\left[(P_2O_7)^{x}_{P_2O_7}\right]^3}\sqrt{4\left[A^{/}\right]^3 + 27\times 2K_4 p(H2O)\left[(P_2O_7)^{x}_{P_2O_7}\right]^3}\right)^{\frac{1}{3}}}{32^{\frac{1}{3}}} \tag{3.53}$$

3.11 Defect Structures of TiP_2O_7, ZrP_2O_7 and SnP_2O_7

Under oxidizing conditions proton conductivity was dominant in these materials. The electroneutrality condition will be

$$2\left[(2PO_4)^{//}_{P_2O_7}\right] = \left[(HP_2O_7)^{\bullet}_{P_2O_7}\right] \tag{3.54}$$

By inserting the Eq. (3.54) into the expression for the hydration equilibrium constant (Eq. (3.46)), we obtain the concentration of protonic defects expressed as

$$\left[(HP_2O_7)^{\bullet}_{P_2O_7}\right] = 2^{1/3} K_4^{1/3} \left[(P_2O_7)^{x}_{P_2O_7}\right] p(H_2O)^{1/3} \tag{3.55}$$

ZrP_2O_7 acts as a pure proton conductor also in reducing atmospheres, but in TiP_2O_7 and SnP_2O_7, electron conductivity contributes to the total conductivity at higher temperatures. The equilibrium between electrons and protons can be written

$$2(P_2O_7)^{x}_{P_2O_7} + H_2O_{(g)} = 2(HP_2O_7)^{\bullet}_{P_2O_7} + 2e^{/} + \frac{1}{2}O_2 \tag{3.56}$$

and the equilibrium constant of this can be expressed as

$$K_5 = \frac{\left[(HP_2O_7)^{\bullet}_{P_2O_7}\right]^2 n^2 p(O_2)^{1/2}}{\left[(P_2O_7)^{x}_{P_2O_7}\right]^2 p(H_2O)} \tag{3.57}$$

Assuming that electrons are minority defects, and that we can again assume small overall defect concentrations, we can insert the dominating concentration of protons from Eq. (3.55) into Eq. (3.57) and get an expression for the concentration of electrons

$$n = \frac{K_5^{1/2} p(H_2O)^{1/6} p(O_2)^{-1/4}}{2^{1/3} K_4^{1/3}} \tag{3.58}$$

3.12 Brouwer diagrams

Variations in defect concentrations as a result of variable conditions, e.g. changes in the surrounding oxygen or water vapor partial pressures, may be expressed schematically in a Brouwer diagram. A material in equilibrium is always electrical neutral, and the Brouwer diagrams are based on an electroneutrality condition and the equilibrium

expressions of the defect reactions. The defect structure will be dominated by different defects at different oxygen and water vapor partial pressures, and the diagram may be expressed by choosing one negative and one positive defect, and express the other defects as a function of these.

3.12.1 Water vapor dependency

Fig. 3.4 shows a Brouwer diagram for the Sr-doped LaP_3O_9 showing schematically the variations in defect concentrations upon changes in $p(H_2O)$ assuming protons are charge compensated by oxygen vacancies and acceptors. Fig. 3.5 shows a Brouwer diagram for the acceptor doped pyrophosphate showing schematically the variations in defect concentrations upon changes in $p(H_2O)$ assuming protons charge compensated by oxygen interstitials and acceptors.

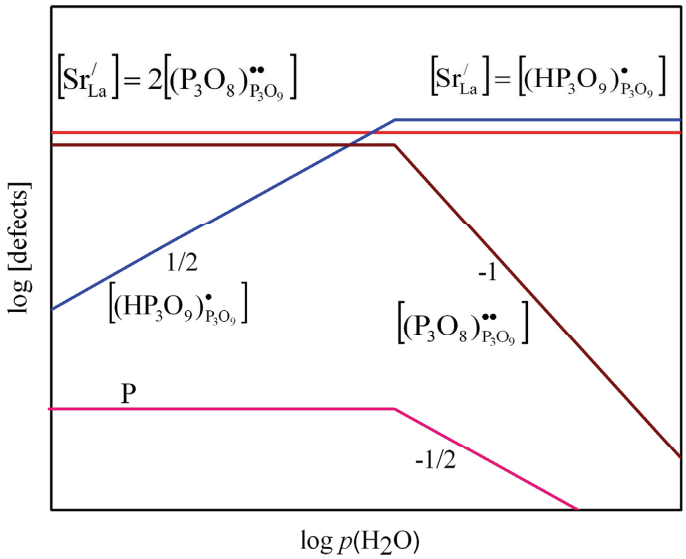

Fig. 3.4 Brouwer diagram for the Sr-doped LaP_3O_9 showing schematically the variations in defect concentrations upon changes in $p(H_2O)$ assuming the $p(O_2)$ constant.

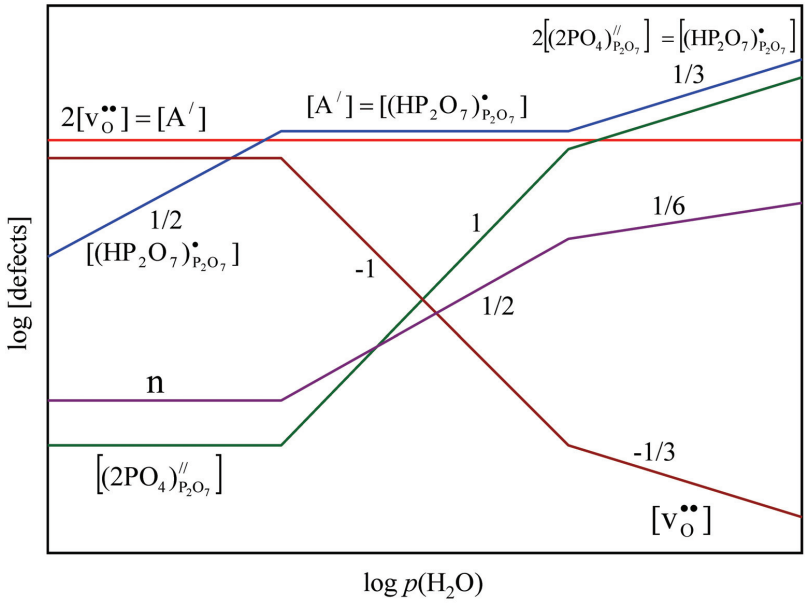

Fig. 3.5 Brouwer diagram for the acceptor doped pyrophosphate showing schematically the variations in defect concentrations upon changes in $p(H_2O)$ assuming the $p(O_2)$ constant.

3.12.2 Oxygen partial pressure dependency

Fig. 3.6 shows a Brouwer diagram for the Sr-doped LaP_3O_9 showing schematically the variations in defect concentrations upon changes in $p(O_2)$ assuming protons are charge compensated by oxygen vacancies and acceptors. Fig. 3.7 shows a Brouwer diagram for the acceptor doped pyrophosphate showing schematically the variations in defect concentrations upon changes in $p(O_2)$ assuming protons charge compensated by oxygen interstitials and acceptors.

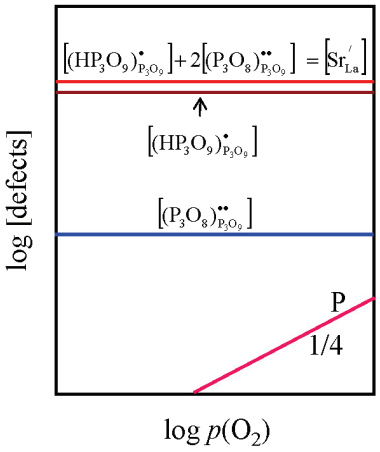

Fig. 3.6 Brouwer diagram for the Sr-doped LaP_3O_9 showing schematically the variations in defect concentrations upon changes in $p(O_2)$ assuming the $p(H_2O)$ constant.

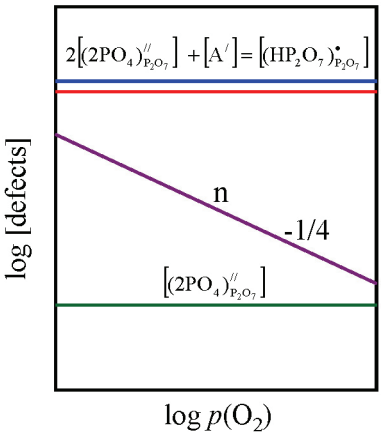

Fig. 3.7 Brouwer diagram for the acceptor doped pyrophosphate showing schematically the variations in defect concentrations upon changes in $p(O_2)$ assuming the $p(H_2O)$ constant.

3.13 Impedance spectroscopy (IS)

Measurements of accurate and meaningful conductivity values, especially in poly-crystalline materials, are often quite difficult. Ideally, the DC conductivity should be measured, in order to be sure that the values pertaining to long range ion migration and not

to dielectric losses such as would be associated with limited or localized rattling of ions within cages. The difficulty in making DC measurements is in finding an electrode material that does not give polarization effects in the boundary between bulk and electrode. When applying AC measurements this electrode problem is avoided, and in addition to the resistance and capacitance of bulk, information on the resistance and capacitance of grain boundaries and electrodes can be retrieved. The principle of AC conductivity measurements by way of modern instruments, as applied in this study, is shown in Fig. 3.8.

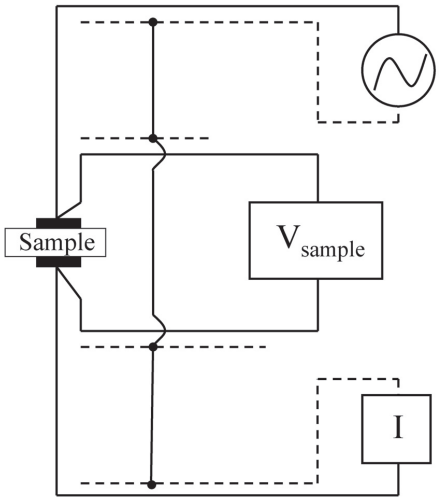

Fig. 3.8 Principle of AC conductivity measurements (*89*).

A harmonic voltage with adjustable amplitude and frequency is applied over the sample, and the voltage across the sample and the current are measured. The current path through the shields, marked with dotted lines in the figure is designed, so as to counteract the current from the leads and give zero net fields around the current cables.

In the desired set-up, the wire resistance and inductance are eliminated and the capacitance and induction between current and voltage leads are reduced. Remaining parasitic elements are mainly parallel capacitance of the order of 1 pF, serial ohmic resistance in the electrode collectors, instrument-resident induction-like error ($\sim 10^{-5}$ H) and high-frequency error and noise.

In AC conductivity measurements the measured complex impedance, Z^*, may be expressed as

$$Z^* = R + jX = \frac{E^*}{I^*} \tag{3.59}$$

where R (resistance) and X (reactance) indicate the real and imaginary part of the impedance, respectively. E^* denotes the measured complex voltage and I^* the complex current. The complex admittance is the reciprocal of the complex impedance, and we have

$$Y^* = \frac{1}{Z^*} = G + jB = \frac{I^*}{E^*} \tag{3.60}$$

where G (conductance) and B (susceptance) are the real and imaginary parts of the admittance, respectively. The susceptance of a capacitor may be written as

$$B = \omega C \tag{3.61}$$

where C is the capacitance and $\omega\,(=2\pi f)$ is the angular frequency.

The bulk impedance of a solid oxide sample may ideally be represented as an RC parallel circuit (*90*), where R represents an ohmic resistor and C is a capacitor, which arises from the long range charge transport and polarization in the material, respectively. The polarization may be caused by the displacement of electron clouds in the lattice atoms, displacement of anions and cations and rotation of dipoles.

In poly-crystalline samples, grain boundaries introduce polarization effects with different time-constants than those stemming from polarization in bulk. This may be represented by a lumped RC unit in series with the RC unit representing bulk. However, different grain size, grain boundary thickness and grain boundary orientations may give dispersion in the time-constants for the polarization. This causes a deviation from an RC circuit which is usually taken into account by representing the capacitance with a so-called constant phase element (CPE) often denoted by a Q in an equivalent circuit. In the same way as for poly-crystalline samples, this effect may be seen also for single crystals upon the existence of domains and domain boundaries. Finally, the electrodes will be polarized and may also typically be represented by a CPE element in parallel with a resistor R. A principle equivalent circuit for the impedance contributions from bulk, grain or domain boundaries and electrodes is shown in Fig. 3.9.

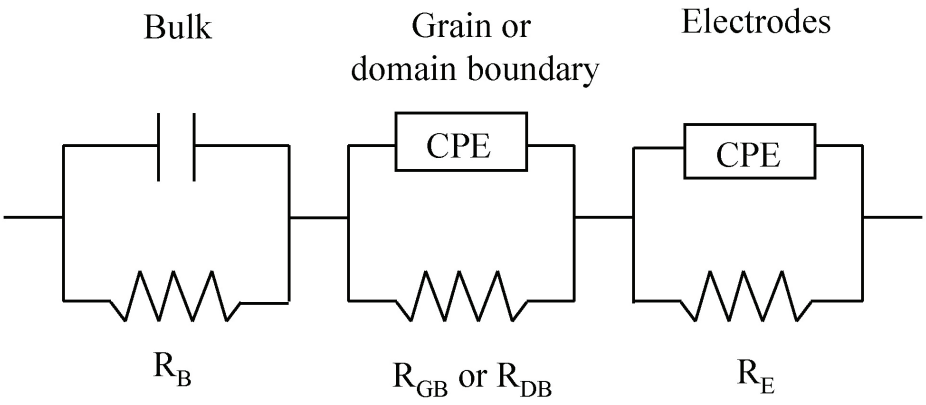

Fig. 3.9 Equivalent circuit for a poly-crystalline material representing the contributions to the impedance from bulk, grain or domain boundaries and electrode. The resistance contributions from bulk, grain or domain boundaries and electrodes are denoted R_B, R_{GB} or R_{DB} and R_E, respectively.

If the time-constants for bulk, grain or domain boundaries and electrode polarization effects are sufficiently different, the processes would show up as three semi-circles in a Nyquist-plot (-X plotted vs R) as seen in Fig. 3.10.

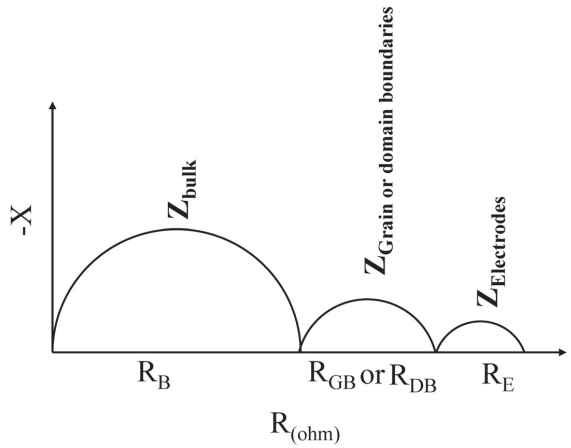

Fig. 3.10 Nyquist plot showing an arbitrarily chosen example of impedance contributions from bulk, grain or domain boundaries and electrodes.

As seen in Fig. 3.10, the lumped RQ units appear as depressed semi-circles as opposed to the perfect semi-circle of the RC parallel circuit of bulk.

The capacitances for bulk, grain or domain boundaries and electrodes are typically of the order 10^{-12} F, 10^{-9} F and 10^{-6} F, respectively, for typical sample geometry. In case of a poly-crystalline material with no domain boundaries present, the two time-constants usually attributed to bulk transport and grain boundary polarization may possibly instead be attributed to bulk transport and rattling of point defects (e.g. protons). Rattling may stem from association between the protons and dopant centres. This can be modeled by the equivalent circuit shown in Fig. 3.11(*90*).

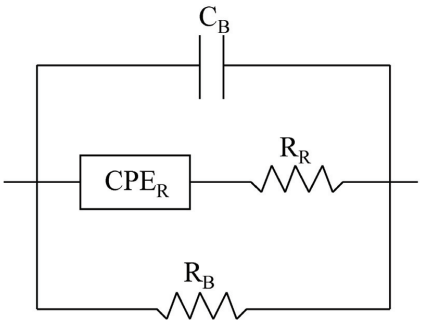

Fig. 3.11 Equivalent circuit representing bulk and the effect where some of the protons are associated with a dopant centre giving rise to a rattling (described by CPE_R and R_R) within an energy cage with a different time constant than for the "free" protons.

Although it is an important aspect, it was not applied in the present work due to the general absence of two time constants.

3.14 Transport number measurements

The transport number for a species *i* is defined as $t_i = \sigma_i / \sigma_{tot}$ where σ_{tot} denotes the total conductivity and σ_i the partial conductivity arising from transport of species *i*. It is important to note that the following discussion excludes interaction between the different charge carriers in a system. For further reading on theory and experimental set-ups for determining transport numbers, see references (*91, 92*).

Consider a material with reversible electrodes in contact with the sample on each side (electrode I and II) and let E_{II-I} denote the voltage measured across the sample at II with reference to I. In general an element X can dissolve and ionize in the material according to:

$$X = X^z + ze^- \tag{3.62}$$

The charge z may be positive or negative, and accordingly, electrons are formed or consumed in the process. A gradient in the activity a_X of X will give rise to an EMF (Electromotive force) often called OCV (Open Circuit Voltage) over the sample. Assuming that the two sides of the sample are equipped with equal and inert electrodes at the same temperature and that X^z and e^- are the only mobile species, the measured OCV will be:

$$E_{II-I} = \frac{-kT}{ze}\int_I^{II} t_{X^z} d\ln a_X \tag{3.63}$$

where t_{X^z} denotes the transport number of the species X^z. Unless the transport number t_{X^z} is 0 or 1, current will flow within the sample and exchange according to Eq. (3.62) will take place. Eq. (3.63) must now be transformed into a form that can be related to experimentally measurable entities. If a small gradient in the activity of X is applied on each side of the sample and one assumes that the transport number is constant within this gradient, Eq. (3.63) can be integrated directly yielding:

$$E_{II-I} = t_{X^z}\frac{-kT}{ze}\ln\left(\frac{a_X^{II}}{a_X^{I}}\right) \tag{3.64}$$

Hence, knowing the activity of X on each side of the sample and measuring the EMF developed, the transport number of X can be found. The transport number obtained will represent a mean value between condition I and II. In the case of oxygen the activities in Eq. (3.64) can be replaced by $p(O_2)$, making z = −4. Noting that a gradient in the partial pressure of oxygen must be accompanied by an inverse gradient in the metal activity, the measured voltage can be expressed as

$$E_{II-I} = t_{M+O}\frac{RT}{4F}\ln\left(\frac{P_{O_2}^{II}}{P_{O_2}^{I}}\right) \tag{3.65}$$

where t_{M+O} represents the sum of the transport numbers for oxygen and metal ions.

For a pure protonic conductor (replacing X with hydrogen) a corresponding Nernst equation may be derived in terms of the hydrogen partial pressure. This may be applied to materials with mixed proton and electron conduction by the introduction of a transport number of protons, t_{H^+}:

$$E_{II-I} = -t_{H^+} \frac{RT}{2F} \ln\left(\frac{P_{H_2}^{II}}{P_{H_2}^{I}}\right) \tag{3.66}$$

This may be rewritten as a function of water vapor pressure and oxygen pressure using the gas equilibrium $2H_{2(g)} + O_{2(g)} = 2H_2O_{(g)}$ to obtain :

$$E_{II-I} = t_{H^+} \frac{RT}{4F} \ln\left(\frac{P_{O_2}^{II}}{P_{O_2}^{I}}\right) - t_{H^+} \frac{RT}{2F} \ln\left(\frac{P_{H_2O}^{II}}{P_{H_2O}^{I}}\right) \tag{3.67}$$

Thus, proton conductors display an OCV in a gradient of $p(O_2)$. With no gradient in $p(H_2O)$, it is identical to that obtained with an oxygen ion conductor. In many oxides depending on temperature, $p(O_2)$ and $p(H_2O)$, a more complex situation with for instance native ionic, protonic and electronic conduction present, is encountered. In the following, protonic defects will comprise protons (H^+), hydroxide ions (OH^-) and hydride ions (H^-). Transport of metal species will be ignored. Sutija et al. (*92*) have described three different approaches and an analytical solution for the OCV of such systems. In general one can deduce the following relationship between the partial pressure of the gas species, the transport numbers and the OCV:

$$E_{II-I} = (t_{M-O} + t_{H^+} + t_{OH^-} - t_{H^-}) \frac{RT}{4F} \ln\left(\frac{P_{O_2}^{II}}{P_{O_2}^{I}}\right) - (t_{H^+} - t_{OH^-} - t_{H^-}) \frac{RT}{2F} \ln\left(\frac{P_{H_2O}^{II}}{P_{H_2O}^{I}}\right) \tag{3.68}$$

By introducing the equilibrium $2H_{2(g)} + O_{2(g)} = 2H_2O_{(g)}$ in Eq. (3.68), the OCV can be expressed in terms of the partial pressure of water and hydrogen or hydrogen and oxygen.

As seen from Eq. (3.68) we can measure the EMF with a small gradient in $p(H_2O)$ and no gradient in $p(O_2)$. This gives the sum of all transfer numbers resulting from the different protonic defects. If, on the other hand, a small gradient in $p(O_2)$ is created while $p(H_2O)$ is held constant, the sum of native ionic and protonic transfer numbers is obtained. With knowledge of which protonic defect that is dominating and remembering that the sum of all transport number is equal to unity.

Chapter 4

Experimental

4.1 Synthesis

The interest in the properties of solids and the development of new materials has given rise to the development of a huge variety of methods for preparing them. Crystalline solids may be prepared in different forms, such as fibers, films, foams, ceramics, powders, nano-particles, and single crystals (*74*). The different methods used to prepare crystalline solids depend on the thermodynamic stability of the compounds to be synthesized. The simplest and most common way of preparing solids is the ceramic method, which is also the case in this study. This method is used widely both industrially and in the laboratory, and can be used for fabrication of poly-crystalline materials or powders.

4.1.1 Ceramic method

The ceramic (solid state reaction) method consists of heating together two non-volatile solids which react to form the required product. This method involves mixing, compacting and firing of reactants to achieve the desired product. Thermodynamics, which determine the change of free energy, and kinetics, that determine the rate of reaction, are important factors to be considered. This method is intrinsically slow but simple. Although the reactants are well-mixed on the macroscopic level, they are very inhomogeneous on the atomic level. Solid state reactions can only take place at the interface of the two solids and once the surface layer has reacted, the reaction continues as the reactants diffuse from the bulk to the interface. Thus, grinding and mixing several times are often necessary. Raising the temperature enables the reaction at the interface and diffusion through the solid to go faster than it would at room temperature. Hence it is necessary to heat the mixture to much higher temperatures, often above 1000 ^{o}C. In this study LaP_3O_9 and 2 mol-% Sr-doped LaP_3O_9 have been synthesized by the solid state reaction method.

Steps in the ceramic method:

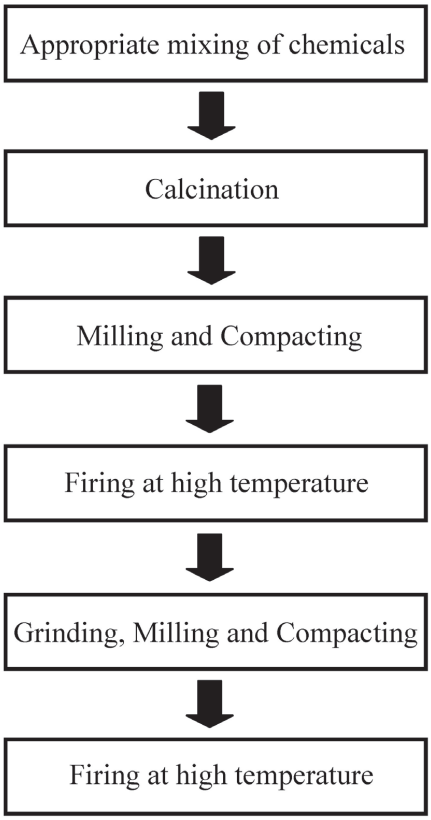

4.1.2 Phosphoric acid method

Different preparative techniques of ceramic materials play a significant role in connection to its properties. Particularly the wet chemical route can play two important roles: 1) the low-temperature synthesis of highly pure and homogeneous substances and 2) the development of fabrication techniques, e.g. films, fibers and monoliths (which is the most beneficial from an industrial point of view) (*93*). Unlike the solid state sintering route the reactants are well-mixed and very homogeneous on the atomic level. Thus, the desired phase can be obtained relatively quickly at low temperatures.

In this study, undoped and acceptor doped pyrophosphates (Ti, Zr and Sn) were synthesized by the phosphoric acid method.

Steps in the phosphoric acid method:

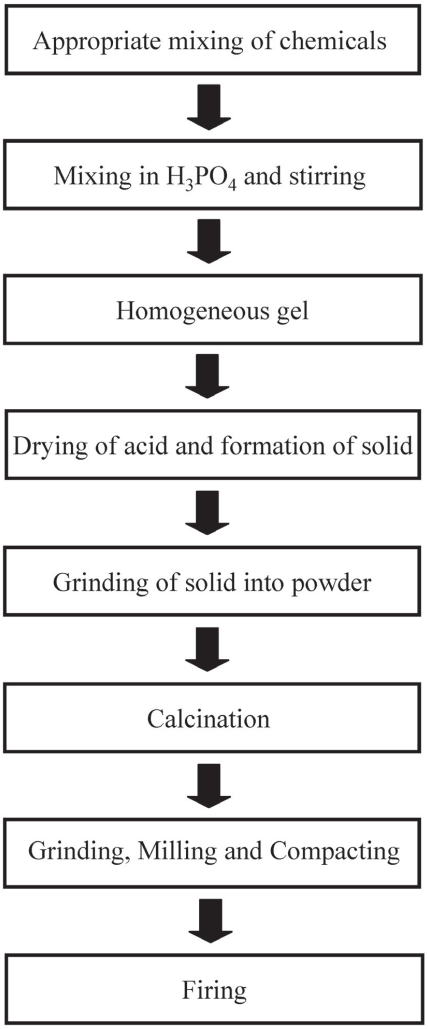

4.2 Sintering

Sintering is the process whereby powders and small particles agglomerate and grow together to form a continuous polycrystalline body. As a rule of thumb the material must be heated to 2/3 of the melting temperature to achieve considerable sintering (*79*).

If the HTPCs are to be applied to electrolytes in electrochemical devices, a highly dense, gastight, and mechanically strong material is required. However, for phosphate-based proton conducting materials, it is sometimes difficult to obtain a highly dense compact by means of the conventional sintering method, because high-temperature sintering is not applicable to some of the phosphates. For LaP_3O_9 and tetravalent pyrophosphate based materials, long-time sintering at high temperature is not feasible because of thermal decomposition of the materials themselves. In this study the samples sintered by the conventional sintering method were highly porous (below 75%). In order to improve the density of the materials, the spark plasma sintering method was used.

4.2.1 Spark plasma sintering method

Spark plasma sintering (SPS) is a relatively new sintering process that generally enables high densification of metals and ceramics at relatively low temperatures within a very short time compared with conventional sintering. In the SPS process, material powder is stacked in a graphite die and pressed uniaxially at typically 30−50 MPa while a pulsed dc current is passed through the specimen. The pulsed current applied momentarily generates local electrical spark discharges and high temperature between the specimen particles, and also heat the graphite die by joule heating. In this way, the powder can be heated from both inside and outside, promoting material flow, accelerating densification, and shortening sintering time. In this work we have sintered the samples (TiP_2O_7 and ZrP_2O_7) at 30 MPa at 1150 ^oC for 5 min, achieving relative final densities of ~ 85−94%.

4.3 Characterization

4.3.1 Scanning electron microscopy (SEM)

Microstructure analysis has been performed with a scanning electron microscope (SEM; FEI Quanta 200 F-field emission gun scanning electron microscope). It can be operated at three vacuum modes to deal with different types of sample. High vacuum (HiVac) is the conventional operating mode associated with all scanning electron microscopes. The two other application modes are low vacuum (LowVac) and ESEM. In

these modes the column is under high vacuum, and the specimen chamber is at a high pressure range of 15 to 4000 Pa. In the present study, we used the high and low vacuum modes.

The energetic electron beam produced in the electron gun is passed through a series of magnetic lenses which have been designed to focus the electron beam to a very fine spot. When the electron beam hits the specimen, interaction between bombarding electrons and the atoms of the specimen results in either elastic (electron-nucleus) or in-elastic (electron-electron) collisions (*94*). Elastic collisions produce backscattered electrons (BSE) which provides both topographic and compositional information about the specimen. Inelastic collisions deposit energy within the sample which releases secondary electrons (SE), X-rays, light photons and heat. SE provide information mainly on surface morphology (*94*). In this study, we have mainly investigated the surface morphology using SE and BSE detectors. Grain size and porosity of the samples were also estimated.

Qualitative and quantitative chemical analysis information is obtained using an energy dispersive X-ray spectrometer (EDS; EDAX Pegasus 2200 Micro-characterization system) with the SEM. The characteristic X-rays emitted when an electron beam irradiated the specimen was used for qualitative and quantitative elemental analysis of the specimens. The emitted X-rays were detected and measured using a detector consisting of a Li doped Si crystal cooled to liquid nitrogen temperature. Each element in the sample emits X-rays with characteristic energy by which it was detected. The intensity of the peaks corresponding to this energy was used to calculate the composition of the illuminated area. In order to obtain accurate X-ray analysis data, the system must be in calibration. A calibration sample of both copper and aluminium is generally used. Calibration was done for each combination of time constant and eV per channel. The calibration panel has edit boxes for the number of counts and the number of iterations. The number of counts refers to the length of collection for each iteration. A sufficient number of counts should be set so that the spectrum is statistically accurate. The standardless quantification was performed by getting the spectrum and results.

4.3.2 X-ray powder diffraction (XRPD)

X-ray powder diffraction is a widely used and powerful analytical technique for characterization of crystalline materials. If synchrotron sources are excluded, X-ray is a

quick and cheap lab scale facility to verify sample phase purity, to identify impurities, determine the degree of sample crystallinity, observe the progress of synthesis, and determine unit cell dimensions.

In this study the X-ray diffraction measurements were carried out at ambient temperature using a Siemens D5000 diffractometer with Bragg-Brentano geometry, variable slit, a position sensitive detector and Cu $K_{\alpha 1}$ radiation (λ = 1.5406 Å). The Cu $K_{\alpha 2}$ (λ = 1.5444 Å) radiation was eliminated with a Ge monochromator. The sample was scanned from 10 ^{o} to 90 ^{o}. Silicon NBS 640b was used as an internal standard (not in every scan). The software EVA 8.0 was used for analyzing the XRD data. Experimentally obtained XRD patterns were compared to the data in the powder diffraction file (PDF) database compiled and revised by Joint Committee on Powder Diffraction Standards International Centre.

4.3.3 Neutron powder diffraction (NPD)

In contrast to x-rays, neutrons are scattered by the nuclei of the atoms. As neutrons carry no charge and because of the small size of the atom core, neutrons can penetrate deep within the sample. Samples for powder diffraction have typically a volume of 1 cm^3. Such large amounts are also necessary because of the relatively small flux of neutrons compared to X-ray photons. The scattering length of the nuclei varies a lot between the elements and it follows no easy trend. The neutron rotates around its own axis and carries a moment. The magnetic moment of the neutron interacts with the unpaired electrons in the material. The total scattering result is a diffractogram containing information on the crystal structure.

A large scale facility is required in order to carry out neutron diffraction. Generally a nuclear reactor or a spallation source is needed to create a high flux of neutrons. High-energy neutrons are produced from a reactor source by the fission of uranium or plutonium, whilst in a spallation source; neutrons of various energies are produced when a high energy proton beam hits a heavy-metal target. In a spallation source pulsed neutrons are produced and in a reactor source neutrons are produced continuously.

Neutron powder diffraction data presented in this work was collected on high-resolution neutron powder diffractometer (PUS-Powder universal spectrometer, Fig. 4.1) instrument at the JEEP II reactor at Kjeller in Norway. Neutrons with λ = 1.5554 Å were provided by a focusing Ge (511) monochromator. Data was collected in the range

2θ = 10−130 ^{o} ($\Delta 2\theta$ = 0.05 ^{o}) by 2 detector banks, each with 7 vertically stacked position sensitive detectors. The sample was contained in a quartz tube with 8 mm inner diameter, which was fitted into a furnace with tantalum heating elements. The furnace with empty quartz tube was also measured for background correction. The structure of TiP_2O_7 was studied at ambient temperature and 800 ^{o}C.

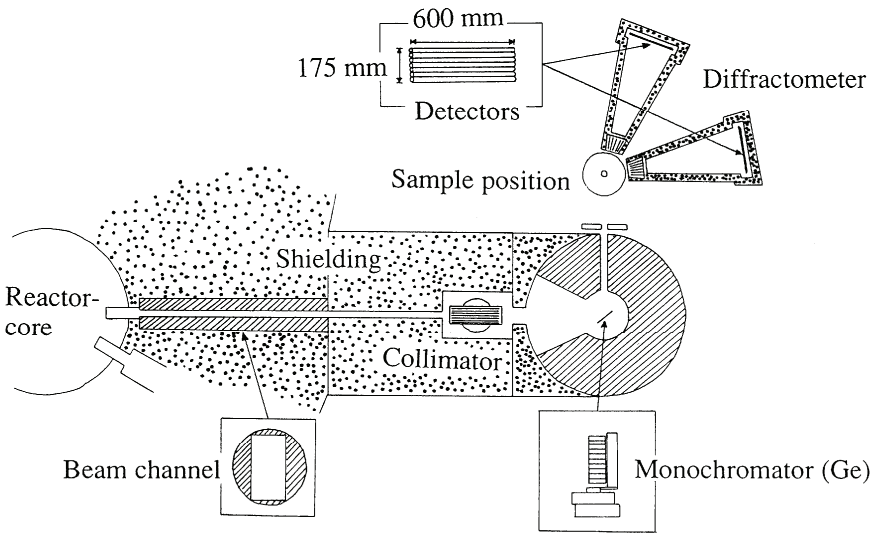

Fig. 4.1 Schematic diagram of the powder universal spectrometer (PUS).

4.3.4 Rietveld analysis

Rietveld analysis is a comprehensive, computer based method for the analysis of whole powder diffraction patterns. It is very important to note that this method is a structure refinement method and not a structure solution method. In the Rietveld method (*95*) least-squares refinements are carried out until the best fit is obtained between the entire observed powder diffraction pattern and the entire calculated pattern. Typically, many Bragg reflections contribute to the intensity, y_i, observed at any arbitrarily chosen point, *i*, in the pattern. The calculated intensities are determined from $|F_k|^2$ values calculated from the structural model plus the background (*96*).

$$y_{i,cal} = \alpha \sum_k L_k |F_k|^2 S_{ik}(2\theta_i - 2\theta_k) P_k A + b_i \quad (4.1)$$

Here α is the scale factor, L_k contains the Lorentz polarization and multiplicity factors, $|F_k|^2$ is the structure factor, S_{ik} is the reflection profile function, P_k is the preferred orientation, A is the absorption factor and b_i is the background intensity at the i-th step. The most widely used reflection profile functions (S_{ik}) are pseudo-Voigt, Pearson VII, and Gaussian, Lorentzian and modified Lorentzian. For all the functions above, H_k, full-width-at-half maximum (FWHM) is used to take instrumental broadening into account,

$$H_k^2 = U \tan^2\theta + V \tan^2\theta + W \quad (4.2)$$

where U, V, and W are instrumental parameters. Standard deviations obtained from Rietveld refinements are usually taken as a measure of precision as the weights depend solely on counting statistics. The accuracy of the structural model fitted to the observed data is judged by reliability (R) factors. It is very important to remember that lower R-values, which imply convergence of least-square calculations, give no guarantee that the model is physically meaningful. Therefore, a very good chemical knowledge is required in this analysis.

In this study, Rietveld analysis was carried out by using either Fullprof (*97*) or GSAS (*98, 99*) software.

4.3.5 Transmission electron microscopy (TEM)

Structural study has been performed in transmission electron microscope (TEM; JOEL 2000FX). To investigate the crystal structure, cell dimensions and morphology, selected area diffraction **(**SAD) and imaging were used. These two basic operations of a transmission electron microscope are schematically shown in Fig. 4.2. When a parallel electron beam passes through a thin specimen (a few hundred angstroms in thickness) the diffraction patterns are formed at the back focal plane and the images are formed at the image plane.

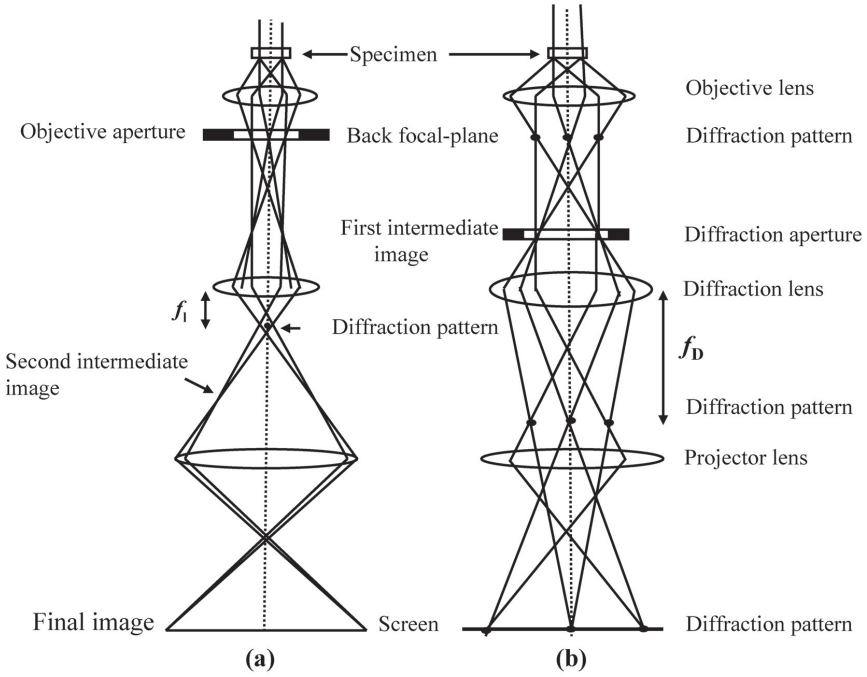

Fig. 4.2 Schematic diagrams showing how an image (a) and diffraction pattern (b) are formed in a TEM (*100*).

Electron diffraction is a collective elastic scattering phenomenon where electrons are scattered by atoms in angular array (crystal). The incoming electron wave interact with the atoms, and secondary waves are generated which interfere with each other. This occurs either constructively or destructively. The scattering event can be described as a reflection of the electrons from atomic planes. The Bragg's law gives the relation between interplanar distance d in a crystal and the diffraction angle 2θ:

$$n\lambda = 2d\sin\theta \tag{4.3}$$

Since the wavelength λ of the electrons and the camera length L of the microscope were known, interplanar distances d were calculated from SAD patterns by using the relation:

$$\lambda L = rd \tag{4.4}$$

where *r* is the measured distance between the direct beam and the reflections measured on the photographic film. Furthermore, information about crystal symmetry could be obtained by the convergent beam electron diffraction (CBED). Images were obtained either by allowing only the direct beam to pass through the crystal, or one of the scattered beams through the crystal. The ray diagram corresponding to this is shown in Fig. 4.3. The bright field (BF) images were obtained when only the direct beam passed through the objective aperture. Dark field (DF) images were obtained when only one of the scattered beams was used to make an image. If the specimen is oriented in such a way that there is only one scattered beam, BF and DF images are complimentary (the dark regions in the BF become bright in DF and vice versa). The contrast in the image is then due to the fact that some regions in the specimen scatter the incident electron beam different than other parts of the specimen.

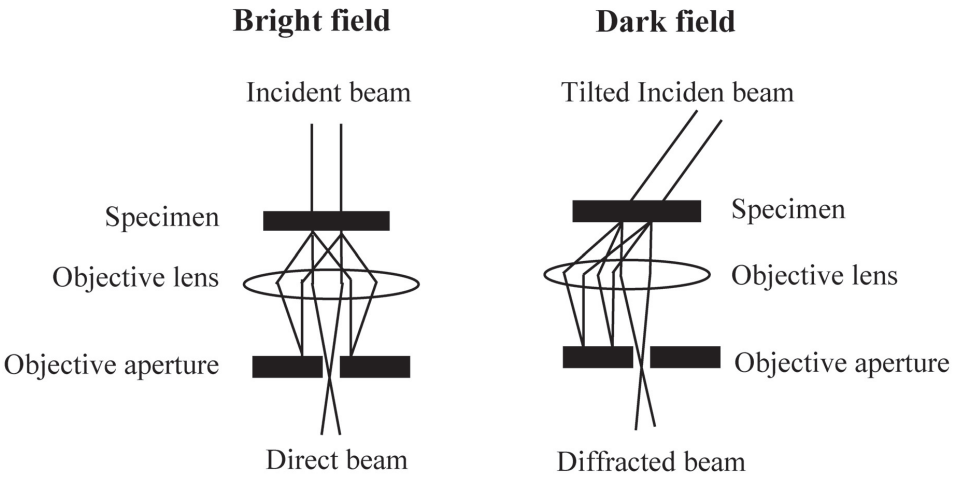

Fig. 4.3 Schematic diagrams showing how a bright field (left) and a dark field (right) image are obtained in a TEM (*101*).

4.3.7 Thermogravimetric analysis (TGA)

Thermogravimetry measures the change in mass of a substance as a function of temperature or time. The results appear as a continuous record as shown in Fig. 4.4. The change in mass (ΔM) upon heating is a fundamental property of the sample, and can be

used for quantitative calculations. Due to a significant mass increase accompanying the hydration reaction, the concentration of protonic defects can be measured.

However, in many cases the change in mass, and thus the change in proton concentration, was found to be less than that predicted from the nominal acceptor dopant concentration. There can be several reasons for this, including thermodynamics of the hydration reactions, distribution of the dopant over more than one site, symmetry reduction, and local lattice distortions. It is difficult to generalize the reasons and it can definitely vary for different systems.

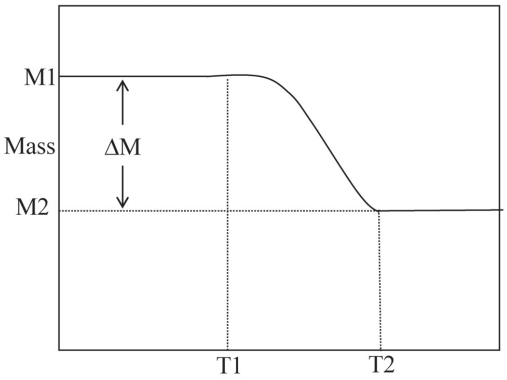

Fig. 4.4 Schematic TG curve showing the change in mass, ΔM, as a function of temperature (*74*).

Thermogravimetric analysis (TGA) was carried out in a Netzsch STA (Simultaneous Thermal Analyzer) 449 C Jupiter instrument. The instrument was especially designed to operate under high water vapor pressures, and in order to achieve such a high pressure it was equipped with a water vapor generator, and a special furnace constructed for high water vapor pressures (see Fig. 4.5).

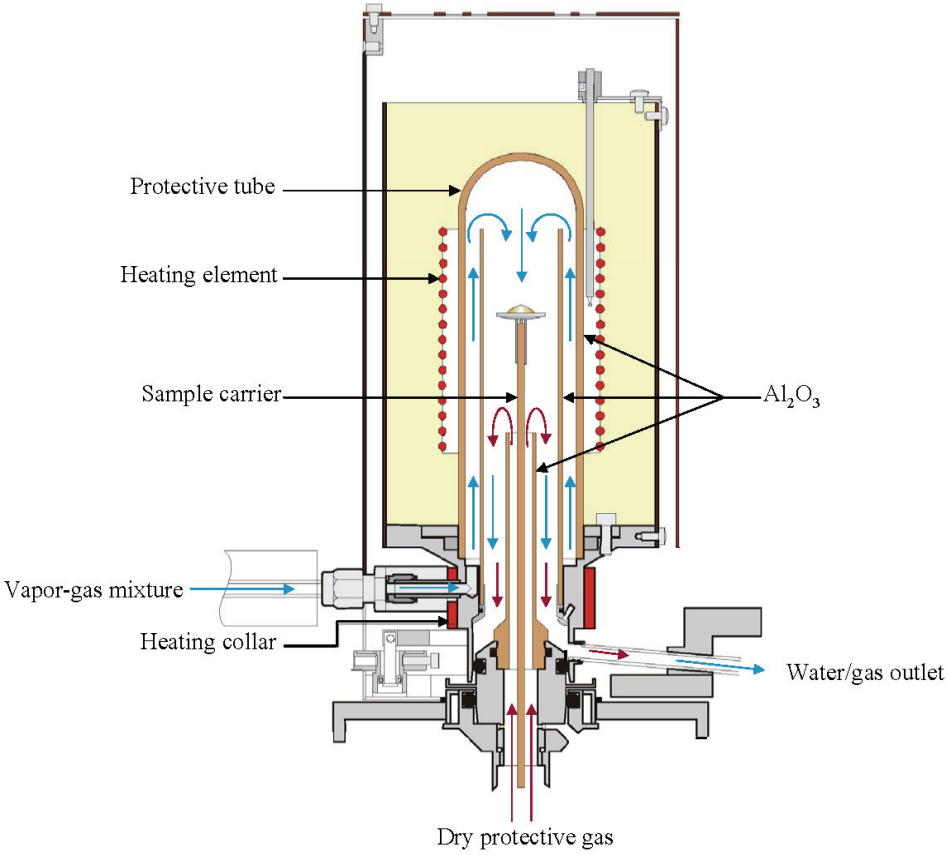

Fig. 4.5 Schematic diagram of the TG-DSC water vapor furnace for high water vapor contents up to 1 atm (*102*).

The vapor generator, shown in Fig. 4.6, produces internally 100% vapor in a special evaporation device. The flow of water for evaporation is measured by a mass flow controller for liquids. The liquid water is completely evaporated (at 180 ^{o}C) and the vapor is introduced into the furnace by a heated transfer line and heating jacket, which excludes condensation. Because of the lines inside the furnace, the vapor or vapor gas mixture is further more preheated to the sample temperature inside the outer flow chamber and guided from the top over the sample; only this vapor or vapor gas mixture arrives at the sample. If a second gas is used to dilute the water vapor, this can be used in two ways, namely within the water vapor generator controlled by a needle valve, or within the instrument using the purge gas channel, controlled by a mass flow controller. In the present study, the 1 atm H_2O was replaced by 0.1 atm H_2O (balance to 1 atm total pressure by N_2).

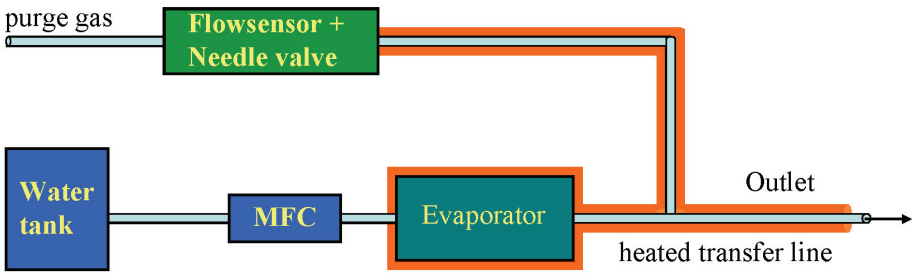

Fig. 4.6 Vapor and gas flow paths in the water vapor generator (*102*).

TGA was carried out on Fe-doped TiP_2O_7 with alumina sample- and reference containers. The sample, consisting of 160 milligrams of powder, was first heated to 900 ^oC at 1.5 ^oC/min in a stream of bottle-dry N_2 gas. It was then equilibrated in N_2 with 0.1 atm H_2O and then cooled at the same rate. All gas flow rates were 50 ml/min. A corresponding correction file was recorded with empty crucibles. The water content in the sample was obtained from the difference between the sample and correction files, using the dry-to-wet step at 900 ^oC as a starting point, assuming the water content in dry atmospheres at 900 ^oC is zero. Similarly, for Sc-doped SnP_2O_7 and Sr-doped LaP_3O_9 the measurements were done isothermally in N_2–0.1 atm H_2O.

4.3.7 Electrical conductivity measurements

Two point AC-conductivity measurements were performed on pressed and sintered samples. For the measurements, circular platinum electrodes of diameter 1 cm were attached to each side of the specimen by painting three layers with platinum ink. The specimens containing electrodes were annealed at 900 ^oC for 2 h to remove residual organics from the platinum ink. The electrical characterization was performed in a ProboStat^{TM} measurement cell (Fig. 4.7) from Norwegian Electro Ceramics AS (NorECS) using a Hewelett Packard 4192A impedance analyzer at a frequency 10 kHz and an oscillation voltage of 1.1 V (rms). The cell was inserted into an external furnace to measure the impedance at different temperatures. Impedance spectroscopy was performed

at different temperatures in the frequency range 5−10^6 Hz, to establish the contributions of bulk, grain boundaries and electrode resistance.

4.3.7.1 ProboStat measurement cell

The ProboStat cell is illustrated in figure (Fig. 4.7). The left part of the picture (Fig. 4.7) shows the base unit of the cell and the right part exhibit the top of the cell (hot zone) in detail where the sample is located.

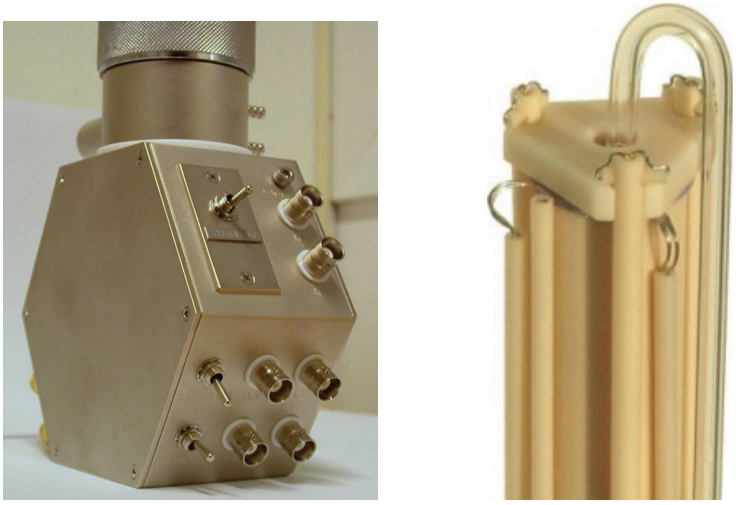

Fig. 4.7 Measurement cell (*103*).

The hot zone is centered in the furnace, and the temperature is measured by a Pt/Pt+10%-Rh thermocouple mounted close to the sample. The base unit of the measurement cell (cold zone) is made of Ni-plated brass. The circular base unit metal block has threads for holding support and outer tubes, it has electrical and gas feedthroughs, water cooling, and underneath a hexagonal shaped connector box.

4.3.7.2 Transport number measurements

The transport numbers for the different charge carriers can be determined using the set-up shown in Fig. 4.8. A 1 mm thick gold ring was placed as sealing gasket between the specimen and the support tube. By means of an outer closed alumina tube, the cell then

forms two gas volumes separated by the specimen. Electrodes leads from the cell base were attached to the circular electrodes on the specimen – from underneath inside the inner compartment, and on top of the specimen, from the outer gas compartment. A spring loaded alumina assembly held the parts together to maintain contact between the Pt leads and the electrodes and to facilitate the gold ring sealing. The gold ring softened and sealed after heating to ~1060 ^{o}C. The inner and outer compartments were connected to a gas mixer so as to establish well-defined partial pressures and gradients of oxygen and water vapor across the specimen. The leakage can be detected either by flow reading decreasing

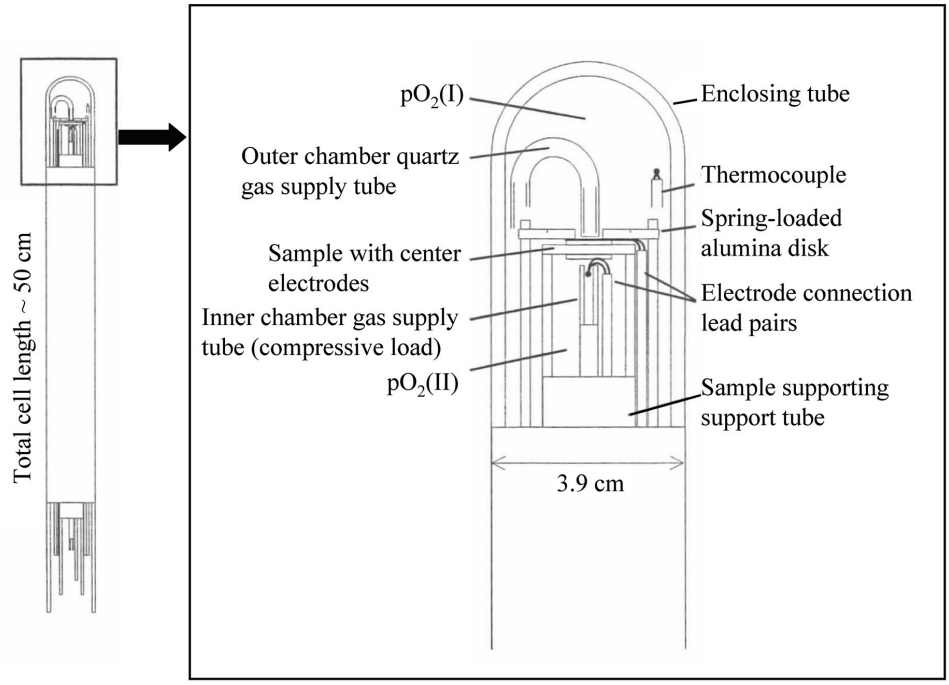

Fig. 4.8 Principle drawing of two point EMF measurement in a gas concentration cell.

when closing the outlet of the cell or by a mass spectrometer. The voltages resulting from differences in the chemical potentials across the specimen induced by gas partial pressure gradients were measured with a Schlumberger Solartron 7150 Plus high-impedance voltmeter. The absolute value of the EMF's will be influenced by any leakage over the sample, decreasing the effective activity gradients and thereby the apparent transport

number. Sealant could be used but was avoided because of risk of sample contamination. The error in the transport number was minimized by extrapolating the transport numbers back zero gradients (for further details, see: (*91, 92*)).

In the present work EMF measurements were done on the 2 mol-% Y-doped ZrP_2O_7 at 600 ^oC in wet oxygen to determine qualitatively the transport number for protons. These measurements involved measuring the voltage over the sample when exposed to two different water vapor partial pressures while keeping the oxygen partial pressure the same on both sides. One of the water vapor pressures was always that of 0.025 atm, while the other came from increasingly drier gas. The EMF of a cell exposed to a gradient in $p(O_2)$ (oxygen vs argon) but not $p(H_2O)$ (both wet) was also measured in a similar manner.

4.3.7.3 Instrument control

The set-up for measuring the conductivity of ceramic samples is illustrated in Fig. 4.9. The measurements are computer controlled through a GPIB interface. The measurement cells are connected to the measuring devices (impedance analyzer and/or voltmeter) by a GPIB interfaced multiplexer system. The purpose of the multiplexer system is to automatically connect a sample to a measuring device such that several samples can share devices, and each sample can be studied with several devices. The multiplexer system can scan over the different samples, enabling the measurement devices to measure on one cell after the other in a continuous manner. The open contact and isolation resistance of the multiplexer unit is higher than 10^9 Ω, indicating that we may expect a background conductivity of the order of 10^{-9} S/Ω. The computer control and the mathematical routines for extracting conductivity and transport numbers are all included in the "IS" program package (*104*).

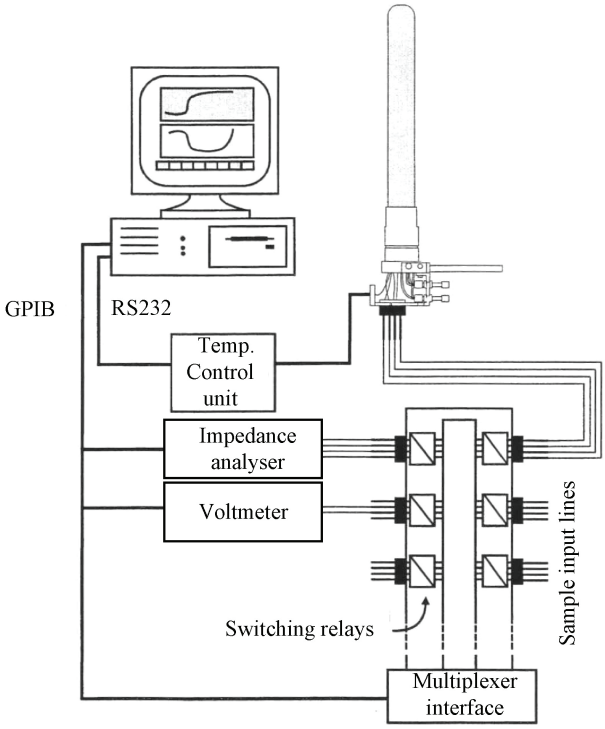

Fig. 4.9 Schematic illustration of the instrument control and multiplexer unit. The four main leads going from the cell, through the multiplexer system and to the measuring devices (voltmeter and impedance analyzer) have separate shields. The set-up is shown with one measuring cell connected (*89*).

4.3.7.4 Mixing of gases

To control the gas mixtures used in conductivity and transport number measurements a complex flowmeter controlled gas mixer unit was used (Fig. 4.10). Three different gases can be mixed in the apparatus. Each mixing unit (M_1−M_6) was equipped with two different flowmeters; one with a glass ball and one with a tantalum ball. Depending on the density of the gas, the flow in the tantalum ball flowmeters is about 5−10 times as high as the flow in the ones with glass balls. In this way it was possible to dilute GAS l about $1{:}10^{3-4}$, while the water vapor content can be diluted by approximately 1:100. Oxygen partial pressures in the range from 1 to 10^{-30} atm can be reached through the use of O_2/Ar, CO/CO_2 and H_2/Ar mixtures depending on the cell temperature. Wet and dry conditions are obtained through the M_4 and the M_6 mixing unit. Wet conditions are

achieved by running the gas through a saturated KBr solution giving a water vapor pressure of approximately 0.023 atm at room temperature (25 ^{o}C). Drying was achieved by running the gas through a column of P_2O_5 leaving less than 1 ppm H_2O in the gas. In practice the partial pressure of water in the dried gas in the high temperature cell is estimated to be 30 ppm ($3{\cdot}10^{-5}$ atm) (*105*) due to the permeability of H_2O through the single wall alumina cell. Intermediate water vapor pressures were attained by mixing wet

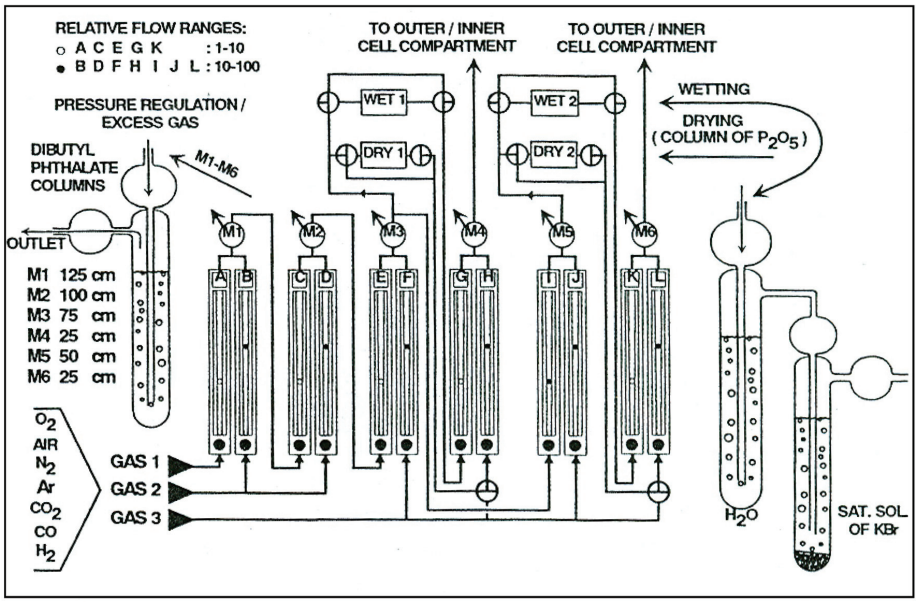

Fig. 4.10 Schematic drawing of the flowmeter controlled gas-mixing unit used in the setup for measuring transport number and conductivity (*106*).

and dry portions of the gas. Excess gas from the mixing units (M_1−M_6) was directed to columns of dibutyl phthalate to ensure a constant pressure of the gas to the next mixing unit or to the cell. The gas mixtures was finally fed to the measurement cell from M_4 and M_6 from two additional flowmeters (not shown in Fig. 4.10), and can be directed either to the inner or the outer cell compartment (important for creating partial pressure gradients as in EMF measurements). The partial pressure of the different gases was calculated by the use of a computer program [GASMIX (*107*)] which accounts for all parameters involved.

In this study Electrical conductivity was measured under various oxygen and water vapor partial pressures. The oxygen partial pressure, $p(O_2)$, was changed by using pure O_2

or Ar/O_2 and H_2/Ar gas mixtures. Water vapor partial pressure, $p(H_2O)$, was varied from 0.025 to $3 \cdot 10^{-5}$ atm by mixing dry gas with gas bubbled through a saturated solution of KBr(aq) at room temperature. In order to confirm protonic conduction, conductivity of the materials under D_2O atmosphere was also measured.

Specific conductivities were obtained by taking the thickness and electrode area of the sample into account, together with the porosity.

$$\sigma SP = G_{Mea} \frac{Thickness}{Electrode\,area} \quad \frac{1}{(1 - porosity)^2} \quad (S/cm) \tag{4.5}$$

The program 2D Table curve was used for modeling of experimental results.

Chapter 5

Summary of results and discussions

5.1 Synthesis and structural characterization

We have investigated four series of materials, namely

1) TiP_2O_7 (undoped, 2 mol % Al, Sc and Fe-doped)

2) ZrP_2O_7 (undoped, 2 mol % Sc, Y and La-doped)

3) SnP_2O_7 (undoped and 2 mol % Sc-doped)

4) LaP_3O_9 (undoped and 2 mol % Sr-doped)

All the pyrophosphate samples showed cubic superstructure of space group $Pa\bar{3}$ at room temperature and metaphosphates showed orthorhombic structure of space group $C222_1$. The unit cell of TiP_2O_7 and LaP_3O_9 is shown in Fig. 5.1 and Fig. 5.2. The results of structural characterization for all the samples are shown in Table 5.1.

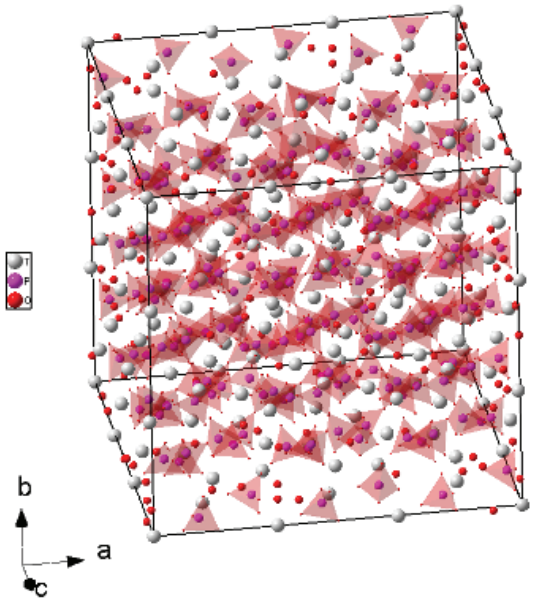

Fig. 5.1 Unit cell of TiP_2O_7

Table 5.1 Structural parameters for the different phosphate samples at ambient temperature.

No.	Sample	Structure	Space group	*a*	*b*	*c*	Porosity	Grain size	Stability
				(Å)	(Å)	(Å)	(%)	(μm)	(^{o}C)
1	Undoped TiP_2O_7	cubic superstructure	*Pa-3*	23.533(1)			~26	1–4	1050
2	2 mol-% Al-doped TiP_2O_7	cubic superstructure	*Pa-3*	23.524(2)			~26	2–10	1050
3	2 mol-% Sc-doped TiP_2O_7	cubic superstructure	*Pa-3*	23.596(3)			~5	-	1050
4	2 mol-% Fe-doped TiP_2O_7	cubic superstructure	*Pa-3*	23.528(1)			~15	-	1050
5	Undoped ZrP_2O_7	cubic superstructure	*Pa-3*	24.717(1)			~20	0.5–2.5	1100
6	2 mol-% Sc-doped ZrP_2O_7	cubic superstructure	*Pa-3*	24.706(3)			~25	-	1100
7	2 mol-% Y-doped ZrP_2O_7	cubic superstructure	*Pa-3*	24.7213(9)			~14	-	1100
8	2 mol-% La-doped ZrP_2O_7	cubic superstructure	*Pa-3*	24.7158(6)			~25	0.5–2.5	1100
9	Undoped SnP_2O_7	cubic superstructure	*Pa-3*	23.820(1)			~28	~0.25	1000
10	2 mol-% Sc-doped SnP_2O_7	cubic superstructure	*Pa-3*	23.005(3)			~20	~0.25	1000
11	Undoped LaP_3O_9	orthorhombic	$C222_1$	11.3043(2)	8.6482(4)	7.3962(1)	~25	1–4	700
12	2 mol-% Sr-doped LaP_3O_9	orthorhombic	$C222_1$	11.3135(4)	8.6571(1)	7.3986(3)	~25	2–10	700

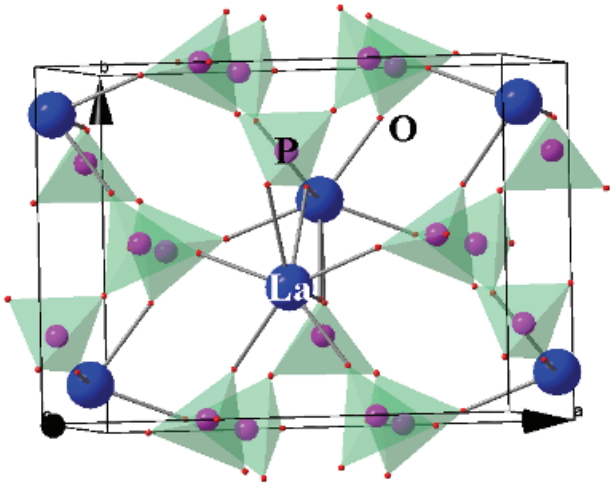

Fig. 5.2 Unit cell of LaP_3O_9

Chernorukov et al. (*108*) reported that below 730 °C TiP_2O_7 exists in a cubic α modification (a = 23.52 Å) and above 730 °C transforms into the cubic β modification (a = 7.80 Å). This phase transition was also observed in the present study at similar temperatures by conductivity measurements as well as by neutron diffraction (*109*). Similarly in ZrP_2O_7 the room temperature cubic superstructure was transformed to a modulated cubic phase at ~290 °C (*110*). Two high temperature phase transitions were reported in SnP_2O_7 (*111*). On heating to ~277 °C it undergoes a phase transition to a structure in which the subcell reflections show a triclinic distortion; above ~557 °C the subcell reflections show a rhombohedral distortion. On cooling the material, it appears to retain a rhombohedral splitting at 495 °C and shows a more gradual reversion to cubic symmetry. In our conductivity measurements on cooling the sample (Sc-doped SnP_2O_7) from 900−200 °C, the phase transition was seemingly observed at ~420 °C and ~255 °C.

For TiP_2O_7, sintering at higher temperatures than 1050 °C causes formation of $TiO(P_2O_7)$, and the existence of such impurity phases considerably deteriorates the conductivity. For LaP_3O_9-based materials, a long-time sintering at higher temperatures than 800 °C is not available because of the thermal decomposition of the materials themselves. According to our high temperature study the stability of the materials are in the following order:

$$LaP_3O_9 < SnP_2O_7 < TiP_2O_7 < ZrP_2O_7$$

5.2. Electrical measurements

5.2.1 Temperature dependencies

The total conductivity of different phosphates is shown as a function of inverse temperature in Fig. 5.3 and Fig. 5.4 for H_2O- and D_2O-wetted, and dry oxygen atmospheres. In the doped TiP_2O_7 and ZrP_2O_7 each curve is obtained after equilibration at 1000 °C, and was recorded during cooling ramps of 18 °C/h to 500 °C. In SnP_2O_7, the conductivity was measured from 900 to 500 °C. In metaphosphates the conductivity was measured between 700 and 300 °C. The conductivity of the materials in wet atmospheres was significantly higher than in dry and in D_2O atmospheres, showing that the protonic conduction was dominant in these materials. The existence of a clear isotope effect suggests that the transfer of protons in the materials takes place by Grotthuss hopping mechanism, similar to perovskite oxides (*112*). A sharp bend in the conductivity curve of TiP_2O_7 (Fig. 5.3) is due to a phase transition of the sample.

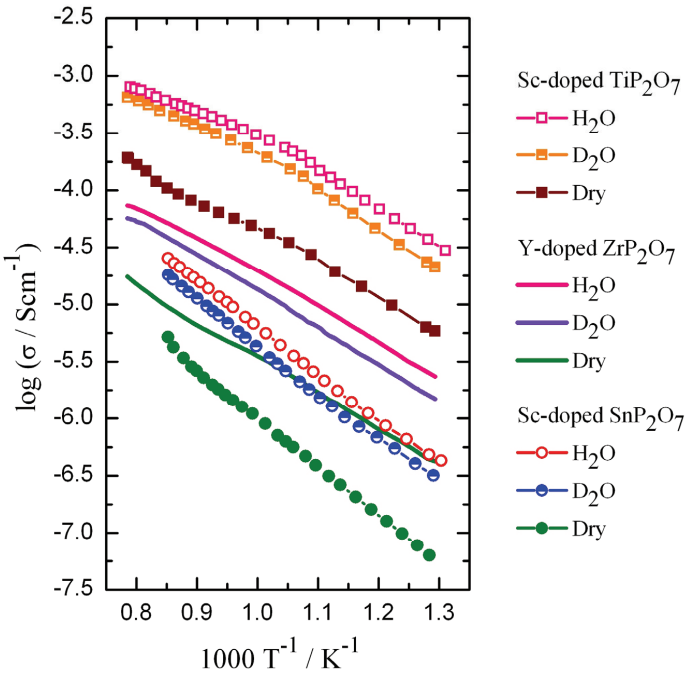

Fig. 5.3 Temperature dependence of the total conductivity for Sc-doped TiP_2O_7, Y-doped ZrP_2O_7 and Sc-doped SnP_2O_7 in wet, D_2O-containing, and dry oxygen atmospheres.

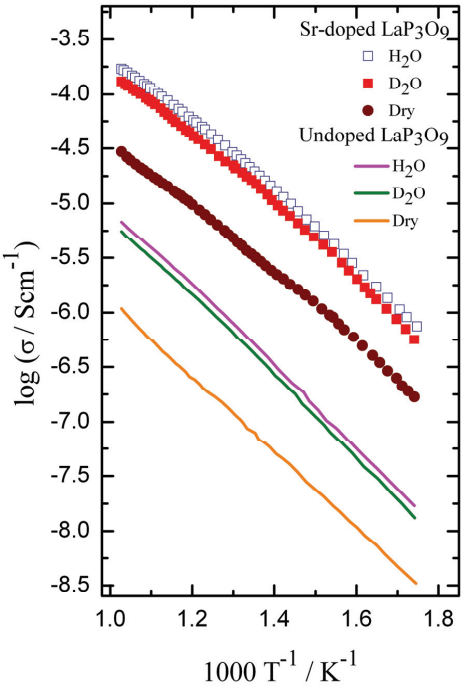

Fig. 5.4 Temperature dependence of the total conductivity for undoped and Sr-doped LaP_3O_9 in wet, D_2O-containing, and dry oxygen atmospheres.

Conductivity measurements of 2 mol-% Sc-doped SnP_2O_7 in wet oxygen atmosphere between 900 and 200 ^oC is shown in Fig. 5.5. The conductivity curve shows bends at ~420 ^oC and ~255 ^oC, indicative of a phase transition, probably the one reported in the literature (*108*). However Tao (*73*) reported that by heating poorly sintered samples, the conductivity decreased between 250 and 300 ^oC, which might be related to possible water desorption. The results of electrical characterization for all the samples are shown in Table **5.2**. According to our electrical conductivity measurements the activation energy of different phosphate samples are in the range 0.7 to 0.8 eV, similar to that of rare earth orthophosphate (*61*). By comparing the results, the total conductivity of the materials are in the following order:

$$TiP_2O_7 < LaP_3O_9 < ZrP_2O_7 < SnP_2O_7$$

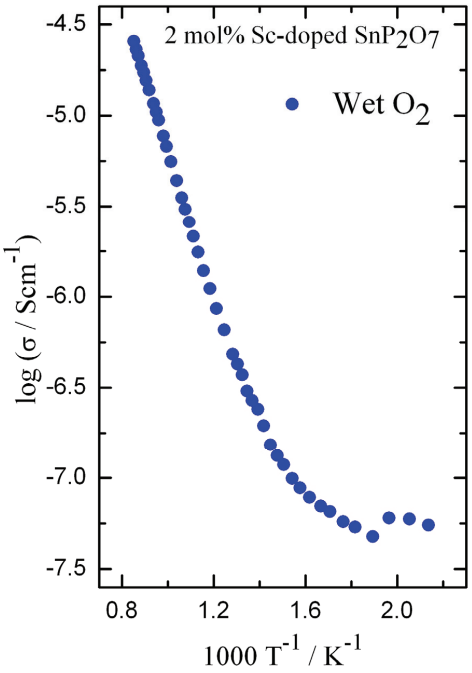

Fig. 5.5 Temperature dependence of the total conductivity for Sc-doped SnP_2O_7 in wet oxygen atmospheres.

Table 5.2 Electrical parameters for the different phosphate samples.

No.	Sample	Activation energy (e.V)	Isotope effect (1000–500 °C)	Total conductivity Wet O_2 (1000 °C) (S/cm)	Total conductivity (Reducing conditions) (1000 °C) (S/cm)
1	Undoped TiP_2O_7	0.70 (500–674 °C) 0.47 (692–1000 °C)	1.33–1.76	$3.2 \cdot 10^{-4}$	-
2	2 mol-% Al-doped TiP_2O_7	0.69 (500–654 °C) 0.47 (673–1000 °C)	1.34–1.85	$4.6 \cdot 10^{-4}$	-
3	2 mol-% Sc-doped TiP_2O_7	0.75 (500–680 °C) 0.49 (700–1000 °C)	1.59–1.27	$8.0 \cdot 10^{-4}$	$5.2 \cdot 10^{-3}$
4	2 mol-% Fe-doped TiP_2O_7	0.76 (500–680 °C) 0.51 (700–1000 °C)	1.54–1.20	$7.0 \cdot 10^{-4}$	$1.3 \cdot 10^{-2}$
5	Undoped ZrP_2O_7	0.80 (600–900 °C)	1.23–1.27	$7.1 \cdot 10^{-6}$	-
6	2 mol-% Sc-doped ZrP_2O_7	0.78 (600–900 °C)	1.29–1.47	$5.6 \cdot 10^{-5}$	$5.5 \cdot 10^{-5}$
7	2 mol-% Y-doped ZrP_2O_7	0.70 (600–900 °C)	1.30–1.58	$7.4 \cdot 10^{-5}$	$7.3 \cdot 10^{-5}$
8	2 mol-% La-doped ZrP_2O_7	0.79 (600–900 °C)	1.28–1.50	$1.2 \cdot 10^{-5}$	-
9	Undoped SnP_2O_7	0.80 (500–900 °C)	1.25–1.35 (900-500 °C)	$3.3 \cdot 10^{-6}$ (900 °C)	-
10	2 mol-% Sc-doped SnP_2O_7	0.88 (500–900 °C)	1.31–1.45 (900–500 °C)	$2.6 \cdot 10^{-5}$ (900 °C)	$6.0 \cdot 10^{-5}$ (900 °C)
11	Undoped LaP_3O_9	0.81 (300–600 °C)	1.18–1.28 (300–700 °C)	$6.8 \cdot 10^{-6}$ (700 °C)	-
12	2 mol-% Sr-doped LaP_3O_9	0.77 (300–600 °C)	1.22–1.30 (300–700 °C)	$1.7 \cdot 10^{-4}$ (700 °C)	$1.7 \cdot 10^{-4}$ (700 °C)

5.2.2 Dependencies on oxygen partial pressure

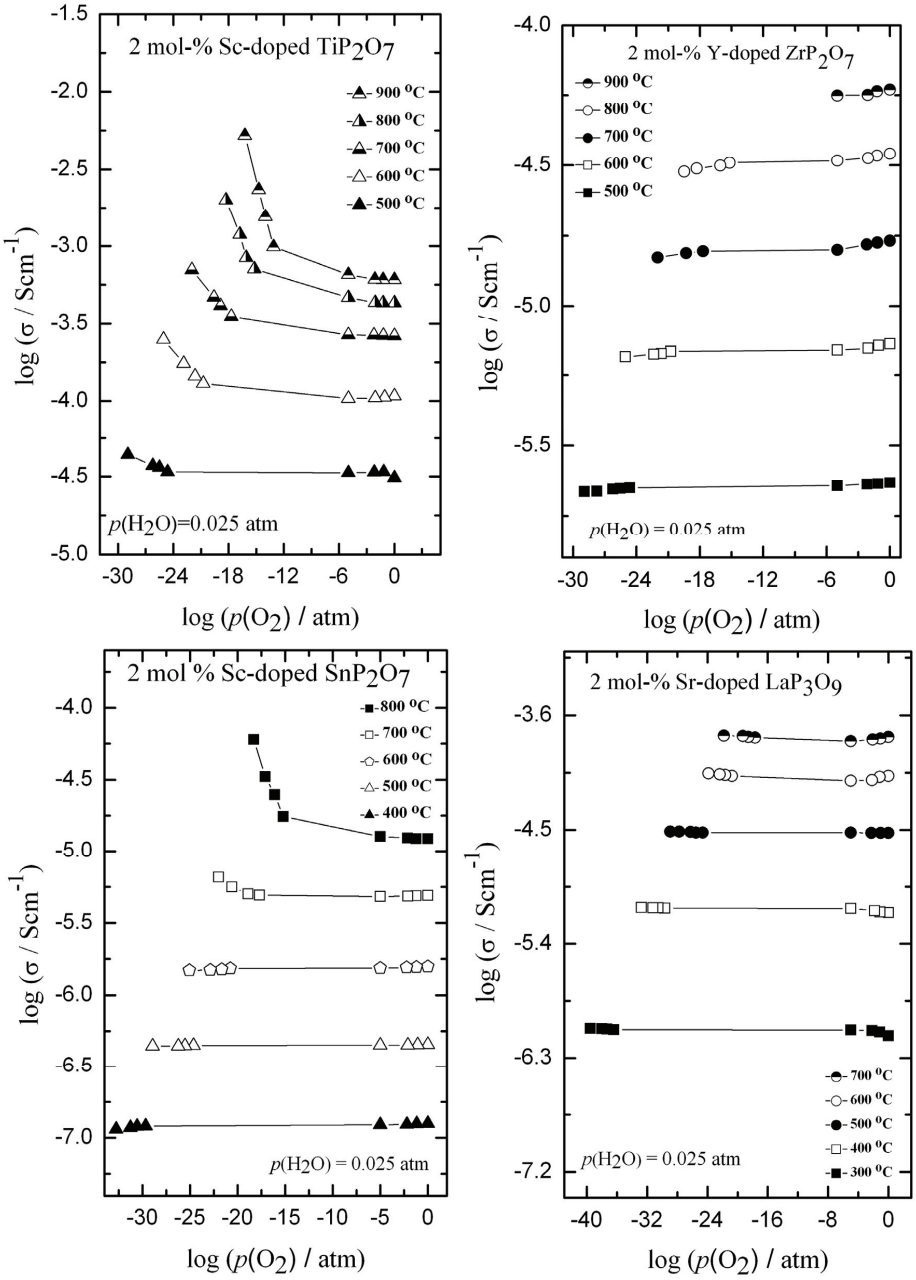

Fig. 5.6 Measured total conductivity for acceptor doped TiP_2O_7, ZrP_2O_7, SnP_2O_7 and LaP_3O_9 as a function of $p(O_2)$ at constant $p(H_2O)$ = 0.025 atm.

Fig. 5.6 shows total conductivity vs $p(O_2)$ at constant $p(H_2O)$. In ZrP_2O_7 and LaP_3O_9, conductivities were almost independent of partial pressure of oxygen under oxidizing and reducing conditions at each temperature, indicating that there is no electronic contribution to the total conductivity and protonic conduction is predominant. In TiP_2O_7 and SnP_2O_7 under oxidizing conditions the conductivity is mainly protonic. On the other hand, under reducing conditions towards high temperatures, n-type electronic conductivity is contributing to the total conductivity. This may be attributed to the reducibility of Ti^{4+} into Ti^{3+} states and Sn^{4+} into Sn^{3+} states in TiP_2O_7 and SnP_2O_7, respectively.

5.2.3 Dependencies on water vapor partial pressure

Fig. 5.7 shows conductivity measurements for different phosphates as a function of $p(H_2O)$ in an oxidizing atmosphere. The oxygen partial pressure is kept constant at each temperature. The conductivity increases with increasing water vapor pressure and it is approximately proportional to $p(H_2O)^{1/3}$ at 500−900 ^oC for pyrophosphates. In pyrophosphates the conductivity of the acceptor-doped samples is higher than the conductivity of the undoped one; however the $p(H_2O)$ and $p(O_2)$ dependencies are similar. It seems that the acceptor doping appears to not be significant for the defect structure. Hence, we believe the increased conductivity is due to the microstructure of the material. The $p(H_2O)$ dependencies of the conductivity of ZrP_2O_7 have been curve fitted at each temperature assuming protons are charge compensated by oxygen interstitials. The $p(H_2O)$ dependencies of the conductivity of TiP_2O_7 and SnP_2O_7 have been modeled assuming protons are charge compensated by oxygen interstitials and with conductivity contributions from minority electrons at high temperatures.

The conductivities of dominating protons and minority electrons are expressed as

$$\sigma_{H^+} = zFc_{0,H^+}\mu_{0,H^+}p(H_2O)^{1/3}\frac{1}{T}\exp\left(\frac{-(\frac{1}{3}\Delta H_1^0 + \Delta H_{m,H^+})}{RT}\right) = \sigma_{0,H^+}p(H_2O)^{1/3}\frac{1}{T}\exp\left(\frac{-\Delta H_{H^+}}{RT}\right) \quad (5.1)$$

$$\sigma_n = zFn_0\mu_{0,n}p(H_2O)^{1/6}\,p(O_2)^{-1/4}\frac{1}{T}\exp\left(\frac{-(\frac{1}{2}\Delta H_2^0 - \frac{1}{3}\Delta H_1^0 + \Delta H_{m,n})}{RT}\right)$$

$$= \sigma_{0,n} p(H_2O)^{1/6} p(O_2)^{-1/4} \frac{1}{T} \exp\left(\frac{-\Delta H_n}{RT}\right) \tag{5.2}$$

The activation enthalpies (ΔH) and pre-exponentials ($zFc_0\mu_0$) have been extracted from the modeling. The extracted parameters are listed in Table 5.3. In TiP_2O_7, the change in the parameters between low and high temperature is assigned to the phase transformation.

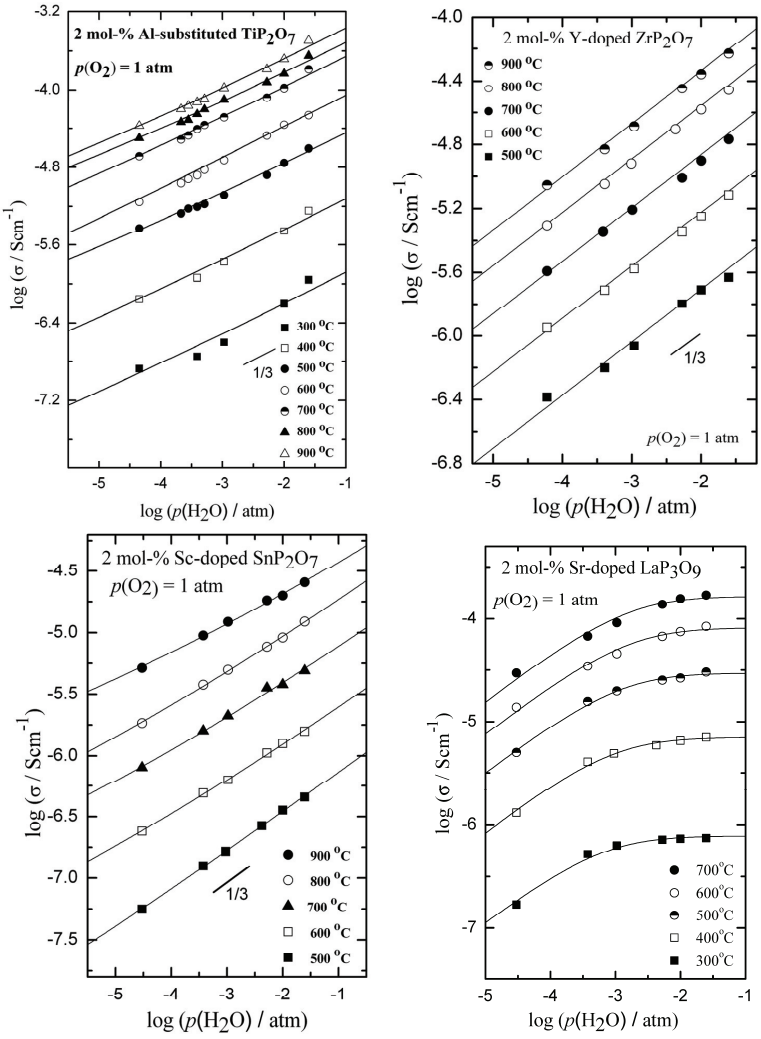

Fig. 5.7 Measured and modeled total conductivity for acceptor doped TiP_2O_7, ZrP_2O_7, SnP_2O_7 and LaP_3O_9 as a function of $p(H_2O)$ at constant $p(O_2)$ = 1 atm. The lines represent the corresponding fitted conductivities.

Table 5.3 The extracted activation enthalpies and pre-exponentials of partial proton and electron conductivities from the modeling of $p(H_2O)$ dependency of the conductivity results.

No.	Sample	Pre-exponential of partial proton conductivity ($zFc_{0,H^+}\mu_{0,H^+}$)	Activation enthalpy of partial proton conductivity (ΔH_{H^+})	Pre-exponential of partial electron conductivity ($zFn_{0,n}\mu_{0,n}$)	Activation enthalpy of partial electron conductivity (ΔH_n)
		(SK/cm)	(kJ/mol)	(S K/cm)	(kJ/mol)
1	2 mol-% Al-doped TiP_2O_7				
	(300−600 °C)	$(2 \pm 1.5)\cdot 10^3$	68 ± 5	-	-
	(Cubic α-modification)				
	(700 −900 °C)	60 ± 35	36 ± 8	$10^{4\pm1}$	110 ± 20
	(Cubic β- modification)				
2	2 mol-% Fe-doped TiP_2O_7				
	(500−700 °C)	$(2 \pm 1)\cdot 10^3$	66 ± 2	-	-
	(700−900 °C)	62 ± 30	35 ± 5	$10^{8\pm1}$	208 ± 25
3	Undoped ZrP_2O_7	40 ± 5	79 ± 2	-	-
4	2 mol-% Sc-doped ZrP_2O_7	260 ± 120	82 ± 5	-	-
5	2 mol-% Y-doped ZrP_2O_7	217 ± 32	67 ± 1	-	-
6	Undoped SnP_2O_7	14 ± 5	70 ± 2	$154 \overset{\times}{\div} 6$	105 ± 15
7	2 mol-% Sc-doped SnP_2O_7	147 ± 30	76 ± 2	$(7.3\cdot 10^4) \overset{\times}{\div} 6$	144 ± 20

In LaP_3O_9, the conductivity increases with increasing $p(H_2O)$, and the conductivities were approximately proportional to $p(H_2O)^{1/2}$. These results coincide with the water vapor dependency of other rare earth ortho and metaphosphates (*62, 113*). However the results are contrary to the water vapor dependency of these materials in the literature (*16*). $p(H_2O)$ dependencies of the conductivity have been modeled assuming protons and oxygen vacancies are charge compensating the acceptors. At high $p(H_2O)$ acceptors are charge compensated by protons. At low $p(H_2O)$ the proton concentration decreases and the concentration of oxygen vacancies increase with increasing temperature. The extracted parameters from the modeling are reported in Table 5.4.

5.2.4 Transport number measurements

EMF measurements were carried out on the 2 mol-% Y-doped ZrP_2O_7 at 700 ^oC in wet oxygen to qualitatively determine the transport number of protons. These measurements involved measuring the voltage over the sample when exposed to two different $p(H_2O)$ while keeping the $p(O_2)$ the same on both sides. One of the water vapor pressures was always wet gas (0.025 atm), while the other came from increasingly drier gas. The average of the ionic transport number over the gradient used is the ratio of the measured voltage over the appropriate Nernst voltage. The transport numbers plotted against the logarithm of the ratio of the pressures is shown in Fig. 5.8. The transport number of protons decreases with increasing gradients. We attribute this to smaller average $p(H_2O)$ and thus smaller proton conduction with increasing gradient, and to larger leakage through unavoidable remaining sample porosity and imperfect gasket sealing. Thus, the proton transport number in wet oxygen at 700 ^oC obtained by extrapolation to zero gradient comes out as 0.65 and thus confirms that the material is mainly a proton conductor under these conditions. If the material is a pure proton conductor, the transport number is unity. The lowered transport number is typical of the effect of leakage between the gas chambers even at small gradients. We also measured the EMF of a cell exposed to a gradient in $p(O_2)$ (oxygen vs argon) at constant $p(H_2O)$ = 0.025 atm. We observed a transport number of 0.66, which is not significantly different from the protonic one. We have thus confirmed that the sample is mainly a proton conductor. This is in good agreement with the conductivity measurements of this material.

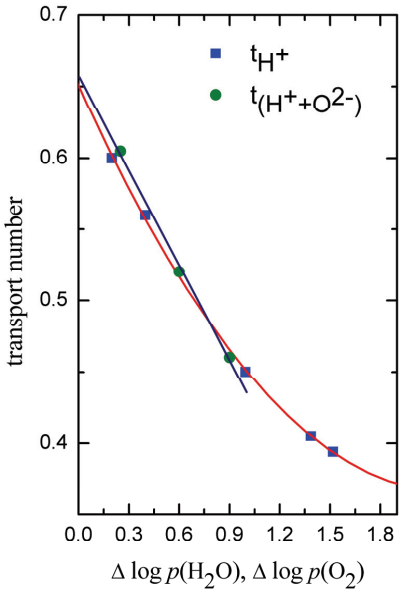

Fig. 5.8 Transport numbers versus logarithm of the ratio of the pressures of 2 mol-% Y-doped ZrP_2O_7 at 700 °C.

5.3 Thermogravimetric measurements

TGA experiments were carried out to investigate the water uptake in Fe-doped TiP_2O_7, Sc-doped SnP_2O_7 and Sr-doped LaP_3O_9. The standard hydration enthalpy of Fe-doped TiP_2O_7 was derived as −45 ± 5 kJ/mol at low temperature and −77 ± 15 kJ/mol at high temperature, for one mol of water assuming that protons are charge compensated by oxygen interstitials. The standard hydration enthalpy of Sc-doped SnP_2O_7 was derived as −40 ± 5 kJ/mol. The standard hydration enthalpy of Sr-doped LaP_3O_9 is evaluated as −67 ± 10 kJ/mol, for one mol of water assuming protons and oxygen vacancies are charge compensating the acceptors. The mobility of protons is derived by the combination of proton conductivity and thermodynamic parameters from thermogravimetric measurements and is listed also in Table 5.4. The $p(H_2O)$ dependency of pyrophosphates indicates that the protons dissolve in quantities exceeding the dopant level. According to our TG measurements at low temperature, proton concentration is higher than the concentration of acceptors while at high temperatures the proton concentration decreases below these levels. In rare earth oxides, the hydration enthalpies are moreover related to the stability of the

materials (*114*). Compared to oxides, phosphates are less stable and the hydration enthalpy correspondingly less negative. Hydration entropies are generally reported in the range −160 to −100 J/mol K, reflecting the entropy loss of one gas molecule for chemical reactions, empirically −120 J/mol K (*115*). In this respect the entropy of hydration of all the samples seems reasonable while in TiP_2O_7 at high temperature it is beyond the normal range due to more order created when water is incorporated.

Theoretically, the pre-exponential should approach ~1000 cm^2 K/V s for proton migration, but the effective attempt frequency and sticking probability tend to lower this value to 10−100 cm^2 K/V s (*116*). Hence the pre-exponentials of all the samples are reasonable.

Table 5.4 Thermodynamic and transport parameters derived from the modeling of thermogravimetry and conductivity results.

No.	Sample	Hydration entropy (ΔS^0)	Hydration enthalpy (ΔH^0)	Migration enthalpy of protons ($\Delta H_{m,H+}$)	Pre-exponential of proton mobility ($\mu_{0,H+}$)
		(J/mol K)	(kJ/mol)	(kJ/mol)	(cm^2 K/V s)
1	2 mol-% Fe-doped TiP_2O_7				
	(500−700 °C)	−147 ± 6	−40 ± 4	79 ± 3	470 ± 150
	(Cubic α-modification)				
	(700−1000 °C)	−185 ± 13	−77 ± 15	61 ± 5	58 ± 30
	(Cubic β- modification)				
2	2 mol-% Sc-doped SnP_2O_7	−140 ± 10	−40 ± 5	87 ± 3	22 ± 10
3	2 mol-% Sr-doped LaP_3O_9	−100 ± 10	−67 ± 10	50 ± 5	7 ± 3

In oxides and orthophosphates, the conductivity was increased by acceptor doping and the acceptors are charge compensated by protons and oxygen vacancies. Similarly in LaP_3O_9 the conductivity was drastically increased by Sr- doping. At low $p(H_2O)$, the conductivity increases with increasing $p(H_2O)$ and is proportional to approximately $p(H_2O)^{1/2}$. The water partial pressure dependence decrease as the amount of water vapor

increase and, seemingly, approaches a regime where the conductivity becomes $p(H_2O)$-independent. However, in TiP_2O_7, the conductivity was slightly increased by acceptor doping. Moreover the $p(O_2)$ and $p(H_2O)$ dependencies of the conductivities are similar for doped and undoped samples. The conductivity increases with increasing water vapor pressure and it is approximately proportional to $p(H_2O)^{1/3}$. In ZrP_2O_7 and SnP_2O_7 pyrophosphates the conductivity of the acceptor-doped samples is higher than the conductivity of the undoped one; however the $p(H_2O)$ and $p(O_2)$ dependencies are similar. It thus seems that the defect structure is not altered by acceptor doping or the acceptors are not fully and effectively dissolved. Hence, we believe the increased conductivity is related to the microstructure of the material. Because the materials are prepared by conventional and spark plasma sintering and the porosities are different. Our results indicate that the protons and oxygen interstitials dissolve in quantities exceeding the dopant level. This means that water dissolves as protons and some negative defect, for instance interstitial oxide ions. This has been suggested as a prevailing situation in undoped Y_2O_3, an oxide with native empty interstitial oxygen sites (*117*).

The conductivities of our samples (pyrophosphates) were several orders of magnitude lower than the literature values at low temperature. Impedance spectroscopy was performed on our samples at different temperatures in the frequency range of $5-10^6$ Hz. We observed only one semicircle and deconvoluted the plot using an equivalent circuit program. This showed that the AC conductivity at 10 kHz is mainly reflecting bulk - and possibly a grain boundary parallel contribution - but not grain boundary resistance or electrode responses. In tetravalent metal pyrophosphates remarkably high proton conductivity was reported at the temperature between 150 and 350 ^oC under water free conditions claimed to be resulting from hopping of protons introduced into the bulk through a reaction between water vapor, electron holes and oxygen vacancies (*11-13, 15*).

Tao (*73*) reported on the proton conductivity of SnP_2O_7 and In-doped SnP_2O_7 prepared by aqueous solution method. The conductivity of these materials were also several orders of magnitude lower than that of the literature values (*11*). Moreover, Xu et al. (*118*) reported that the conductivity of pure $Al(H_2PO_4)_3$ in air is in the order of $10^{-6}-10^{-7}$ S/cm between 100 and 200 ^oC. For samples containing small excess of H_3PO_4, a much higher conductivity was observed. The extra acid is found to play a key role in enhancing the conductivity of $Al(H_2PO_4)_3$-H_3PO_4 composite at the surface region of the $Al(H_2PO_4)_3$ in a core shell type behavior. 0.7 mol-% excess of H_3PO_4 can increase the conductivity by three orders of magnitude (*118*). Possible conducting paths within the

composite series are shown in Fig. 5.9. By considering the particles in a core shell structure, a conductive surface layer may connect together and bypass the particles of $Al(H_2PO_4)_3$.

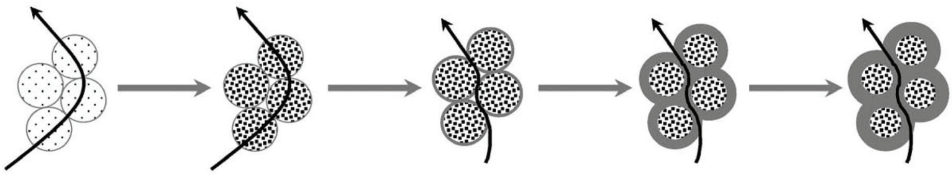

Fig. 5.9 Possible proton transfer paths of $Al(H_2PO_4)_3$-H_3PO_4 systems. The small circles represent the particles of $Al(H_2PO_4)_3$, while the shells represent the conductive layers formed by additional acid. Different defect concentration is expressed by the density of black dot in the circles. Possible paths are showed by arrows (*118*).

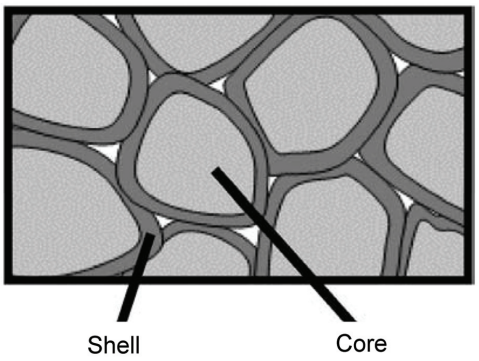

Fig. 5.10 Schematic image of core-shell type electrolytes (*119*).

H_3PO_4 precursor used in the acid route and insufficient annealing temperatures may also play important roles for the conductivity of pyrophosphates. The dominant conduction behavior is thought to change from grain interior conduction to surface/interfacial conduction. Shirai et al. (*118, 119*) explained that the conductivity in tetra valent pyrophosphates was related to the core-shell structure (Fig. 5.10). When heated above 700 ^oC the core-shell structure was completely removed and the sample becomes more crystalline. Our results serve to confirm this, and we may conclude that our samples not seem to have contained such an amorphous phase.

Chapter 6

Conclusions

Undoped and acceptor doped Ti, Zr and Sn pyrophosphates were prepared by the phosphoric acid route. Undoped and Sr-doped LaP_3O_9 were prepared by traditional solid state reaction method. The crystal structures of all the samples were analyzed by XRD. LaP_3O_9 was orthorhombic and all the pyrophosphates were cubic superstructures at room temperature and undergo a phase transition to a simpler cubic structure at high temperatures. The samples were fabricated by conventional and spark plasma sintering.

The AC conductivity of sintered samples of all phosphates increases with humidity and has a clear H/D isotope effect, which demonstrates that the conductivity is mainly protonic and that protons migrate through a hopping mechanism. The isotope effect is attributed to higher activation energy of the mobility of deuterons than of protons. The $p(O_2)$ dependence indicated that the materials are mainly ionic (proton) conductors and that n-type conductivity contributes significantly at high temperatures in reduced oxygen activities for TiP_2O_7 and SnP_2O_7.

The proton conductivity in pyrophosphates increases with increasing $p(H_2O)$, and were approximately proportional to $p(H_2O)^{1/3}$. The acceptor doping appears not to be significant for the defect structure. The conductivity has been modeled assuming that protons are charge compensated by oxygen interstitials.

In the metaphosphate, the conductivities were approximately proportional to $p(H_2O)^{1/2}$ and it has been modeled assuming that the acceptors are charge compensated by protons and oxygen vacancies.

Entropy and enthalpy of hydration of the samples have been deduced from thermogravimetric measurements of water uptake. Based on the modeling results, thermodynamic constants and transport parameters of proton mobility have been derived for acceptor doped materials.

Signs of abnormally high proton conductivities of pyrophosphates at low temperatures as reported in literature have not been observed. Extra phosphoric acid appears to play a key role in the conduction processes and water acts as another important

factor typically at lower temperatures. Modest stable proton conductivity was observed in pyrophosphate samples sintered at high temperatures.

Bibliography

1. W. R. Grove, *Phil. Mag.* **14**, 127 (1839).
2. B. C. H. Steele, *J. Mater. Sci.* **36**, 1053 (2001).
3. B. C. H. Steele, A. Heinzel, *Nature (London)* **414**, 345 (2001).
4. http://www.sintef.no/Home/Materials-and-Chemistry/Energy-Conversion-and-Materials/Materials-for-Energy-and-Environmental-Technology/Test/Proton-conducting-fuel-cells--PCFC/.
5. T. Norby, R. Haugsrud, *Nanoporus Inorganic Membranes*. A. F. Sammells, M. V. Mundsschau, Eds., (WILLEY-VCH Verlag GmbH&Co. KGaA Weinheim 2006).
6. H. Iwahara, H. Uchinda, K. Ono, K. Ogaki, *J. Electrochem. Soc.* **135**, 529 (1988).
7. S. M. Haile, D. A. Boysen, C. R. I. Chisholm, R. B. Merle, *Nature (London)* **410**, 910 (2001).
8. T. Norby, M. Friesel, B. E. Mellander, *Solid State Ionics* **77**, 105 (1995).
9. A. Pawlowski, M. Polomska, *Solid State Ionics* **176**, 2045 (2005).
10. J. Otomo, T. Tamaki, S. Nishida, S. Wang, M. Ogura, T. kobayashi, C. Wen, H. Nagamoto, H. Takahashi, *J. App. Electrochem.* 35, 865 (2003).
11. M. Nagao *et al.*, *J. Electrochem. Soc.* **153**, A1604 (2006).
12. M. Nagao *et al.*, *Electrochem. Solid-State Lett.* **9**, A105 (2006).
13. X. Sun *et al.*, *Solid State Ionics* **179**, 1138 (2008).
14. Y. Li, T. Kunitake, Y. Aoki, E. Muto, *Adv. Mater.* **20**, 2398 (2008).
15. A. Tomita, N. Kajiyama, T. Kamiya, M. Nagao, T. Hibino, *J. Electrochem. Soc.* **154**, B1265 (2007).
16. K. Amezawa, Y. Kitajima, Y. Tomii, N. Yamamoto, *Electrochem. Solid-State Lett.* **7**, A511 (2004).
17. G. Zhang *et al.*, *Solid State Ionics* **178**, 1811 (2008).
18. K. Amezawa, Y. Agari, N. Kitamura, Y. Uchimoto, Y. Tomii, *Proceedings of 16th Iketani Conference* 403 (2006).
19. E. Mollwo, *ZeitschriJ fur Phjjsik* **138**, 478 (1954).
20. D. G. Thomas, J. J. Lander, *J. Chem. Phy.* **25**, 1136 (1956).
21. V. Rudolph, *Z. Naturforsch* **A13**, 757 (1958).
22. S. Stotz, C. Wagner, *Ber. Bunsenges. Phys. Chem.* **70**, 781 (1967).
23. C. Wagner, *Ber. Bunsenges. Phys. Chem.* **72**, 778 (1968).

24. G. J. Hill, *Br. J. Appl.Phys.* **1**, 1151 (1968).
25. J. B. Bates, J. C. Wang, R. A. Perkins, *Phys. Rev. B* **19 [18]**, 4130 (1979).
26. J. C. Cathcart, R. A. Perkins, J. B. Bates, L. C. Manley, *J. Appl. Phys.* **50 [6]**, 4110 (1979).
27. W. G. Buckman, *J. Appl. Phys.* **43 [2]**, 1280.
28. D. A. Shores, R. A. Rapp, *J. Electrochem. Soc.* **119**, 300 (1972).
29. J. M. Pope, G. Simkovich, *Materials Res. Bull.* **9**, 1111 (1974).
30. T. Takahashi, H. Iwahara, *Revue de Chirnie Minerale* **17**, 243 (1980).
31. H. Iwahara, H. Uchida, S. Tanaka, *Solid State Ionics* **9-10**, 1021 (1983).
32. K. C. Liang, A. S. Nowick, *Solid State Ionics* **61**, 77 (1993).
33. K. C. Liang, Y. Du, A. S. Nowick, *Solid State Ionics* **69**, 117 (1994).
34. K. D. Kreuer, *Solid State Ionics* **125**, 285 (1999).
35. H. G. Bohn, T. Schober, T. Mono, W. Schilling, *Solid State Ionics* **117**, 219 (1999).
36. Y. Du, A. S. Nowick, *Solid State Ionics* **91**, 85 (1996).
37. K. D. Kreuer, *Solid State Ionics* **97**, 1 (1997).
38. T. Schober, *Solid State Ionics* **109**, 1 (1998).
39. D. J. D. Corcoran, J. T. S. Irvine, *Solid State Ionics* **145**, 307 (2001).
40. A. S. Nowick, Y. Du, K. C. Liang, *Solid State Ionics* **125**, 303 (1999).
41. R. Haugsrud, T. Norby, *Nature Mater.* **5**, 193 (2006).
42. S. Li, F. Schonberger, P. Slater, *Chem. Comm.* **21**, 2694 (2003).
43. F. Schonberger, E. Kendrick, M. S. Islam, P. R. Slater, *Solid State Ionics* **176**, 2951 (2005).
44. G. B. Zhang, D. M. Smyth, *Solid State Ionics* **82**, 153 (1995).
45. K. Kakinuma, A. Tomita, H. Yamamura, T. Atake, *J. Mater. Sci.* **41**, 6435 (2006).
46. T. Shimura, M. Komori, H. Iwahara, *Solid State Ionics* **86-88**, 685 (1996).
47. T. Omata, S. O. Y. Matsuo, *J. Electrochem. Soc.* **148**, E252 (2001).
48. T. Shimura, S. Fujimoto, H. Iwahara, *Solid State Ionics* **143**, 117 (2001).
49. R. Q. Liu, Y. H. Xie, J. D. Wang, Z. J. Li, B. H. Wang, *Solid State Ionics* **177**, 73 (2006).
50. T. Norby, *Korean J. Ceramics* **4**, 128 (1998).
51. T. Norby, O. Dyrlie, P. Kofstad, *Solid State Ionics* **53-56**, 446 (1992).
52. Y. Larring, T. Norby, *Solid State Ionics* **77**, 338 (1995).
53. Ph. Colomban, A. Novak, *Chemistry of Solid State Materials, Proton Conductors*, Cambridge University Press, Cambridge, **2**, pp.165-182 (1992).

54. A. I. Baranov, V. P. Khiznichenko, V. A. Sandler, L. A. Shuvalov, *Ferroelectrics* **81**, 183 (1988).
55. F. Romain, A. Novak, *J. Mol. Struct.* **263**, 69 (1991).
56. W. Bronowska, *J. Chem. Phys.* **114**, 611 (2001).
57. J. Otomo, N. Minagawa, C. Wen, K. Eguchi, H. Takahashi, *Solid State Ionics* **156**, 357 (2003).
58. N. Kitamura *et al.*, *Solid State Ionics* **177**, 2369 (2006).
59. K. Amezawa, Y. Uchimoto, Y. Tornii, *Solid State Ionics* **177**, 2407 (2006).
60. K. Amezawa, Y. Nishikawa, Y. Tomii, N. Yamamoto, *J. Electrochem. Soc.* **152**, A1060 (2005).
61. T. Norby, N. Christiansen, *Solid State Ionics* **77**, 240 (1995).
62. K. Amezawa, H. Mackawa, Y. Tomii, N. Yamamoto, *Solid State Ionics* **145**, 233 (2001).
63. K. Amezawa, Y. Tomii, N. Yamamoto, *Solid State Ionics* **162-163**, 175 (2003).
64. N. Kitamura, K. Amezawa, Y. Tomii, N. Yamamoto, *Solid State Ionics* **162-163**, 161 (2003).
65. S. Gallini, M. Hansel, T. Norby, M. T. Colomer, J. R. Jurado, *Solid State Ionics* **162-163**, 167 (2003).
66. N. Kitamura *et al.*, *J. Electrochem. Soc.* **152**, A658 (2005).
67. K. Amezawa, Y. Tomii, N. Yamamoto, *Solid State Ionics* **176**, 143 (2005).
68. K. Amezawa *et al.*, *Solid State Ionics* **176**, 2867 (2005).
69. N. Sharova, H. Fjellvåg, T. Norby, *Solid State Ionics* **180**, 117 (2009).
70. G. Zhang, E. D. Wachsman, J. C. Nino, *ECS Transactions* **1**, 357 (2006).
71. G. Harley, R. Yu, L. C. De Jonghe, *Solid State Ionics* **178**, 769 (2007).
72. M. Greenblatt, P. P. Tsai, T. Kodama, S. Tanase, *Solid State Ionics* **40-41**, 444 (1990).
73. S. Tao, *Solid State Ionics* **180**, 148 (2009).
74. A. R. West, *Solid State Chemistry and its Applications*, ISBN:0-471-90377-9.
75. J. Gopalakrishnan, C. Nagesa, R. Rao, Eds., *New Directions in Solid State Chemistry*, (Cambridge University Press, 230 (1997).
76. R. J. D. Tilley, *Defect Crystal Chemistry and its Applications*, ISBN:0-412-031331-2J.
77. K. D. Kreuer, *Chemistry of Materials* **8**, 610 (1996).
78. T. Norby, *Solid State Ionics* **125**, 1 (1999).

79. P. Kofstad, T. Norby, *Defects and Transport in crystalline solids*.
80. W. K. Lee, A. S. Nowick, L. A. Boatner, *Solid State Ionics* **18-19**, 989 (1986).
81. R. C. T. Slade, N. Singh, *J. Mater. Chem.* **1**, 441 (1991).
82. N. Bonanos, *Solid State Ionics* **53-56**, 967 (1992).
83. A. S. Nowick, A. V. Vaysleyb, *Solid State Ionics* **97**, 17 (1997).
84. R. P. Bell, in *The Tunnel Effect in Chemistry*. (Chapman and Hall, London, 1980).
85. T. Scherban, A. S. Nowick, *Solid State Ionics* **35**, 189 (1989).
86. T. Norby, *Solid State Ionics* **125**, 1 (2000).
87. H. Iwahara, T. Shimura, H. Matsumoto, *Electrochemistry* **68**, 154 (2000).
88. T. Norby, P. Kofstad, *J. Am. Ceram. Soc.* **69**, 780 (1986).
89. R. Glöckner, Doctor Scientiarum thesis, *Dissolution and transport of protons in some perovskite-related oxides*, Faculty of mathematics and natural sciences, University of Oslo, ISSN:1501-7710 No. 82 (2000).
90. J. Ross, M. Donald, *Impedance Spectroscopy*,Wiely (1987).
91. T. Norby, *Solid State Ionics* **28-30**, 1586 (1988).
92. D. P. Sutija, T. Norby, P. Björnbom, *Solid State Ionics* **77**, 167 (1995).
93. M. Kakihana, M. Yoshimura, *Bull. Chem. Jpn.* **72**, 1427 (1999).
94. B. L. Gabriel, *SEM: A User's Manual for Materials Science*, ISBN:0-87 170-202-9.
95. H. M. Rietveld, *J. Appl. Crystallogr.* **2**, 65 (1969).
96. R. A. Young, *The Rietveld Method*, ISBN:0-19-85557-6 (1993).
97. J. R. Carvajal, *Physica B* **192**, 55 (1993).
98. B. H. Toby, *J. Appl. Cryst*., **34**, 210 (2001).
99. A. C. Larson, R. B. Von Dreele, *General Structure Analysis System (GSAS)*, *Report Laur*, Los Alamos National Lab, pp. 86-748 (2000).
100. P. E. Champness, *Electron Diffraction in the Transmission Electron Microscope,* BIOS Scientific Publisher Limited (2001).
101. A. Olsen, *The theory and practice of Analytical Electron Microscopy in Materials Science,* University of Oslo (2002).
102. Netzsch, *Proteus-Thermal Analysis* V 4.8.5 Manual (2008).
103. http://www.norecs.com/.
104. T. Norby, *Impedance Spectroscopy,* Internal report.
105. T. Norby, P. Kofstad, *J. Am. Ceram. Soc.* **67**, 786 (1984).
106. Y. Larring, Doctor Scientiarum thesis, *Protons and oxygen vacancies in acceptor substituted rare earth oxides,* Faculty of mathematics and natural sciences,

University of Oslo (1998).
107. T. Norby, *GASMIX,* Internal report.
108. N. G. Chernorukov, M. I. Zhuk, E. P. Moskvichev, *Tr. Khim. Tekh.* **3**, 9 (1974).
109. V. Nalini, M. H. Sørby, K. Amazawa, R. Haugsrud, H. Fjellvåg, T. Norby, Structure, water uptake and electrical conductivity of TiP_2O_7, Submitted to *J. Am. Ceram. Soc.* (2010).
110. R. L. Withers, Y. Tabira, J. S. O. Evans, I. J. King, A. W. Sleight, *J. Solid State Chem.* **157**, 186 (2001).
111. R. K. B. Gover, N. D. Withers, S. Allen, R. L. Withers, J. S. O. Evans, *J. Solid State Chem.* **166**, 42 (2002).
112. K. D. Kreuer, *Chem. Mat.* **8**, 610 (1996).
113. K. Amezawa, Y. Agari, N. Kitamura, Y. Uchimoto, Y. Tomii, *Proc. 16th Iketani Conference*, 403 (2006).
114. Y. Larring, T. Norby, *Solid State Ionics* **97**, 523 (1997).
115. T. Norby, M. Widerøe, R. Glöckner, Y. Larring, *Dalton Trans.* **19**, 3012 (2004).
116. T. Norby, *Perovskite oxide for solid oxide fuel cells*, T. Ishihara, Ed., Springer, ISBN: 978-0-387-77707-8, pp. 217-241 (2009).
117. T. Norby, P. Kofstad, *J. Am. Ceram. Soc.* **69**, 780 (1986).
118. X. Xu, S. Tao, J. T. S. Irvine, *Solid State Ionics* **180**, 343 (2009).
119. T. Shirai, S. Satou, M. Saito, J. Kuwano, H. Shiroishi, *Solid State Ionics* **180,** 569 (2009).

List of publications and manuscripts

1) **V. Nalini,** R. Haugsrud, T. Norby, "High-temperature proton conductivity and defect structure of TiP_2O_7", *Solid State Ionics* **181,** 510 (2010).

2) **V. Nalini,** K. Amezawa, W. Xing, T. Norby, "High-temperature proton conductivity of ZrP_2O_7", *J. Electrochem. Soc.* **157,** B1491 (2010).

3) **V. Nalini,** R. Haugsrud, T. Norby, "Defects and transport properties of Sr-doped LaP_3O_9", *Solid State Ionics* **181,** 1264 (2010).

4) **V. Nalini,** M. H. Sørby, K. Amezawa, R. Haugsrud, H. Fjellvåg, T. Norby, "Structure, water uptake and electrical conductivity of TiP_2O_7", Submitted to *J. Am. Ceram. Soc*. (2010).

5) **V. Nalini,** L. Jantsky, R. Haugsrud, T. Norby, "Synthesis and electrical characterization of SnP_2O_7", Manuscript.

Related publications not included in this thesis

1) **V. Nalini,** A. M. Anuradha, T. Norby, "Protonic conduction in TiP_2O_7", *Solid State Ionics: Advanced Materials for Emerging Technologies, Proc. 10th Asian Conference,* Kandy, Sri Lanka, 321-328 (2006).

2) T. Norby, R. Haugsrud, **V. Nalini**, "New proton conducting materials for fuel cells and hydrogen separation membranes", *Proc. 9th International Conference on Inorganic Membranes*, Oslo: SINTEF, ISBN 978-82-14-04026-5, 260-267 (2006).

I

High-temperature proton conductivity and defect structure of TiP_2O_7

Vajeeston Nalini, Reidar Haugsrud, Truls Norby

Solid State Ionics **181,** 510 (2010).

High-temperature proton conductivity of ZrP_2O_7

Vajeeston Nalini, Koji Amezawa, Wen Xing, Truls Norby

J. Electrochem. Soc. **157,** B1491 (2010).

II

Journal of The Electrochemical Society, **157** (10) B1491-B1498 (2010)
0013-4651/2010/157(10)/B1491/8/$28.00 © The Electrochemical Society

High Temperature Proton Conductivity of ZrP_2O_7

Vajeeston Nalini,[a,z] Koji Amezawa,[b] Wen Xing,[a] and Truls Norby[a,*,z]

[a]*Centre for Materials Science and Nanotechnology, FERMiO, Department of Chemistry, University of Oslo, NO-0349 Oslo, Norway*
[b]*Graduate School of Environmental Studies, Tohoku University, Sendai 980-8579, Japan*

Undoped ZrP_2O_7 and 2 mol % Sc-, Y-, and La-doped ZrP_2O_7 have been synthesized by an aqueous phosphoric acid route and characterized by X-ray diffraction and scanning electron microscopy. The samples were fabricated by conventional and spark plasma sintering (SPS), and the electrical conductivity was examined from 500 to 1000°C as a function of $p(O_2)$ and $p(H_2O)$ or $p(D_2O)$ by impedance spectroscopy. The conductivity of the materials in H_2O was higher than in D_2O and dry atmospheres, indicating that proton conductivity is dominant, supported also by transport number measurements. The conductivity was independent of $p(O_2)$ at all temperatures, showing that the conductivity is predominantly ionic (protonic) under oxidizing as well as more reducing conditions. The $p(H_2O)$ and temperature dependencies of the conductivity were modeled assuming that protons are charge-compensated by oxygen interstitials. The attempted acceptor doping does not influence the conductivity significantly. Less dense samples exhibit a conductivity contribution at low temperatures assigned to internal surfaces; this is avoided in the SPS samples.
 [DOI: 10.1149/1.3474942]

Manuscript submitted March 25, 2010; revised manuscript received July 11, 2010. Published August 26, 2010.

The development of a clean, sustainable hydrogen economy requires the development of fuel cells and electrolyzers. Also, better use of fossil fuels in the next 100 years may require the use of fuel cells combined with O_2 separation and H_2 separation gas separation membranes for CO_2 sequestration. Fuel cells and electrolyzers rely on oxygen ion or proton conductors, while gas separation membranes may be realized with mixed ionic/electronic conductors. For these purposes, materials that exhibit high proton conductivity and are thermodynamically stable are in demand. A leading candidate class comprises acceptor-substituted perovskite oxides that become hydrated and proton conducting in the presence of water vapor at high temperatures.[1-6] Certain acidic oxyacid salts such as hydrogen sulfates, selenates, arsenates, and phosphates are good proton conductors at moderate temperatures,[7-10] but their use is limited by modest thermal stabilities toward reducing (fuel) conditions.

Recently, remarkably high proton conductivities have been reported in tetravalent metal pyrophosphates (MP_2O_7) at temperatures between 150 and 350°C under nominally water-free conditions. The conductivity has been attributed to the hopping of protons introduced through a reaction between water vapor and electron holes or oxygen vacancies.[11-14] These papers motivated further studies aimed at understanding the proton conduction of pyrophosphates at high temperatures. Li et al.[15] reported that 5 mol % Y-doped ZrP_2O_7 with deliberate precursor excess of phosphorous (atomic ratio P/(Zr + Y) = 3) showed high proton conductivity of 1.5×10^{-4} S/cm at 340°C. Alberti et al.[16,17] reported that the conductivity of ZrP_2O_7 increases from 10^{-7} to 10^{-3} S/cm at 20°C when the relative humidity increases from 20 to 90%. Shirai et al.[18,19] found that the high conductivity was related to an amorphous shell around the grain cores. When heated above 700°C, the shell structure is removed and the sample becomes more crystalline and less conductive. Tao[20] reported that the proton conductivity of In-doped SnP_2O_7 prepared by an aqueous solution method was several orders of magnitude lower than those reported for samples prepared by traditional routes.[11] It was concluded that the H_3PO_4 precursor used in the traditional acid route together with insufficient annealing temperatures may play a role in the abnormally high conductivity sometimes reported for pyrophosphates.

We have reported earlier a modest proton conductivity of TiP_2O_7 and Al-doped TiP_2O_7 at high temperatures.[21] In the present contribution, we describe the synthesis, sintering, and characterization of ZrP_2O_7 and the 2 mol % Sc-, Y-, and La-doped ZrP_2O_7 and report their high temperature electrical properties. In ZrP_2O_7, as in other pyrophosphates, densification by conventional sintering is difficult because of the thermal decomposition of the compound and volatility of phosphorous oxides at the high temperatures required. Hence, spark plasma sintering (SPS) was applied to some of the samples (undoped and 2 mol % Y-doped ZrP_2O_7). This relatively new sintering process generally enables high densification of metals and ceramics at relatively low temperatures within a very short time compared to conventional sintering. In the SPS process, material powder is packed in a graphite die and pressed uniaxially at typically 30–50 MPa while a pulsed dc current is passed through the specimen. The pulsed current applied momentarily generates local electrical spark discharges and high temperature between specimen particles and also heats the graphite die by joule heating. In this way, the powder is heated from both inside and outside, promoting material flow, accelerating densification, shortening sintering time, and reducing loss of volatile species such as phosphorous.

To understand the proton conduction mechanism in this compound and how it varies upon acceptor doping, we have studied the electrical conductivity in H_2O- and D_2O-containing as well as dry atmospheres, measured $p(H_2O)$ dependencies, and done a qualitative test of protonic and ionic transport numbers by the concentration cell electromotive force (emf) method. The results are discussed in terms of a defect chemical model, and we start with a theoretical treatment of this, as it is not commonly described for pyrophosphates.

Theory

Defect chemistry.— In ZrP_2O_7, the pyrophosphate group, $P_2O_7^{4-}$, is the host anion. It may be hydrated to form hydrogen pyrophosphate defects at pyrophosphate sites denoted as $(HP_2O_7)^{\bullet}_{P_2O_7}$. These may charge compensate acceptor dopants. However, our results indicate that the protons dissolve in quantities exceeding the dopant level. This means that water dissolves as protons and some negative defect, for instance, an interstitial oxide ion. In a pyrophosphate, the interstitial oxygen may be denoted as phosphate ions at pyrophosphate sites $(2PO_4)''_{P_2O_7}$. The hydration reaction in this case can be written as

$$3(P_2O_7)^{x}_{P_2O_7} + H_2O_{(g)} = (2PO_4)''_{P_2O_7} + 2(HP_2O_7)^{\bullet}_{P_2O_7} \quad [1]$$

with the equilibrium constant expressed as

$$K = \frac{[(2PO_4)''_{P_2O_7}][(HP_2O_7)^{\bullet}_{P_2O_7}]^2}{[(P_2O_7)^{x}_{P_2O_7}]^3 p(H_2O)} = \exp\left(\frac{\Delta S^0}{R}\right)\exp\left(\frac{-\Delta H^0}{RT}\right) \quad [2]$$

* Electrochemical Society Active Member.
z E-mail: vajeesn@kjemi.uio.no; truls.norby@kjemi.uio.no

in which brackets denote volume concentrations or mole fractions and the partial pressure is given in bar (≈atm). With these as the dominating defects, the electroneutrality condition can be written as

$$2[(2PO_4)''_{P_2O_7}] = [(HP_2O_7)^{\bullet}_{P_2O_7}] \quad [3]$$

The combination of the equilibrium constant and the electroneutrality condition yields the following expression for the concentration of the protons

$$[(HP_2O_7)^{\bullet}_{P_2O_7}] = 2^{1/3}K^{1/3}p(H_2O)^{1/3} = c_{0,H^+}\exp\left(\frac{-\frac{1}{3}\Delta H^0}{RT}\right)p(H_2O)^{1/3} \quad [4]$$

where c_{0,H^+} is the pre-exponential collection of terms for the proton concentration and ΔH^0 is the standard enthalpy change in the hydration reaction in Eq. 1.

The conductivity contribution from a charge carrier species i can be expressed as

$$\sigma_i = z_i e c_i \mu_i \quad [5]$$

where z_i is the absolute charge of the species, e the elementary charge (C), c_i the concentration (cm^{-3}), and μ_i the mobility (cm^2/Vs). The charge mobility of the diffusing species such as protons is given by

$$\mu_i = \mu_{0,i}\frac{1}{T}\exp\left(\frac{-\Delta H_{m,i}}{RT}\right) \quad [6]$$

where $\mu_{0,i}$ is the pre-exponential of charge mobility (cm^2 K/Vs) and $\Delta H_{m,i}$ is the enthalpy of migration. By combining the expressions for the concentration and mobility of protons, we get the proton conductivity

$$\sigma_{H^+} = zec_{0,H^+}\mu_{0,H^+}p(H_2O)^{1/3}\frac{1}{T}\exp\left(\frac{-\left(\frac{1}{3}\Delta H^0 + \Delta H_{m,H^+}\right)}{RT}\right) = \sigma_{0,H^+}p(H_2O)^{1/3}\frac{1}{T}\exp\left(\frac{-\Delta H_{H^+}}{RT}\right) \quad [7]$$

where μ_{0,H^+} is the pre-exponential and ΔH_{H^+} is the effective activation enthalpy of proton conductivity, having contributions from hydration thermodynamics and proton mobility.

Experimental

Materials preparation and phase characterization.— Undoped ZrP_2O_7 was prepared according to a procedure given elsewhere[22] by mixing nominal amounts of ZrO_2 (99.99%, Aldrich) and 85 wt % H_3PO_4 (99.999%, Aldrich) at room temperature until a homogeneous slurry was formed and subsequently heated at 200°C for 3 h. The obtained thick gel was further dried at 100°C for 24 h, ground, and calcined at 400°C for 1 h. The phase purity of the product was confirmed by powder X-ray diffraction (PXRD) at ambient temperature using a Siemens D5000 diffractometer with Bragg–Brentano geometry, variable slit, a position sensitive detector, and Cu $K\alpha_1$ radiation (λ = 1.5406 Å). Unit cell parameters were obtained from a least-squares fitting of all peak positions. 2 mol % Sc-, Y-, and La-doped ZrP_2O_7 were synthesized by mixing appropriate amounts of ZrO_2 and 85 wt % H_3PO_4 with high purity Sc_2O_3, Y_2O_3, and La_2O_3, respectively. The atomic ratio of the sum of the acceptor (Sc, Y, and La) and Zr to P was kept exactly at 1:2. The Sc- and La-doped ZrP_2O_7 powders were cold-pressed to disks of 13 mm diameter and ~2.5 mm thick. The thermal decomposition of ZrP_2O_7 was studied by heating at 1200°C for 30 h (see Results section). To avoid such thermal decomposition during sintering, the Sc- and La-doped samples were sintered at only 1000°C for 3 h, and the relative densities were around 75%, obtained from the lattice parameters and mass and dimensions of the disks.

The undoped and 2 mol % Y-doped ZrP_2O_7 samples were made by SPS at 30 MPa for 5 min with heating rates of 100 K/min. We sintered the doped sample at 1100, 1200, and 1250°C, achieving relative final densities of 86, 89, and 92%, respectively. The undoped ZrP_2O_7 was sintered at 1100°C and achieved 80% relative density. The microstructure and porosity of the samples were analyzed by a scanning electron microscope (SEM, FEI Quanta 200F), while chemical analysis in the SEM was obtained by an energy-dispersive X-ray spectrometer (EDS, EDAX Pegasus 2200).

Electrical characterization.— Electrodes of 10 mm diameter were applied to the disk sample faces by painting two layers of platinum paint (Metalor, Pt A3788A) on each side. A platinum mesh (0.09 mm thread) was fastened to each electrode by immersing and firing it into the first layer of platinum paint. The specimens with electrodes were annealed at 900°C for 2 h to remove organic residues from the ink. For conductivity measurements under reducing conditions, the Au electrodes were attached to each side of the specimen by painting three layers of gold ink (Engelhard, T-10112-gold paste) followed by annealing the sample at 900°C for 1 h. The electrical characterization was carried out in a ProboStat measurement cell (NorECs, Norway) with a two-electrode four-wire setup using a Hewlett-Packard 4192A impedance analyzer. Conductivities were generally obtained at 10 kHz and an oscillation voltage of 1.1 V (root-mean-square). Impedance spectroscopy was performed at different temperatures in the frequency range 5–10^6 Hz to establish the contributions of bulk, grain boundaries, and electrode resistance. Deconvolution of the impedance spectra was done using the EQUIVCRT software.[23] The conductivities were calculated based on the area of the electrodes and thickness of the sample and are corrected for sample porosity using the simple first approximation empirical relationship $\sigma = \sigma_m/d^2$ based on the data from Ref. 24 where σ_m is the measured conductivity and d is the relative density. The conductivity was measured over the temperature range 500–1000°C in various oxygen and water vapor partial pressures under oxidizing and reducing conditions obtained by using pure O_2 and Ar/O_2 and Ar/H_2 gas mixtures. Water vapor partial pressure was varied from "dry" (empirically ~6×10^{-5} atm) to "wet" (0.025 atm) by mixing gas dried over P_2O_5 and gas wetted by bubbling through pure water and then a saturated solution of $KBr_{(aq)}$ at room temperature. To confirm protonic conduction, conductivity under a D_2O atmosphere obtained in a corresponding manner was also measured. $p(D_2O)$ over a saturated solution of KBr in D_2O is not exactly the same as $p(H_2O)$ over a corresponding H_2O-based solution, but this is considered a minor difference here as long as we use the isotope effect in a qualitative manner only.

For transport number measurements, a 1 mm thick gold ring was placed as the sealing gasket between the specimen and the support tube. By an outer closed alumina tube, the cell then forms two gas volumes separated by the specimen. Electrode leads from the cell base were attached to the circular electrodes on the specimen from underneath inside the inner compartment and on top of the specimen from the outer gas compartment. A spring loaded alumina assembly held the parts together to maintain contact between the Pt leads and the electrodes and to facilitate the gold ring sealing. The gold ring softened and sealed after heating to ~1060°C. The inner and outer compartments were connected to a gas mixer to establish well-defined partial pressures and gradients of oxygen and water vapor across the specimen. The voltages resulting from the differences in the chemical potentials across the specimen induced by gas partial pressure gradients were measured with a Schlumberger Solartron 7150 Plus high impedance voltmeter. The proton transport numbers were obtained from the voltage over the sample when exposed to two different water vapor partial pressures while keeping the oxygen partial pressure the same on both sides. One of the gases was always fully wetted (pH_2O) = 0.025 atm), while the other was increas-

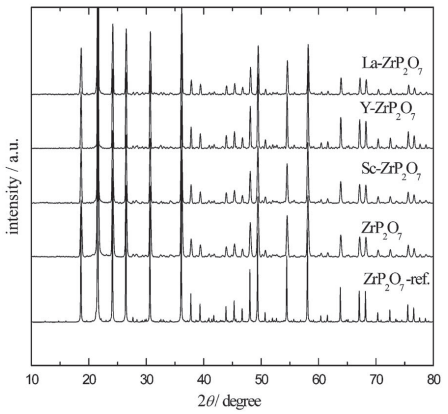

Figure 1. PXRD pattern for ZrP_2O_7 from Ref. 27, observed PXRD patterns of ZrP_2O_7, 2 mol % Sc-doped, 2 mol % Y-doped, and 2 mol % La-doped ZrP_2O_7 after sintering.

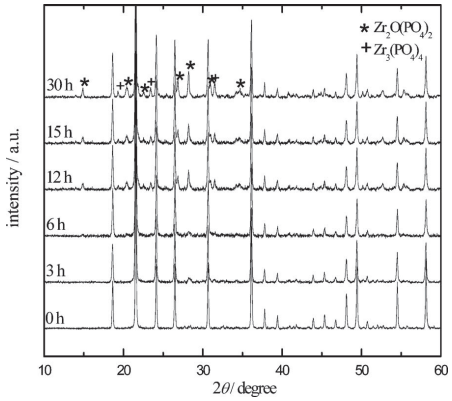

Figure 2. PXRD patterns for ZrP_2O_7 after heat-treatments at 1200°C for 0, 3, 6, 12, 15, and 30 h.

ingly drier by mixing in more dry gas. Similarly, the total ionic transport number was obtained from the voltage over the sample exposed to two gases of different contents of oxygen in Ar, both fully wetted.

Offset voltages were eliminated by reversing the gradient, recording the new voltage (which was close to the negative of the first), subtracting this reverse voltage from the forward voltage to obtain the sum of the absolute voltages, and dividing the result by 2. The offset was negligibly small anyway, as a result of the elimination of thermoelectrical contributions by careful centering of the sample in the hot zone of the furnace.

The ratio of the measured voltage over the Nernst voltage represents the average proton transport number over the gradient applied. Further details concerning the theory and experimental setup for transport number measurements of this kind are described and discussed elsewhere.[25,26]

Results and Discussion

Structural and thermal characterization.— Figure 1 shows the room-temperature PXRD patterns of ZrP_2O_7 and 2 mol % Sc-, Y-, and La-doped ZrP_2O_7 after sintering. These revealed that single-phase ZrP_2O_7 with cubic superstructure was formed in all cases, and the patterns match those from the study by Khosrovani et al.[27] This room temperature superstructure is reported to transform to another modulated cubic structure at ~290°C.[28] For undoped ZrP_2O_7, we obtained a = 24.717(1) Å (space group $Pa\bar{3}$, no. 205), in reasonable agreement with the literature value a = 24.7423 Å.[27] The lattice parameters for 2 mol % Sc-, Y-, and La-doped ZrP_2O_7 were 24.706(3), 24.7213(9), and 24.7158(6) Å, respectively. The ionic radii with coordination number 6 of Zr^{4+}, Sc^{3+}, Y^{3+}, and La^{3+} ions are 0.790, 0.732, 0.893, and 1.061 Å, respectively,[29] and in accordance with this, the lattice parameters for the Sc- and Y-doped ZrP_2O_7 were lower and higher, respectively, than for the undoped material. In the La-doped ZrP_2O_7, the lattice parameter was not significantly different than in the undoped material, suggesting that La^{3+} may have dissolved to a lesser extent.

The PXRD patterns for ZrP_2O_7 after heat-treatments at 1200°C for 3, 6, 12, 15, and 30 h are given in Fig. 2. For all of the heat-treated samples, diffraction peaks assigned to the orthorhombic $Zr_2O(PO_4)_2$ and $Zr_3(PO_4)_4$ were observed in addition to the peaks of ZrP_2O_7. With increasing time, peak intensities for the decomposition products increased. These results suggest that the thermal decomposition of ZrP_2O_7 can be expressed by

$$3ZrP_2O_7 \rightarrow Zr_3(PO_4)_4 + P_2O_{5(g)} \quad [8]$$

$$2ZrP_2O_7 \rightarrow Zr_2O(PO_4)_2 + P_2O_{5(g)} \quad [9]$$

Figure 3 shows the PXRD patterns for ZrP_2O_7 after SPS at 1100, 1200, and 1250°C. Additional peaks of orthorhombic $Zr_2O(PO_4)_2$ can be identified at the two highest temperatures and increases with temperature. Hence, samples spark plasma sintered at 1100°C were used for the conductivity measurements. Figure 4a-d shows the surface morphologies of the materials after sintering. The particle size ranged from 0.5 to 2.5 μm for the undoped and La-doped samples, while for the Sc- and Y-doped samples, the grain sizes are larger (in the order of few micrometers) and the density of the Y-doped sample (~86%) is higher than that of the other samples. No secondary phase was observed by SEM in any of the samples, but the large porosities make this assessment uncertain. The EDS analysis con-

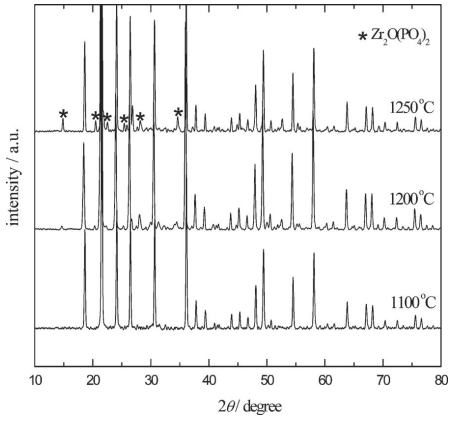

Figure 3. PXRD patterns for ZrP_2O_7 after SPS at 1100, 1200, and 1250°C.

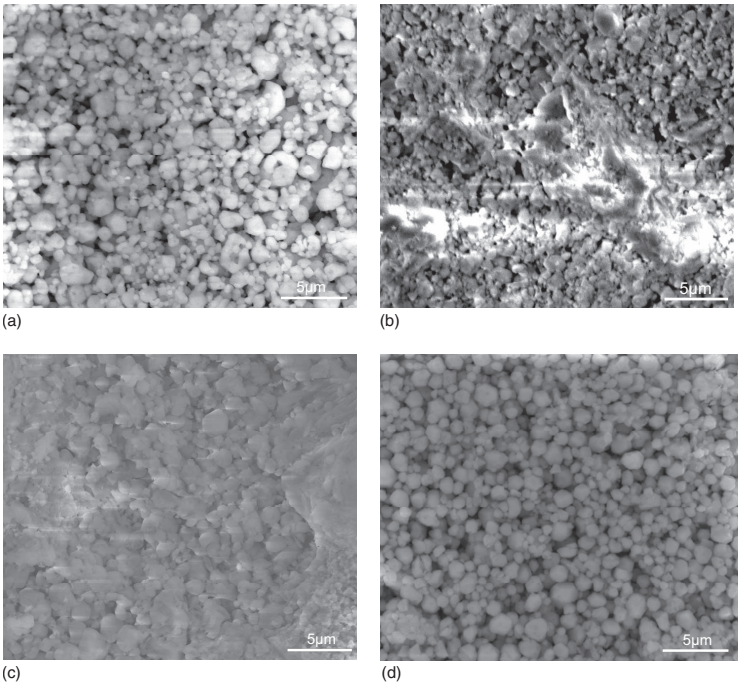

Figure 4. Surface morphology of (a) ZrP_2O_7 mixture of BSE and SE image, (b) 2 mol % Sc-doped (SE), (c) 2 mol % Y-doped ZrP_2O_7 (SE), and (d) 2 mol % La-doped ZrP_2O_7 (mixture of BSE and SE) after sintering.

firmed within its considerable uncertainty that Zr:P, (Zr+Sc):P, (Zr +Y):P, and (Zr+La):P ratios were all close to 1:2.

Conductivity measurements.— The conductivities of the materials vs inverse temperature in wet (H_2O or D_2O) and dry oxygen atmospheres are shown in Fig. 5a-d. Each curve is obtained during a slow cooling ramp of 18°C/h after equilibration at 1000°C. The substitution of Zr^{4+} by Sc^{3+} and Y^{3+} appears to have increased the conductivity of ZrP_2O_7 like acceptor doping does in rare-earth phosphates,[30-33] in contrast to substitution by La^{3+}. However, we shall see that these differences are probably related to sample density and microstructure more than doping.

The conductivity of the materials in the wet (H_2O-containing) atmosphere was significantly higher than in the dry and in D_2O-containing wet atmosphere, showing that the materials dominantly conduct protons in a wet atmosphere. The activation energies of proton and deuteron conduction from the ramps, the isotope ratios of the conductivities $\sigma(H_2O)/\sigma(D_2O)$, and the isotope ratios of pre-exponentials A_H/A_D for all the samples are presented in Table I. The activation energy values are at the same level as the activation energies in other pyrophosphates, for instance, 68 kJ/mol for TiP_2O_7 (below its phase transition temperature).[21] The presence of a clear isotope effect suggests that the transfer of protons in the materials takes place by a Grotthuss hopping mechanism. The activation energy for the deuteron conduction for all the samples was higher than that of the proton conduction, suggesting a semiclassical behavior in the proton hopping process in the material, similar to most of the proton conducting oxides and phosphates.[34-36] The isotope ratio of the pre-exponentials (A_H/A_D) is close to and not higher than unity, indicating that the isotope effect does not have a classical contribution as is also probably the case in most proton conducting oxides.[34]

Figure 5 shows that the temperature dependency of the conductivity is different for the more porous samples (undoped and Sc- and La-doped ZrP_2O_7) compared to the more dense spark plasma sintered Y-doped ZrP_2O_7, the former having an upward tail at low temperatures. This is likely due to the contribution of surface conduction in internal pores. The temperature dependency of Y-doped ZrP_2O_7 (in wet oxygen atmosphere) has been modeled assuming a single activated contribution, as shown in Fig. 5c. The measured conductivity curve exhibits a slight bend at the highest temperatures. This may be due to the approach of a new defect situation. The temperature dependency of Sc-doped ZrP_2O_7 has been modeled as the sum of two activated conductivities, presumably from the bulk and internal surfaces (see Fig. 5b). The pre-exponential (σ_{0,H^+}) and effective activation enthalpy (ΔH_{H^+}) of the bulk proton conductivity and the corresponding parameters for surface conductivity from the fitting of the ramps are listed in Table II.

The conductivity was measured in reducing atmospheres at 500–800°C. Figure 6 shows the temperature dependence of the conductivity for the Y-doped material in the H_2O- and D_2O-wetted H_2 + Ar atmospheres. $p(H_2)$ was as low as 6.3×10^{-4} atm so that the H_2O or D_2O (both at ~0.025 atm) effectively determined the isotope content of the mixture. Both curves are obtained after equilibration at 800°C and were recorded during cooling ramps of 18°C/h. The conductivity of the material in the H_2O-wetted atmosphere was higher than that in the D_2O-wetted atmosphere, showing that the material mainly conducts protons also in reducing atmospheres. The proton conductivity in this material was lower than in TiP_2O_7,[21] and the n-type electronic conductivity in TiP_2O_7 is absent in ZrP_2O_7, which is attributable to the less reducible Zr^{4+} cation.

Impedance spectroscopy in the frequency range of 5–10^6 Hz was performed at selected temperatures. The typical impedance spectra of 2 mol % Sc- and Y-doped ZrP_2O_7 at 600°C are shown in Fig. 7a and b. We observed only one semicircle over the range of frequencies and temperatures investigated and deconvoluted the plots to obtain the parameters for an element with a resistor R and a constant phase element Q in parallel (RQ). From this, the character-

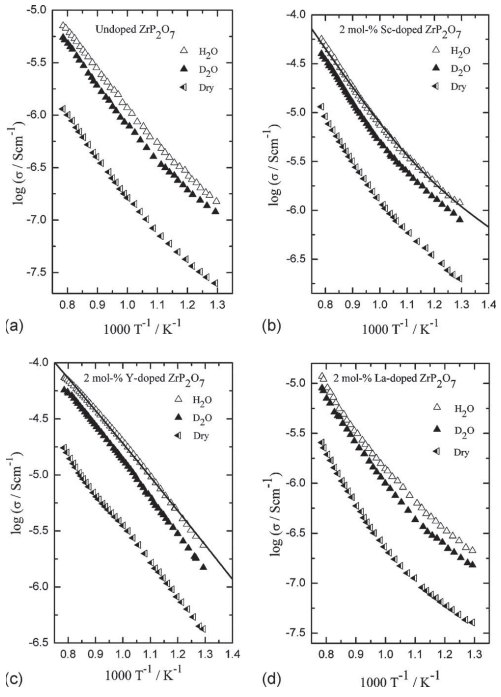

Figure 5. Log ac conductivity vs $1/T$ for (a) ZrP_2O_7, (b) 2 mol % Y-doped, (c) 2 mol % Sc-doped, and (d) 2 mol % La-doped ZrP_2O_7 in wet, D_2O-containing and dry oxygen. The solid lines are modeled behaviors.

istic specific capacitance C was calculated with the equation $C = Y^{1/n}R^{(1/n)-1}$ (Y and n are the parameters defining Q) and came out around 3×10^{-11} F/cm. This indicates that the ac conductivity at 10 kHz mainly reflects the bulk (possibly with a grain boundary parallel contribution) but is not limited by the series grain boundary resistance or electrode responses.

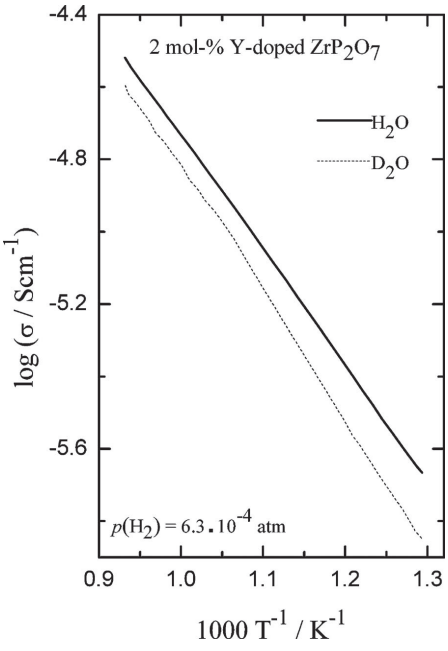

Figure 6. Log ac conductivity vs $1/T$ for 2 mol % Y-doped ZrP_2O_7 in H_2O- and D_2O-wetted H_2 + Ar atmospheres.

The oxygen partial pressure dependencies of the undoped and 2 mol % Sc- and Y-doped materials at constant water vapor pressure at selected temperatures are shown in Fig. 8a-c. The conductivities were independent from $p(O_2)$ under oxidizing as well as reducing atmospheres at each temperature, confirming that there is no electronic contribution to the total conductivity. Protonic conduction dominates and the defect situation appears to be the same in both oxidizing and reducing wet atmospheres.

The water vapor partial pressure dependency of the conductivity

Table I. Activation energies of proton and deuteron conduction, the ratios of the conductivities $\sigma(H_2O)/\sigma(D_2O)$ and the isotope ratio of pre-exponentials A_H/A_D.

Samples	Activation energy (600–900°C) (kJ/mol)		Isotope effect $\sigma H_2O/\sigma D_2O$ (500–1000°C)	Isotope ratio of pre-exponentials A_H/A_D (600–900°C)
	H_2O	D_2O		
Undoped ZrP_2O_7	77	79	1.23–1.27	0.95
Sc-doped ZrP_2O_7	75	79	1.29–1.47	0.94
Y-doped ZrP_2O_7	68	72	1.30–1.58	0.99
La-doped ZrP_2O_7	76	80	1.28–1.50	0.98

Table II. Pre-exponentials and activation enthalpies for bulk proton conductivity and apparent surface conductivity extracted from modeling of temperature ramps in the range 500–1000°C.

Sample	Bulk conductivity		Apparent surface conductivity	
	Pre-exponential (σ_{0,H^+}) (S K/cm)	Activation enthalpy (ΔH_{H^+}) (kJ/mol)	Pre-exponential (S K/cm)	Activation enthalpy (kJ/mol)
Sc-doped ZrP_2O_7	680 ± 300	86 ± 4	1 ± 0.5	38 ± 3
Y-doped ZrP_2O_7	180 ± 20	65 ± 2	—	—

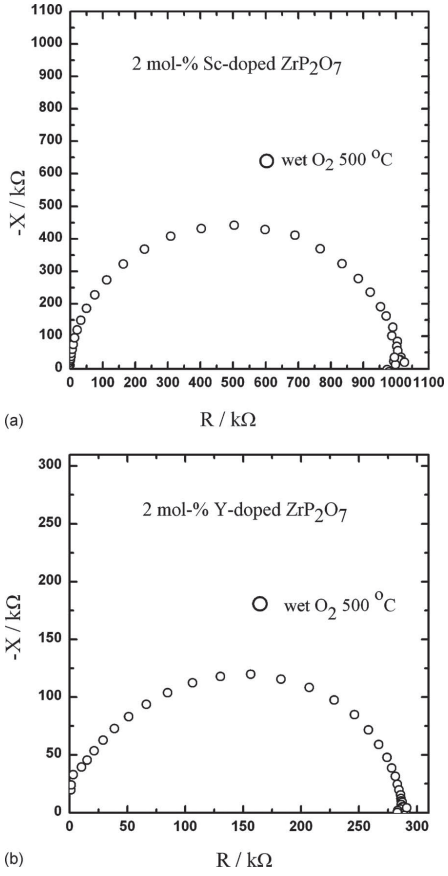

Figure 7. Impedance spectra of (a) 2 mol % Sc-doped and (b) 2 mol % Y-doped ZrP_2O_7 at 500°C (frequency range 5–10^6 Hz).

of the undoped and 2 mol % Sc- and Y-doped materials at constant oxygen partial pressure (1 atm) in the temperature range 500–900°C are shown in Fig. 9a-c. The conductivity increases with increasing water vapor pressure in accordance with the preceding observations and was approximately proportional to $p(H_2O)^{1/3}$ at 500–900°C. The curves for the undoped ZrP_2O_7 and Sc- and Y-doped ZrP_2O_7 have been modeled at each temperature assuming that protons are charge-compensated by oxygen interstitials; the fitted curves are included in Fig. 9a-c. The temperature dependencies of the fitted curves have been modeled according to Eq. 7, and the extracted pre-exponentials and activation enthalpies are listed in Table III. They are in accordance with those from the ramps (Table II) and the enthalpy similar to that of TiP_2O_7.[21]

The pre-exponentials of the proton conductivity obtained by the different evaluations of the data and for different samples vary considerably, are uncertain, and are correlated with the activation enthalpies, as is normal when fitting Arrhenius plots over relatively small temperature ranges. We cannot comment or interpret them beyond this.

The enthalpies of conduction, averaging around 75 kJ/mol, contain the enthalpy of mobility and 1/3 of the enthalpy of the hydration reaction (Eq. 7). The latter is bound to be negative for the reaction to be significant because the corresponding entropy must be negative due to the loss of one water molecule (Eq. 1 and 2). Thus, the activation enthalpy of proton mobility of ZrP_2O_7 must be considerably larger than 75 kJ/mol and thus one reason for the modest proton conductivity.

The conductivity appears to increase somewhat by acceptor doping; however, there is no difference in the water vapor dependency of the undoped and doped materials, suggesting that the doping plays no role in the defect structure. Hence, the differences in conductivity are more likely due to the differences in microstructure of the materials as a result of the different sintering methods and sintering properties of the differently doped samples.

The bulk proton conductivity of ZrP_2O_7 is not sufficient to be of interest in electrolytes for high drain applications such as fuel cells. However, it may be of interest in sensors, both as electrolyte, and in resistance sensors due to the stable $p(H_2O)^{1/3}$ dependency over large ranges of temperature and $p(H_2O)$.

We have not directly shown the identity of the apparent surface conduction, but the differences in H_2O- and D_2O-wetted and dry atmospheres suggest that this is also protonic. It is, moreover, possible that it is related to the abnormally high conductivity reported in insufficiently sintered pyrophosphates at lower temperatures, as mentioned in the introduction and that they reflect conduction in a hygroscopic and amorphous acidic phosphorous-rich phase in the surface.

Transport number measurements.— Transport number measurements were done on the least porous sample (2 mol % Y-doped, SPS) at 700°C in wet oxygen to determine qualitatively the transport number of protons and other ions. Figure 10 shows the transport numbers plotted against the magnitude of the $p(H_2O)$ gradient (as the logarithm of the ratio of the pressures). The measured transport

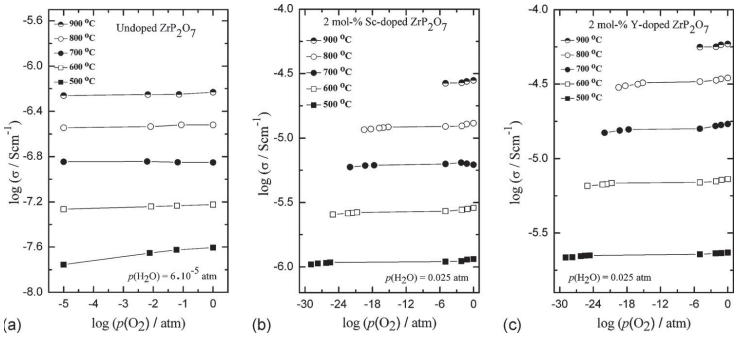

Figure 8. Conductivity vs $p(O_2)$ for (a) ZrP_2O_7 in dry atmospheres and (b) 2 mol % Sc-doped and (c) 2 mol % Y-doped ZrP_2O_7 in wet atmospheres.

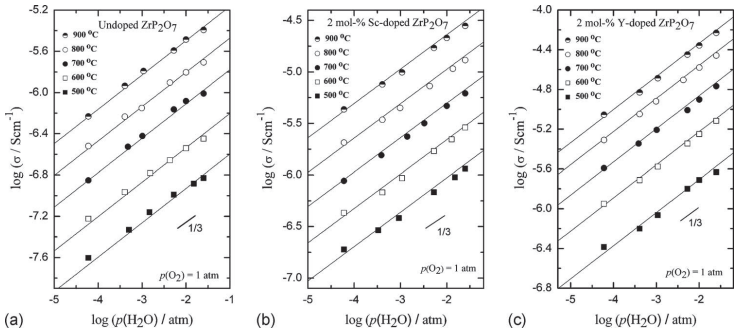

Figure 9. Conductivity vs $p(H_2O)$ for (a) ZrP_2O_7, (b) 2 mol % Sc-doped, and (c) 2 mol % Y-doped ZrP_2O_7 in oxygen. The solid lines are the modeled behavior.

number of protons decreases with increasing gradients. This we attribute to the smaller average $p(H_2O)$ and thus smaller proton conduction with increasing gradient and to larger leakage through unavoidable remaining sample porosity and imperfect gasket sealing.

Table III. Pre-exponentials and activation enthalpies extracted from the modeling of the $p(H_2O)$ dependency of conductivity isotherms in the range 600–900°C.

Sample	Pre-exponential (σ_{0,H^+}) (S K/cm)	Activation enthalpy (ΔH_{H^+}) (kJ/mol)
Undoped ZrP_2O_7	40 ± 5	79 ± 2
Sc-doped ZrP_2O_7	260 ± 120	82 ± 5
Y-doped ZrP_2O_7	217 ± 32	67 ± 1

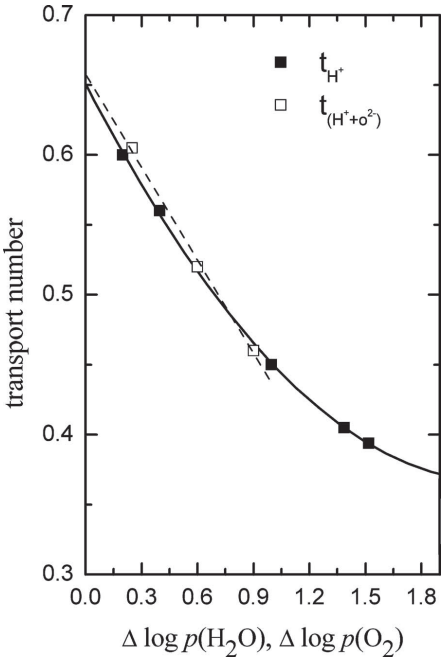

Figure 10. Transport numbers vs $\Delta\log\ p(H_2O)$ and $\Delta\log\ p(O_2)$ of 2 mol % Y-doped ZrP_2O_7 at 700°C in wet oxidizing atmospheres.

The apparent proton transport number in the wet atmosphere was obtained by extrapolation back to zero gradient and comes out as 0.65, indicating that the material is mainly a proton conductor under these conditions. We also measured the emf of a cell exposed to a gradient in $p(O_2)$ at constant $p(H_2O) = 0.025$ atm. The transport number obtained from this measurement is the total ionic transport number (for protons plus native cations and anions). The result gave a transport number of 0.66, which is not significantly different from the measured protonic one, suggesting that native ionic conductivity is minor.

The interpretation of the total conductivity measurements suggested a proton transport number at 700°C in wet oxygen of close to unity. The difference between this and the obtained ionic, i.e., protonic, transport number of around 0.65 is typical of the abovementioned effect of leakages in this relatively high porosity (86% dense sample) and in imperfect sealing between the gas chambers, reducing the effective gradient. The emf measurements thus qualitatively confirm that the sample is mainly a proton conductor in wet atmospheres, and the overall results suggest that this also holds for the bulk conductivity of the other ZrP_2O_7 samples and over a larger temperature range in this study.

Conclusions

The high temperature conductivity of ZrP_2O_7 and the 2 mol % acceptor (Sc, Y, and La) doped ZrP_2O_7 has been investigated. The water vapor pressure dependency, H/D isotope effect, and protonic transport number show that the materials are essentially pure proton conductors, that a free proton hopping diffusion mechanism dominates, and that most likely the defect structure comprises protons and oxide ion interstitials as the dominating defects. The acceptor doping appears not to be significant for the defect structure. The absence of an oxygen partial pressure dependency of the conductivity indicated that no electronic conductivity contributes significantly to the total conductivity. The isobaric temperature dependencies as well as the isothermal $p(H_2O)$ dependencies have all been modeled according to the above, and parameters for the pre-exponentials and activation enthalpies of the bulk and surface conductivities have been extracted. A conductivity contribution with lower activation enthalpy became significant at the lower temperatures in the most porous, traditionally sintered samples. This was absent in the denser spark plasma sintered sample, and we attribute the conductivity contribution at low temperatures to the conduction along internal surfaces of the open porosity. This may well be related to the anomalously high conductivity at lower temperatures reported for poorly sintered samples of this and similar pyrophosphates of tetravalent cations.

Acknowledgments

This work was supported by the FUNMAT@UiO program of the University of Oslo (UiO). The authors are grateful to Dr. Laurent Jantsky, UiO for the assistance with the PXRD work and data interpretation.

University of Oslo assisted in meeting the publication costs of this article.

References

1. H. Iwahara, T. Esaka, H. Uchida, and N. Maeda, *Solid State Ionics*, **3–4**, 359 (1981).
2. T. Norby and P. Kofstad, *J. Am. Ceram. Soc.*, **67**, 786 (1984).
3. W. K. Lee, A. S. Nowick, and L. A. Boatner, *Solid State Ionics*, **18–19**, 989 (1986).
4. H. Iwahara, H. Uchida, K. Ono, and K. Ogaki, *J. Electrochem. Soc.*, **135**, 529 (1988).
5. T. Norby and Y. Larring, *Curr. Opin. Solid State Mater. Sci.*, **2**, 593 (1997).
6. K. D. Kreuer, *Solid State Ionics*, **125**, 285 (1999).
7. S. M. Haile, D. A. Boysen, C. R. I. Chisholm, and R. B. Merle, *Nature (London)*, **410**, 910 (2001).
8. T. Norby, M. Friesel, and B. E. Mellander, *Solid State Ionics*, **77**, 105 (1995).
9. A. Pawlowski and M. Polomska, *Solid State Ionics*, **176**, 2045 (2005).
10. J. Otomo, N. Minagawa, C. Wen, K. Eguchi, and H. Takahashi, *Solid State Ionics*, **156**, 357 (2003).
11. M. Nagao, T. Kamiya, P. Heo, A. Tomita, T. Hibino, and M. Sano, *J. Electrochem. Soc.*, **153**, A1604 (2006).
12. M. Nagao, A. Takeuchi, P. Heo, T. Hibino, M. Sano, and A. Tomita, *Electrochem. Solid-State Lett.*, **9**, A105 (2006).
13. A. Tomita, N. Kajiyama, T. Kamiya, M. Nagao, and T. Hibino, *J. Electrochem. Soc.*, **154**, B1265 (2007).
14. X. Sun, S. Wang, Z. Wang, X. Ye, T. Wen, and F. Huang, *Solid State Ionics*, **179**, 1138 (2008).
15. Y. Li, T. Kunitake, Y. Aoki, and E. Muto, *Adv. Mater.*, **20**, 2398 (2008).
16. G. Alberti, M. Casciola, F. Marmottini, and R. Vivani, *J. Porous Mater.*, **6**, 299 (1999).
17. G. Alberti, M. Casciola, S. Cavalaglio, and R. Vivani, *Solid State Ionics*, **125**, 91 (1999).
18. T. Shirai, S. Satou, Y. Saito, M. Saito, J. Kuwano, and H. Shiroishi, *Phosphorus Res. Bull.*, **21**, 31 (2007).
19. T. Shirai, S. Satou, M. Saito, J. Kuwano, and H. Shiroishi, *Solid State Ionics*, **180**, 569 (2009).
20. S. Tao, *Solid State Ionics*, **180**, 148 (2009).
21. V. Nalini, R. Haugsrud, and T. Norby, *Solid State Ionics*, **181**, 510 (2010).
22. I. C. Marcu, I. Sandulescu, and J.-M. M. Millet, *Appl. Catal., A*, **227**, 309 (2002).
23. B. A. Boukamp, EQUIVCRT Version 3.97, University of Twente (1989).
24. J. Mizusaki, S. Tsuchiya, K. Waragai, H. Tagawa, Y. Arai, and Y. Kuwayama, *J. Am. Ceram. Soc.*, **79**, 109 (1996).
25. T. Norby, *Solid State Ionics*, **28–30**, 1586 (1988).
26. D. P. Sutija, T. Norby, and P. Björnbom, *Solid State Ionics*, **77**, 167 (1995).
27. N. Khosrovani, V. Korthuis, A. W. Sleight, and T. Vogt, *Inorg. Chem.*, **35**, 485 (1996).
28. R. L. Withers, Y. Tabira, J. S. O. Evans, I. J. King, and A. W. Sleight, *J. Solid State Chem.*, **157**, 186 (2001).
29. R. C. Weast (ed.), *Handbook of Chemistry and Physics*, 69th ed., p. F-164, CRC Press, FL (1989).
30. T. Norby and N. Christiansen, *Solid State Ionics*, **77**, 240 (1995).
31. K. Amezawa, H. Maekawa, Y. Tomii, and N. Yamamoto, *Solid State Ionics*, **145**, 233 (2001).
32. K. Amezawa, Y. Tomii, and N. Yamamoto, *Solid State Ionics*, **176**, 135 (2005).
33. K. Amezawa, Y. Tomii, and N. Yamamoto, *Solid State Ionics*, **175**, 569 (2004).
34. Y. Du and A.S. Nowick, *Mater. Res. Soc. Symp. Proc.*, **369**, 289 (1995).
35. J. F. Liu and A. S. Nowick, *Solid State Ionics*, **50**, 131 (1992).
36. N. Kitamura, K. Amezawa, Y. Tomii, T. Hanada, N. Yamamoto, T. Omata, and S. Otsuka-Yao-Matsuo, *J. Electrochem. Soc.*, **152**, A658 (2005).

Defects and transport properties of Sr-doped LaP_3O_9

Vajeeston Nalini, Reidar Haugsrud, Truls Norby

Solid State Ionics **181,** 1264 (2010).

III

Structure, water uptake and electrical conductivity of TiP_2O_7

Vajeeston Nalini, Magnus H. Sørby, Koji Amezawa, Reidar Haugsrud, Helmer Fjellvåg, Truls Norby

Submitted to *J. Am. Ceram. Soc*. (2010).

IV

Structure, Water Uptake and Electrical Conductivity of TiP_2O_7

Vajeeston Nalini, [a,*] Magnus H. Sørby, [b] Koji Amezawa, [c] Reidar Haugsrud, [a] Helmer Fjellvåg, [a] and Truls Norby [a]

[a] Department of Chemistry, University of Oslo, Centre for Materials Science and Nanotechnology, FERMiO, Gaustadalleen 21, NO-0349 Oslo, Norway

[b] Institute for Energy Technology, Department of Physics, P.O. Box 40, NO-2027 Kjeller, Norway

[c] Graduate School of Environmental Studies, Tohoku University, 6-6-01 Aramaki-Aoba, Aoba-ku, Sendai 980-8579, Japan

We here report on the structure of TiP_2O_7 and electrical properties of nominally acceptor (Sc, Fe) doped TiP_2O_7 synthesized by an aqueous phosphoric acid route. Structural characterization, including studies of the high temperature phase transition in TiP_2O_7, was done by powder X-ray and neutron diffraction. Ceramic discs were sintered by the spark plasma technique and their conductivities were characterized as a function of $p(O_2)$ and $p(H_2O)$ in the temperature range 500 to 1000 °C by means of AC constant frequency measurements and impedance spectroscopy. As reported earlier, the acceptor doping appears not to influence the defect structure of TiP_2O_7 significantly. Effects of H^+/D^+ isotope shift were utilized to identify proton conduction. The conductivity was independent of $p(O_2)$ at 500–900 °C under oxidizing conditions suggesting predominantly protonic conduction at these temperatures. Under reducing atmosphere n-type conductivity contributed to the total conductivity at the higher temperatures. $p(H_2O)$ dependencies of the conductivities are interpreted in terms of a defect-chemical model involving protons and oxygen interstitials as the dominating defects. The uptake of water was studied by thermogravimetry at high $p(H_2O)$ and the thermodynamics of the hydration reaction was derived. Finally, parameters for the mobility of protons were extracted by combining the conductivity and thermogravimetry data.

[a,*] Contact information: email: nalini.vajeeston@kjemi.uio.no, tel: +47-22840657, fax: +47-22840651

I. Introduction

The fast transport and kinetics of protons, together with the world's increasing need for new, cleaner and more efficient energy conversion process, have put increasing interest in high-temperature solid proton conducting electrolytes for fuel cells, hydrogen pumps, and electrochemical hydrogen sensors. Despite the advantages and research efforts, this class of electrolytes has not yet provided a breakthrough in the commercial use of solid electrolytes, the main reasons being the difficulty of combining chemical and thermal stability with sufficient proton conductivity.

High-temperature ceramic proton conductors are, in general, oxides with oxygen deficiency in the form of oxygen vacancies, where protons upon hydration dissolve as hydroxide defects at the expense of the vacancies. Leading candidate materials comprise acceptor-substituted perovskite oxides.[1-5] A number of oxyacids such as hydrogen sulfates, selenates, phosphates, and arsenates have been investigated as proton conductors.[6-9] However, their temperature range of operation and stability is limited; they are water soluble and mechanically weak. Appreciable proton conductivity has been encountered also in a number of phosphates, such as $LaPO_4$.[10-12]

More recently, tetravalent metal pyrophosphates (MP_2O_7, M = Si, Ge, Sn, Ti, Zr and Ce) – both undoped and nominally acceptor-doped – have been reported to exhibit remarkably high proton conductivity, exceeding even 0.1 S/cm for 10 mol-% In-doped SnP_2O_7 between 150 and 350 ^oC.[13-17] In contrast, we recently reported that the total conductivity in nominally Al-doped TiP_2O_7[18] under wet oxidizing conditions is rather modest, in the order of 10^{-6}–10^{-4} S/cm at 300−1000 ^oC. The conductivity of the Al-doped TiP_2O_7 was only slightly higher than for undoped TiP_2O_7, in contrast to the effects of doping in rare earth phosphates[11,12,19,20] and we derived a defect-chemical model involving protons charge compensated by oxygen interstitials.

With the aim to achieve significant acceptor doping in TiP_2O_7 by substituting Ti^{4+} with M^{3+} cations, we describe the synthesis, characterization, and conductivity of 2 mol-% Sc- and Fe-doped TiP_2O_7 in oxidizing as well as reducing atmospheres. The high temperature phase transition in TiP_2O_7 is, moreover, analyzed by *in-situ* neutron powder diffraction. The water uptake is furthermore, for the first time, determined by thermogravimetry. Based on the conductivity and thermogravimetry, the thermodynamics of hydration as well as the mobility of protons are derived.

II. Experimental

TiP_2O_7 was synthesized by mixing nominal amounts of TiO_2 (nano-powder, 99.9%, Aldrich) and 85 wt.% aqueous H_3PO_4 (99.999%, Aldrich). 2 mol-% Sc- and Fe-doped TiP_2O_7 were prepared by mixing appropriate amounts of TiO_2 and 85 wt.% H_3PO_4 with high purity Sc_2O_3 and Fe_2O_3, respectively. The atomic ratio of the sum of the acceptor (Fe and Sc) and Ti to P was kept as 1:2. The mixing was done at room temperature until a homogeneous slurry was formed and heated at 200 ^oC for 3 h. The powder obtained was ground, dried at 100 ^oC for 24 h, and calcined at 700 ^oC for 3 h. The structure and phase purity were checked by powder X-ray diffraction (PXRD, Siemens D5000 diffractometer using CuKα radiation). The thermal stability of the Sc-doped TiP_2O_7 was tested by annealing at 1100 ^oC for 14 h, followed by PXRD.

Densification of phosphate-based materials by conventional sintering is often difficult because of thermal decomposition at high temperatures, which limits the sintering temperatures and results in relative densities of typically less than 75%. To aid in densification, the doped samples for conductivity studies in this work were sintered by spark plasma sintering (SPS). With 30 MPa at 1150 ^oC for 5 min, the relative densities achieved for the 2 mol-% Sc- and Fe-doped TiP_2O_7 were, respectively, ~95% and ~85%. The sintered samples were crushed and the powders investigated by PXRD and unit cell parameters were obtained from least-squares fitting of all peak positions.

The structure of TiP_2O_7 was studied by neutron powder diffraction (NPD) using the PUS instrument at the JEEP II reactor (Institute for Energy Technology (IFE), Kjeller, Norway), at ambient temperature and 800 ^oC. Neutrons with $\lambda = 1.5554$ Å were provided by a focussing Ge (511) monochromator. Data was collected in the range $2\theta = 10-130$ ^{o} ($\Delta 2\theta = 0.05$ ^{o}) by 2 detector banks each with 7 vertically stacked position sensitive detectors. The sample was contained in a quartz tube with 8 mm inner diameter, fitted into a furnace with tantalum heating elements. Rietveld refinement was performed using the program GSAS.[21,22] The Bragg peaks were modeled with a Thompson-Cox-Hastings pseudo-Voigt function with three refined parameters. The background was fitted with a 30-term Chebyshev polynomial. The 2θ ranges 37.5−39.8 ^{o}, 43.5−44.1 ^{o} and 69.4−70.1 ^{o} were excluded from the data analyses as they contained Bragg peaks from the tantalum heating elements.

The microstructure and porosity of the samples were analyzed by scanning electron microscopy (SEM; FEI Quanta 200F) and energy dispersive X-ray spectrometry (EDS; EDAX Pegasus 2200 Micro-characterization system). Fig. 1 shows SEM micrographs of 2 mol-% Sc- and Fe-doped TiP_2O_7 after sintering. The porosity of the materials was approximately 5 and 15% by volume for the Sc- and Fe-doped samples, respectively. No secondary phase was observed in either sample. EDS analyses confirmed within the uncertainty of the method that (Ti+Sc):P and (Ti+Fe):P ratios were 1:2.

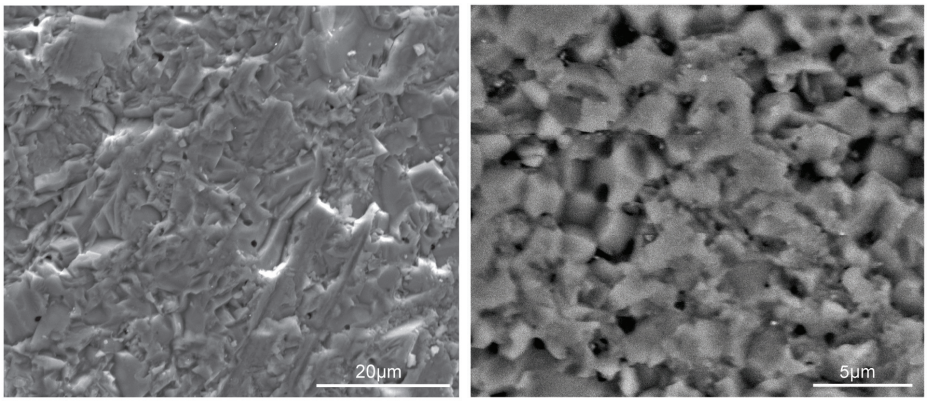

(a) (b)

Fig.1. SEM images of (a) 2 mol-% Sc-doped (back-scatter electron image) and (b) 2 mol-% Fe-doped TiP_2O_7 (mixture of back-scatter electron and secondary electron image) after spark plasma sintering.

For conductivity measurements under oxidizing conditions, circular platinum electrodes of diameter 1 cm were attached to each side of the sintered specimen by painting three layers with platinum ink (Metalor, Pt A3788A). The specimens with electrodes were annealed at 900 ^oC for 2 h to remove residual organics from the ink. Au electrodes (Engelhard, T-10112-gold paste) were used instead of Pt for measurements under reducing conditions by following the same procedure, but with only for 1 h annealing to avoid too much coarsening of the electrode microstructure. The electrical characterization was performed in a ProboStat^{TM} measurement cell (NorECs AS, Norway) with two-point electrode setup, using a Hewlett Packard 4192A impedance analyzer at a frequency 10 kHz and an oscillation voltage of 1.1 V (rms). Impedance spectroscopy was performed at different temperatures in the frequency range $5-10^6$ Hz, to establish the contribution of bulk, grain boundaries and electrode resistance. The electrical conductivity was measured

over the temperature range 500−1000 °C as a function of oxygen and water vapor partial pressures under oxidizing and reducing conditions. The various partial pressures were established by using pure O_2, Ar/O_2 and Ar/H_2 gas mixtures for oxygen pressure dependences, and different water vapor partial pressure was obtained by mixing gas dried over P_2O_5 ($pH_2O = 3 \cdot 10^{-5}$ atm) with gas wetted by bubbling through pure water and then a saturated solution of $KBr_{(aq)}$ at room temperature ($pH_2O = 0.025$ atm). To investigate the contribution from protons, the conductivity was measured similarly under D_2O-wetted atmospheres. Thermogravimetric analysis (TGA) was carried out in a Netzsch STA 449 C Jupiter instrument on Fe-doped TiP_2O_7 with alumina sample and reference containers. The sample, consisting of 160 milligrams of powder, was first heated to 900 °C at 1.5 °C/min in a stream of bottle-dry N_2 gas. It was then equilibrated in N_2 with 0.1 atm H_2O and then cooled at the same rate. All gas flow rates were 50 ml/min. A corresponding correction file was recorded with empty crucibles. The water content in the sample was obtained from the difference between the sample and correction files, using the dry-to-wet step at 900 °C as a starting point, assuming the water content in dry atmospheres at 900 °C is zero.

III. Results and discussion

(1) Structural characterization

Fig. 2 shows the PXRD patterns for undoped and 2 mol-% Sc- and Fe-doped TiP_2O_7 after sintering. They match those from the study by Norberg *et al.*[23], confirming that pure, single-phase materials were obtained after sintering. The compounds exhibited a cubic superstructure (space group: $Pa\bar{3}$; space group no. 205) with lattice parameter $a = 23.533(1)$ Å for undoped TiP_2O_7[18], in good agreement with the value of $a = 23.5340$ of Norberg *et al.*[23] The lattice parameters for 2 mol-% Sc- and Fe-doped TiP_2O_7 were 23.596(3) and 23.528(1) Å, respectively. The ionic radii with coordination number 6 of Ti^{4+}, Sc^{3+} and Fe^{3+} ions are 0.68, 0.732 and 0.64 Å respectively,[24] and in accordance with this, the lattice parameters for the Sc- and Fe-doped TiP_2O_7 were larger and smaller, respectively, than for the undoped material. PXRD patterns for 2 mol-% Sc-doped TiP_2O_7 after heat-treatments at 1100 °C for 3, 7 and 14 h are given in Fig. 3. After 7 h, diffraction peaks assigned to the orthorhombic $Ti_2O(PO_4)_2$ and P_2O_5 were observed in addition to peaks of TiP_2O_7. With increasing time, the intensity of the peaks corresponding to these secondary phases increases. This suggests that TiP_2O_7 decomposes into $Ti_2O(PO_4)_2$ and

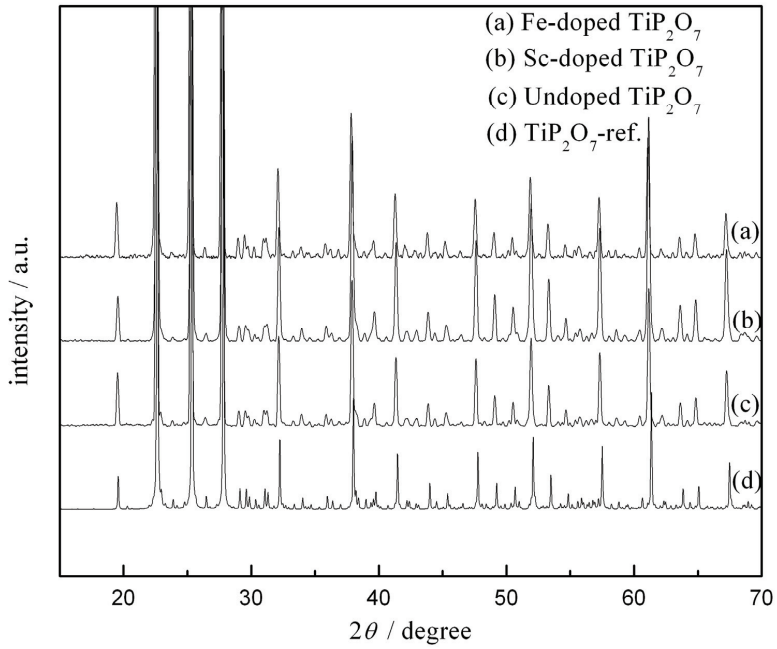

Fig.2. Observed PXRD patterns of (a) 2 mol-% Fe-doped (b) 2 mol-% Sc-doped (c) undoped TiP_2O_7 after spark plasma sintering and (d) TiP_2O_7 from Ref.[23]

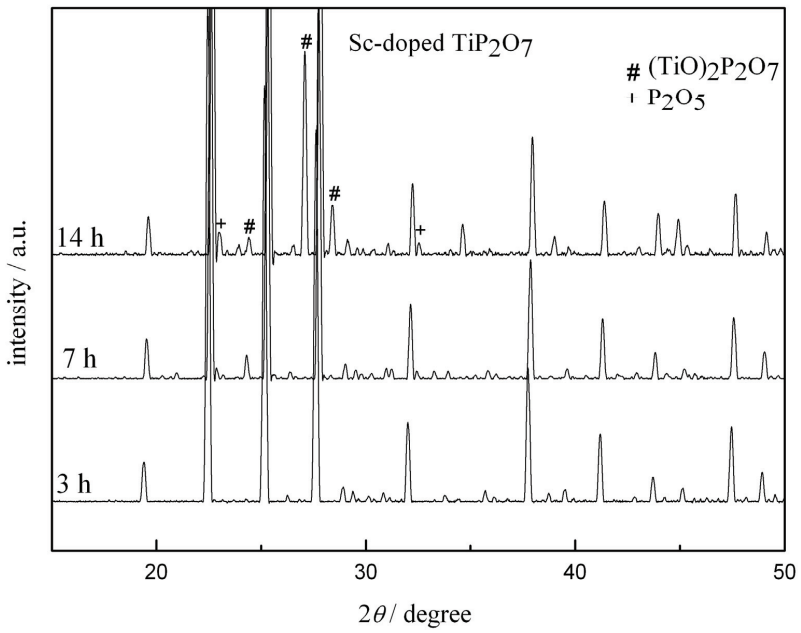

Fig.3. PXRD patterns for 2 mol-% Sc-doped TiP_2O_7 after heat-treatments at 1100 ^oC for 3, 7, and 14 h.

P_2O_5 at 1100 ^oC, as reported earlier.[25,18]

Chernorukov *et al*.[26] reported that TiP_2O_7 is cubic, but with two different modifications; at low temperature the α-phase with a unit cell parameter a = 23.52 Å that transforms into the β modification at 730 ^oC with a = 7.80 Å. As will be shown below, this phase transition was observed by conductivity measurements at 670 and 680 ^oC, respectively, for the Sc- and Fe-doped samples. The difference in temperature is likely due to hysteresis, direction of temperature change, and method of determination (heating in Chernorukov et al.'s structural work as compared to cooling in our conductivity measurements) rather than doping.

For the Rietveld refinement of the room and high temperature NPD data, the structure model reported by Norberg *et al*.[23] (space group $Pa\bar{3}$, a = 23.5340 Å) was taken as the starting point. The model contains 50 crystallographically different atoms defined by 134 positional parameters. A good fit (R_{wp} = 3.18%) was obtained without refining the atomic positions, thus confirming that the atomic arrangement of obtained TiP_2O_7 phase corresponds fully to that described in the single crystal study by Norberg *et al*.[23]

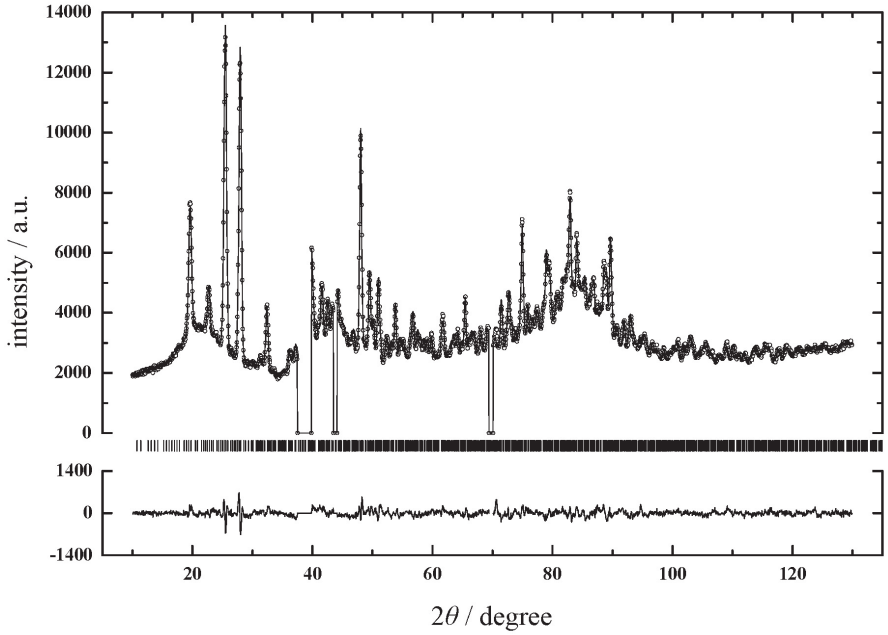

Fig.4. Rietveld fit to ambient temperature NPD data for TiP_2O_7 at ambient temperature using the structure model reported by Norberg *et al*.[23] with isotropic temperature factors. λ = 1.5554 Å, R_{wp} = 2.70 (background subtracted). Three regions are excluded from the refinement due to peaks from the furnace.

The data allowed just refinement of isotropic thermal parameters (one for each element) rather than the anisotropic description included in Norberg's single crystal study. The Rietveld fit to the NPD data for TiP_2O_7 at ambient temperature is shown in Fig. 4. The NPD data acquired at 800 ^oC show the same main features as the room temperature data, but many of the weak reflections observed at room temperature are absent. This indicates a symmetry increase and/or a smaller unit cell. A search among the crystal structures for cubic MP_2O_7 phases reveals several isostructural pyrophosphates, e.g. a high-temperature modification of ZrP_2O_7, with space group $Pa\bar{3}$ and unit cell axis about 1/3 of that found for TiP_2O_7 at ambient temperature, which corresponds to the unit cell parameter for the high-temperature phase suggested by Chernorukov *et al.*[26] The observed peaks at 800 ^oC are consistent with such a subcell (a = 7.96 Å). The coordinates for the high temperature

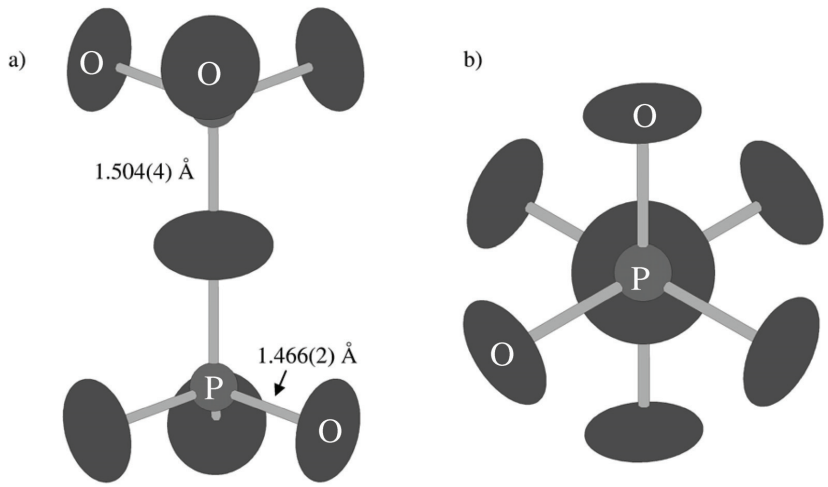

Fig.5. The pyrophosphate group at 800 ^oC viewed a) perpendicular to and b) along the P-O-P bond. The ellipsoids represent anisotropic thermal displacements according to the Rietveld refinement.

crystal structure of ZrP_2O_7 was taken as starting point for the Rietveld refinement. This structure is much simpler than the room temperature structure, with only four positional parameters for four crystallographically different atoms (Zr in *4a*, P in *8c*, O1 in *24d* and O2 in *4b*). The atomic positions were refined along with isotropic displacement factors yielding a fit with significant intensity problems. Refinement of anisotropic temperature factors greatly improved the fit. The displacements of Ti and P turned out nearly isotropic,

whereas those for O appear to be highly anisotropic and occur mostly perpendicular to the P-O bonds (Fig. 5). The fit to the experimental data are shown in Fig. 6 and the structural details are given in Table I and II. The PO_4 tetrahedra are close to ideal with O-P-O angles 107.2(2) ^{o} and 111.6(2) ^{o} (as compared to 109.5 ^{o} for an ideal tetrahedron). Three of the P-O distances are 1.466(2) Å while the third (involving the shared O-atom) is 1.504(2) Å. The tetrahedra are more regular than in the room temperature superstructure where the O-P-O angles are in the range from 104.2 ^{o} to 113.6 ^{o}. Thus, NPD results confirm that TiP_2O_7 undergoes a phase transformation at high temperature similar to Zr and Sn pyrophosphates. At low temperature, the material exists as a cubic superstructure with a unit cell parameter of 23.533(1) Å that upon arrival at 800 ^{o}C has transformed into a closely related high temperature modification with a smaller unit cell of 7.9641(3) Å.

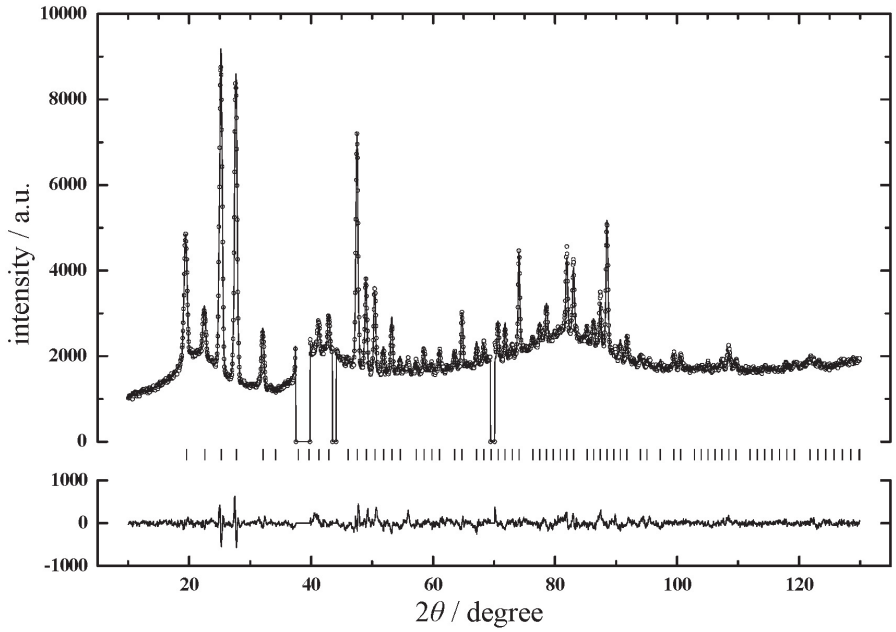

Fig.6. Rietveld fit to NPD data for TiP_2O_7 at 800 ^{o}C using the high temperature structure for ZrP_2O_7 as starting point. λ = 1.5554 Å, R_{wp} = 4.75 (background subtracted). Three regions are excluded from the refinement due to peaks from the furnace.

Table I. Result of Rietveld refinement of TiP_2O_7 at 800 °C with NPD data. Space group $Pa\bar{3}$. a = 7.9641(3) Å. Standard deviations are given in parenthesis. The refinement was performed with anisotropic temperature factors (see Table II). The equivalent isotropic displacement factors are given.

Atom	Site	*x*	*y*	*z*	$U_{iso,\ equivalent}$ (10^{-2} Å^2)
Ti	*4a*	0.000000	0.000000	0.000000	3.0
P	*8c*	0.3911(3)	0.3911(3)	0.3911(3)	2.8
O1	*24d*	0.4436(3)	0.2168(3)	0.4184(4)	9.1
O2	*4b*	0.500000	0.500000	0.500000	13.0

Table II. Anisotropic temperature factors from Rietveld refinement of TiP_2O_7 at 800 °C with NPD data. The unit is 10^{-2} Å^2. (Negative values for coefficients in anisotropic temperature factors are acceptable; the resulting ellipsoids (Fig. 5) are realistic.)

Name	U11	U22	U33	U12	U13	U23
Ti	2.98(18)	2.98(18)	2.98(18)	0.26(25)	0.26(25)	0.26(25)
P	2.75(8)	2.75(8)	2.75(8)	0.03(11)	0.03(11)	0.03(11)
O1	10.63(24)	4.27(15)	12.30(28)	3.40(14)	0.25(20)	1.90(15)
O2	13.02(32)	13.02(32)	13.02(32)	−3.73(37)	−3.73(37)	−3.73(37)

(2) Conductivity measurements

Fig. 7 shows the temperature dependence of the conductivity in wet, D_2O-wetted, and dry oxygen atmospheres for Sc- and Fe-doped TiP_2O_7. The data for the Fe-doped sample also includes reducing atmospheres (H_2O- and D_2O-wetted H_2+Ar atmospheres). The hydrogen concentration was small ($p(H_2)$ = $8.1 \cdot 10^{-3}$ atm) so that the isotope content is largely determined by the content of water (H_2O or D_2O). The conductivity of the materials in wet atmosphere is significantly higher than in dry and in D_2O-wetted atmospheres. The Sc- and Fe-doped samples exhibit a higher conductivity than the undoped TiP_2O_7, but as we shall see this is probably only a result of the higher density of the doped samples prepared by SPS as compared with the conventionally sintered undoped sample. The Arrhenius plots show bends at 670 and 680 °C for the Sc- and Fe-doped samples, respectively, attributed to

the aforementioned phase transition. It should be noted however that the phase transition is not observed for the Fe-doped sample in wet hydrogen. The activation energy of the total conductivity of Sc- and Fe-doped TiP_2O_7 in wet oxidizing atmosphere was determined from $\ln(\sigma T)$ vs $1/T$ plots to 0.75 and 0.76 eV, respectively, at 500−680 ^oC, i.e. below the phase transition temperature. Above the phase transition (700−1000 ^oC) the activation energy was evaluated as 0.49 and 0.51 eV, respectively, for the Sc- and Fe-doped samples.

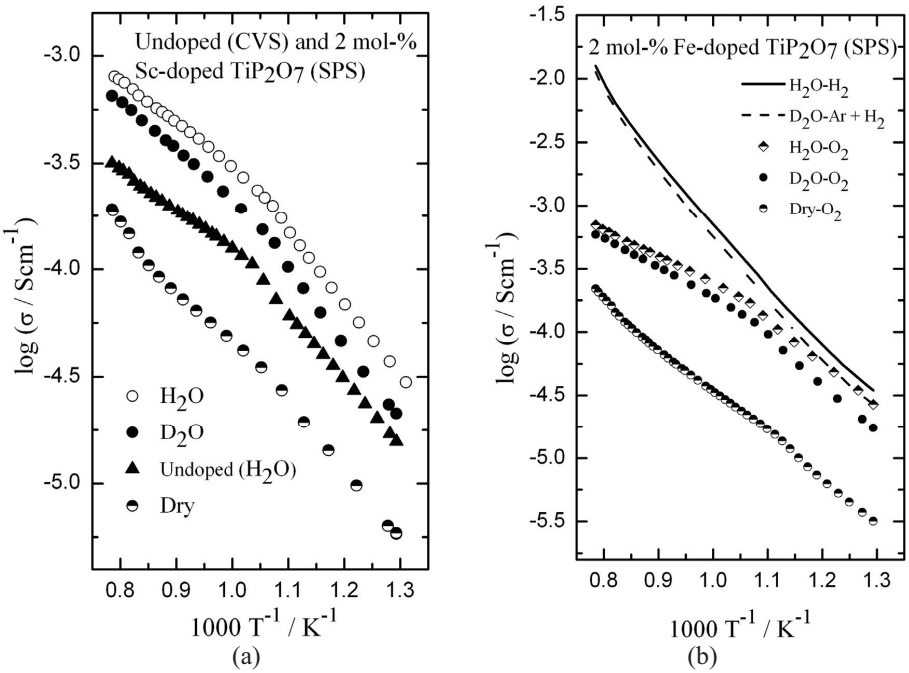

Fig.7. Temperature dependence of the conductivity of (a) conventionally sintered (CVS) undoped (wet) and spark plasma sintered (SPS) 2 mol-% Sc-doped TiP_2O_7 in wet, D_2O-containing, and dry oxygen atmospheres and (b) SPS 2 mol-% Fe-doped TiP_2O_7 in wet, D_2O-containing, dry oxygen and reducing atmospheres (H_2O- and D_2O-wetted H_2+Ar).

The ratios of the conductivities $\sigma(H_2O)/\ \sigma(D_2O)$ were 1.59 and 1.54 at 500 ^oC and 1.27 and 1.20 at 1000 ^oC, for the Sc- and Fe-doped TiP_2O_7, respectively. The conductivity ratios imply that protons are the dominating charge carrier under all conditions, and that the transfer of protons takes place by a free proton Grotthuss-type hopping mechanism.

Impedance sweeps were conducted at selected temperatures in wet and dry oxygen to investigate the bulk and possible grain boundary contributions to the impedance. Selected impedance spectra representative of the Sc- and Fe-doped TiP_2O_7 are displayed in

Fig. 8(a) and (b), respectively, showing in both cases only one semicircle. The spectra were deconvoluted according to one (RQ)-element, and the capacitance C was calculated from the relation $C = Y^{\frac{1}{n}} R^{\frac{1}{n}-1}$ (Y and n denote two constants in the constant phase element Q). The capacitances came out as $1 \cdot 10^{-11}$ and $2 \cdot 10^{-11}$ F cm^{-1}, respectively, for Sc-and Fe-doped samples. This showed that the AC conductivities at 10 kHz mainly reflect bulk properties and not grain boundary or electrode responses.

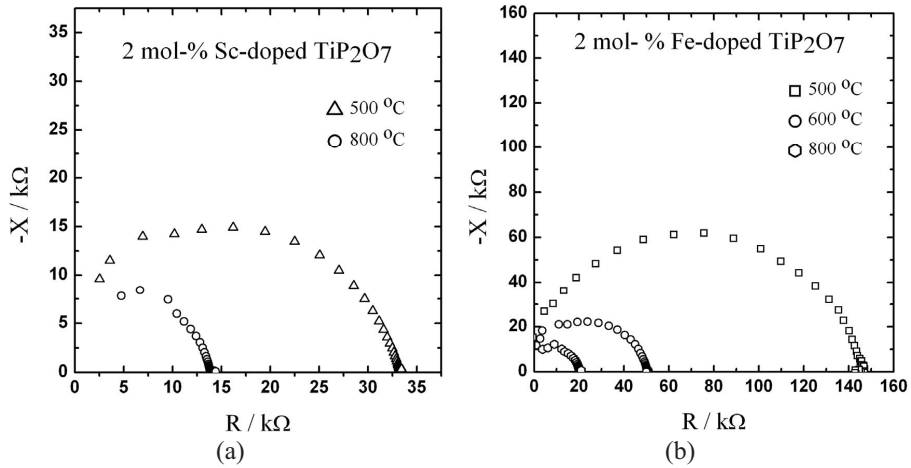

Fig.8. Impedance spectra of (a) 2 mol-% Sc-doped TiP_2O_7 at 500 °C in wet oxygen and at 800 °C in dry oxygen atmospheres and (b) 2 mol-% Fe-doped TiP_2O_7 in dry oxygen atmospheres at 500, 600 and 800 °C ($5-10^6$ Hz).

The conductivity of Fe-doped TiP_2O_7 in wet argon and wet oxygen is presented vs $1/T$ in Fig. 9. Below 900 °C the conductivities were independent of $p(O_2)$, indicating that the electronic contribution was minor. At 900 °C and above the conductivity was higher in Ar than in O_2 and this is attributed to a significant n-type electronic contribution, as reported before.[18] Isothermal $p(O_2)$ dependencies of the conductivity of Sc-doped TiP_2O_7 at constant $p(H_2O)$ (0.025 atm) are shown in Fig. 10. Under reducing conditions, the conductivity increased with decreasing $p(O_2)$ approaching $p(O_2)^{-1/4}$ dependencies at higher temperatures suggesting that n-type electronic conductivity became significant and dominating.

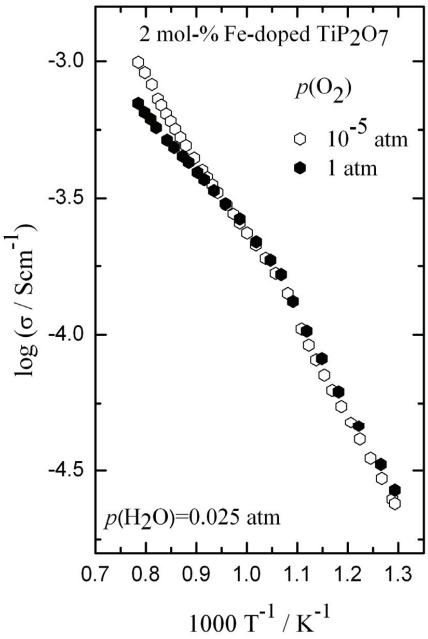

Fig.9. Temperature dependence of the conductivity of 2 mol-% Fe-doped TiP_2O_7 in wet argon and O_2 atmospheres.

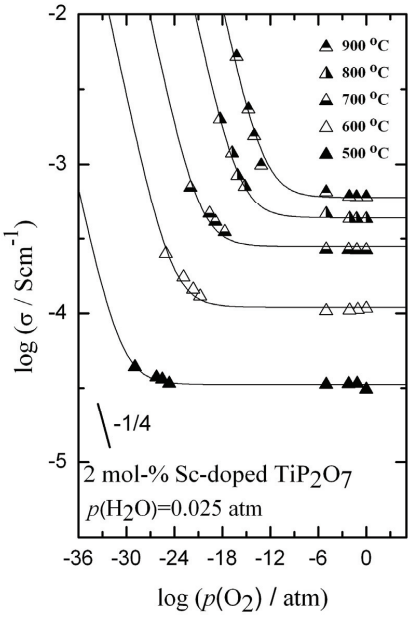

Fig.10. $p(O_2)$ dependence of the conductivity of 2 mol-% Sc-doped TiP_2O_7 in wet atmosphere. The solid lines represent the modeled behavior.

The $p(H_2O)$ dependency of Fe-doped TiP_2O_7 at essentially constant $p(O_2)$ (~1 atm) for selected temperatures are shown in Fig. 11. The conductivity increases with increasing $p(H_2O)$; it was approximately proportional to $p(H_2O)^{1/3}$ at the lower temperatures, while the dependencies decreased with increasing temperatures, earlier attributed to an increasing influence of the n-type electronic contribution.[18]

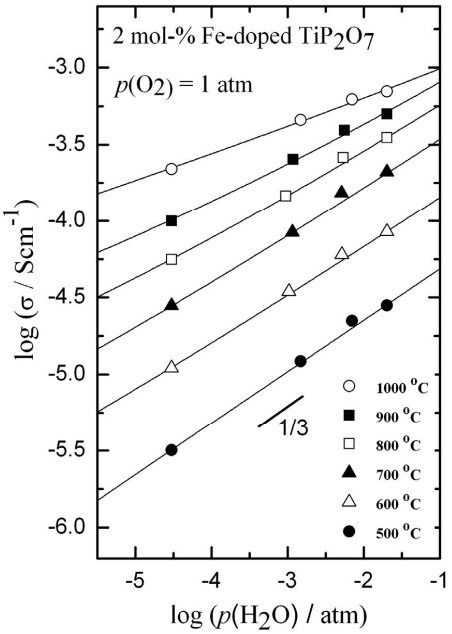

Fig.11. Measured and modeled total conductivity for 2 mol-% Fe-doped TiP_2O_7 as a function of $p(H_2O)$ in oxygen atmosphere. The lines represent the corresponding fitted conductivities.

(3) Defect chemistry

In TiP_2O_7, the pyrophosphate group may be hydrated to form hydrogen pyrophosphate defects at pyrophosphate sites, denoted as $(HP_2O_7)^{\bullet}_{P_2O_7}$. These may charge compensate acceptor dopants or – as proposed earlier[18] - oxygen interstitials formed along with the hydrogen pyrophosphate defect during interaction with surrounding water vapor. Interstitial oxygen may be denoted as phosphate ions at pyrophosphate sites, $(2PO_4)^{//}_{P_2O_7}$, and the hydration can be written as follows:

$$3(P_2O_7)^{x}_{P_2O_7} + H_2O_{(g)} = (2PO_4)^{//}_{P_2O_7} + 2(HP_2O_7)^{\bullet}_{P_2O_7} \quad (1)$$

The equilibrium constant for the above reaction is expressed as

$$K_1 = \frac{\left[(2PO_4)^{//}_{P_2O_7}\right]\left[(HP_2O_7)^{\bullet}_{P_2O_7}\right]^2}{\left[(P_2O_7)^{x}_{P_2O_7}\right]^3 p(H_2O)} = \exp\left(\frac{\Delta S_1^0}{R}\right)\exp\left(\frac{-\Delta H_1^0}{RT}\right) \quad (2)$$

The electroneutrality condition of an acceptor-doped pyrophosphate can in this case be approximated by

$$2\left[(2PO_4)^{//}_{P_2O_7}\right] + \left[A^{/}\right] = \left[(HP_2O_7)^{\bullet}_{P_2O_7}\right] \quad (3)$$

By combining the equilibrium constant (Eq. 2) with the electroneutrality condition (Eq. 3), the following equation for the concentration of protons follows:

$$\left[(HP_2O_7)^{\bullet}_{P_2O_7}\right]^3 - \left[A^{/}\right]\left[(HP_2O_7)^{\bullet}_{P_2O_7}\right]^2 - 2K_1 p(H_2O)\left[(P_2O_7)^{x}_{P_2O_7}\right]^3 = 0 \quad (4)$$

At low $p(H_2O)$, the proton concentration is constant, equal to the dopant concentration, and the protonic conductivity would be independent of $p(H_2O)$. At high $p(H_2O)$, we have $2\left[2(PO_4)^{//}_{P_2O_7}\right] = \left[(HP_2O_7)^{\bullet}_{P_2O_7}\right]$ and under these limiting conditions, the proton concentration will be given by:

$$\left[(HP_2O_7)^{\bullet}_{P_2O_7}\right] = 2^{1/3} K_1^{1/3}\, p(H_2O)^{1/3} = c_{0,H^+}\exp\left(\frac{-\frac{1}{3}\Delta H_1^0}{RT}\right) p(H_2O)^{1/3} \quad (5)$$

where c_{0,H^+} is the pre-exponential of proton concentration and ΔH_1^0 is the standard enthalpy change of the hydration reaction (Eqs. 1 and 2).

Under reducing conditions, one may expect that Ti^{4+} may be reduced forming electrons, for instance charge compensating protons according to

$$2(P_2O_7)^{x}_{P_2O_7} + H_2O_{(g)} = 2(HP_2O_7)^{\bullet}_{P_2O_7} + 2e^{/} + \tfrac{1}{2}O_2 \quad (6)$$

In addition, Fe^{3+} dopants may also be reduced to Fe^{2+}, but occupation at the small Ti^{4+} site probably suppresses this tendency, and we neglect it in the following, for simplicity. The equilibrium constant of the above reaction can be expressed as

$$K_2 = \frac{\left[(\mathrm{HP_2O_7})^{\bullet}_{\mathrm{P_2O_7}}\right]^2 n^2 p(\mathrm{O_2})^{1/2}}{\left[(\mathrm{P_2O_7})^{\mathrm{x}}_{\mathrm{P_2O_7}}\right]^2 p(\mathrm{H_2O})} = K_{0,2}\exp\left(\frac{-\Delta H_2^0}{RT}\right) \tag{7}$$

where n is the concentration of electrons, and the pre-exponential constant is used instead of a standard entropy change, as the standard state of the concentration of electrons is not straightforward to define. By assuming that electrons are minority defects concentration-wise, we can insert the proton concentration from equation (5) into equation (7) and the concentration of electrons thereby reads:

$$n = \frac{K_2^{1/2} p(\mathrm{H_2O})^{1/6} p(\mathrm{O_2})^{-1/4}}{2^{1/3} K_1^{1/3}} = n_0 \exp\left(\frac{-(\tfrac{1}{2}\Delta H_2^0 - \tfrac{1}{3}\Delta H_1^0)}{RT}\right) p(\mathrm{H_2O})^{1/6} p(\mathrm{O_2})^{-1/4} \tag{8}$$

where n_0 is a pre-exponential of electron concentration.

The partial conductivity of a charge carrier i can be expressed as

$$\sigma_i = z_i F c_i \mu_i = z_i F [i] \delta_M \mu_i \tag{9}$$

where z_i is the number of charges, F the Faraday constant, c_i the concentration (mol-cm^{-3}) and μ_i the charge mobility (cm^2/Vs), and where furthermore $[i]$ is the concentration of charge carriers in mole fraction and δ_M the molar density (mol- cm^{-3}) of the material. For diffusing species (protons, and small polaron electronic carriers) the temperature dependency of the charge mobility μ_i is given as

$$\mu_i = \mu_{0,i} \frac{1}{T} \exp\left(\frac{-\Delta H_{m,i}}{RT}\right) \tag{10}$$

where $\mu_{0,i}$ is the pre-exponential of charge mobility and $\Delta H_{m,i}$ is the migration enthalpy.

In accordance with the ionic radii, the lattice parameter for the Fe-doped TiP_2O_7 (a = 23.528(1) Å) was lower than that of undoped sample (a = 23.533(1) Å). Moreover, the Fe-doped sample exhibited a conductivity a little higher than the undoped sample. However, the differences are small, and the $p(H_2O)$ dependencies of the conductivities are similar. As concluded also for Al-doped TiP_2O_7[18] it thus seems that the defect structure is not altered by acceptor doping. We believe the increased conductivity is related to the microstructure of the material caused by the difference in sintering method. The $p(H_2O)$ dependency of the measured conductivity of the Fe-doped sample has thus been modeled at each temperature assuming the model in which protons charge compensate oxygen interstitials, and a conductivity with contributions from protons and minority electrons, the same as we have applied earlier for Al-doped TiP_2O_7.[18] The conductivity of protons and electrons can in this case be expressed as:

$$\sigma_{H^+} = zFc_{0,H^+}\mu_{0,H^+}pH_2O^{1/3}\frac{1}{T}\exp\left(\frac{-\Delta H_{H^+}}{RT}\right) \tag{11}$$

$$\sigma_n = zFn_0\mu_{0,n}pH_2O^{1/6}pO_2^{-1/4}\frac{1}{T}\exp\left(\frac{-\Delta H_n}{RT}\right) \tag{12}$$

Table III. Pre-exponentials and activation enthalpies of partial proton and electron conductivities extracted from the modeling of the $p(H_2O)$ dependency of the conductivity of the nominally Fe-doped sample.

Temperature	Pre-exponential ($zFc_{0,H^+}\mu_{0,H^+}$) [S K/cm]	Activation enthalpy (ΔH_{H^+}) [kJ/mol]	Pre-exponential ($zFn_{0,n}\mu_{0,n}$) [S K/cm]	Activation enthalpy (ΔH_n) [kJ/mol]
500−700 °C (Cubic α-modification)	$(2 \pm 1) \cdot 10^3$	66 ± 2	-	-
700−900 °C (Cubic β-modification)	62 ± 30	35 ± 5	$10^{8\pm1}$	208 ± 25

The modeled curves are shown in Fig. 11. The temperature dependencies of the resulting curves have been further fitted according to Eqs. 11 and 12, and the extracted pre-exponentials ($zFc_0\mu_0$) and activation enthalpies (ΔH) of partial proton and electron conductivities at low and high temperatures are listed in Table III.

Table IV. Pre-exponentials and activation enthalpies of partial proton and electron conductivities extracted from the modeling of the $p(O_2)$ dependency of the conductivity of the nominally Sc-doped sample.

Temperature	Pre-exponential ($zFc_{0,H^+}\mu_{0,H^+}$) [S K/cm]	Activation enthalpy (ΔH_{H^+}) [kJ/mol]	Pre-exponential ($zFn_{0,n}\mu_{0,n}$) [S K/cm]	Activation enthalpy (ΔH_n) [kJ/mol]
500−700 °C (Cubic α-modification)	$(6 \pm 1) \cdot 10^3$	71 ± 1	$10^{8\pm2}$	247 ± 35
700−900 °C (Cubic β-modification)	253 ± 67	44.5 ± 2.5	$10^{8\pm2}$	258 ± 35

The $p(O_2)$ dependency of the measured conductivity of the nominally Sc-doped sample has been modeled under the same assumptions as above at each temperature as shown in Fig. 10. The pre-exponentials and activation enthalpies of partial proton and electron conductivities are derived and are listed in Table IV. The change in the activation enthalpies of the partial proton conductivity between low and high temperature is due to the phase transformation from the low temperature cubic supercell to the high temperature smaller unit cell. The activation enthalpies and pre-exponentials of partial proton conductivities derived from the $p(H_2O)$ dependency of the nominally Fe-doped sample and the $p(O_2)$ dependency of the nominally Sc-doped sample are in reasonable agreement, both at low and high temperature. The n-type conductivity extracted from the $p(H_2O)$ dependencies of the Fe-doped sample in oxidizing atmospheres is however considerably larger than that obtained from the $p(O_2)$ dependencies of the Sc-doped sample under wet reducing conditions, as reflected in the lower activation energy and larger pre-exponential. The origin of this difference is not clear; while Fe^{3+} as a dopant is more readily reduced

than Sc^{3+}, the effect should be minor as long as the dopants do not seem to dissolve significantly in TiP_2O_7.

(4) Thermogravimetric analysis (TGA)

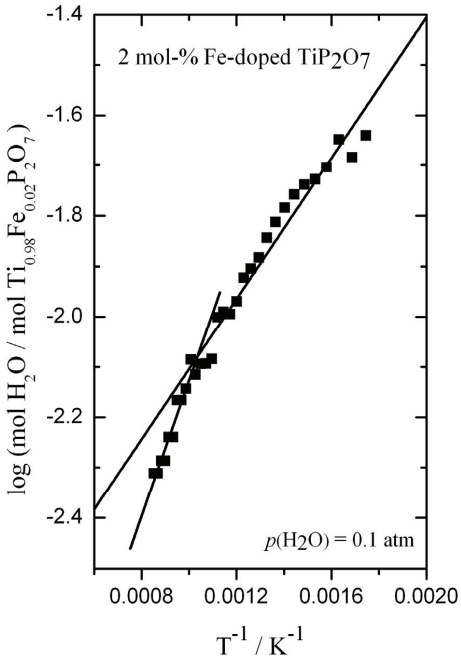

Fig.12. Water content of Fe-doped TiP_2O_7 as a function of inverse temperature in humidified N_2 gas. The solid lines represent the modeled curves.

Fig. 12 shows the results of TGA in terms of water content for the Fe-doped TiP_2O_7 obtained in flowing nitrogen with 10 vol.% water vapor. A continuous gain in water content was encountered during cooling over the whole temperature range. There appears to be a change in behavior at the phase transition, and we thus treat the thermodynamics of hydration differently for the low and high temperature structures. The TGA results are in both cases modeled under the assumption that protons are charge compensated by oxygen interstitials and the derived standard hydration entropy and enthalpy (Eqs. 1 and 2) were, respectively, −147 ± 6 J/mol K and −40 ± 4 kJ/mol at low temperature and −185 ± 13 J/mol K and −77 ± 15 kJ/mol at high temperature. Uncertainties given represent the confidence intervals of the regression in the numeric fit. Hydration entropies are generally reported in the range −160 to −100 J/mol K, reflecting the entropy loss of one gas

molecule for chemical reactions, empirically −120 J/mol K.[27] In this respect, the entropy of hydration at low temperature seems reasonable while at high temperature it is beyond the normal range.

From the TGA curve the proton concentration at 300 °C of 0.04 mol OH^-/mol-TiP_2O_7) is higher than the nominal acceptor concentration (0.02), in agreement with the proposed defect structure. At high temperatures, however, the proton concentration falls below the nominal acceptor concentration. The $p(H_2O)$ dependency of the conductivity of the same material indicated that the protons dissolve in quantities exceeding the effective dopant level also at high temperatures. All in all, this may indicate that the acceptors are not fully and effectively dissolved.

(5) Proton mobility

Now we combine the proton conductivity and thermodynamic parameters from TGA to find the mobility parameters using Eqs. 9 and 10. The derived apparent enthalpy of proton migration $\Delta H_{m,H+}$ is 79 ± 3 kJ/mol at 500−700 °C and 61 ± 5 kJ/mol at 700−1000 °C. The apparent mobility pre-exponential μ_{0,H^+} is 470 ± 150 cm^2 K/V s at low temperatures and 58 ± 30 cm^2 K/V s at higher temperatures. Theoretically, the pre-exponential should approach ~1000 cm^2 K/V s for proton migration, but the effective attempt frequency and sticking probability tend to lower this value to 10−100 cm^2 K/V s.[28] Hence our pre-exponentials of the two modifications are reasonable. The originally measured conductivity leaves no doubt that there is a change in transport properties at the phase transition. If we continue to assume it is at least partly due to mobility, we may speculate that the behavior of the mobility in the low temperature phase reflects a gradual change in the enthalpy or pre-exponential, rather than both a high constant enthalpy and high constant pre-exponential, in a manner similar to that recently reported for $LaNbO_4$ for Fjeld *et al*.[29] The lower mobility may in any case be related to higher packing density or lower symmetry of the low temperature 3 x 3 x 3 supercell structure. More densely packed oxides do in general have lower proton mobility, and in perovskite-related oxides it is found that lower symmetry, e.g. distortions from cubicity, decreases the proton mobility.[30]

The proton conductivity of TiP_2O_7 is modest, e.g. $5 \cdot 10^{-4}$ S/cm at 900 °C in wet atmospheres. Under operation in steam ($p(H_2O)$ = 1 atm) this would increase to around $2 \cdot 10^{-3}$ S/cm, and micron-thick films of TiP_2O_7 could in principle find application as proton

conducting electrolyte. Under reducing atmospheres (wet H_2) the material exhibits dominating electronic conductivity in addition to the protonic, and the ambipolar conductivity ($\sigma_{H^+}\sigma_{e^-}/\sigma_{tot}$) that enables and governs hydrogen permeation would be limited by the proton conductivity levels mentioned. This would suggest that the material is a candidate for hydrogen separation membrane applications, and the ambipolar conductivities and hydrogen permeabilities would be comparable to those of many perovskite oxides.[31] However, phosphates may be unstable over extended time at such high temperatures due to the evaporation of $P_2O_{5(g)}$ under oxidizing conditions or $PH_{3(g)}$ in hydrogen atmospheres.

Even though the proton conductivity is modest, TiP_2O_7 exhibits a well-defined and relatively uniform water vapor dependency all the way down to very low $p(H_2O)$ at all temperatures investigated. This rather unique property makes the material an interesting candidate for conductivity based water vapor sensors.

IV. Summary

Undoped or nominally 2 mol-% Sc- and Fe-doped TiP_2O_7 have been synthesized and characterized with respect to structure, electrical properties, and water uptake thermodynamics by means of X-ray and neutron powder diffraction, impedance measurements, and thermogravimetry. The materials exist in a cubic superstructure at room temperature, which transforms into a simpler cubic structure at high temperature.

The conductivity increases with increasing water vapor pressure, and there is a clear H/D isotope effect, showing that protons are a major charge carrier. From the $p(O_2)$ dependence of the conductivity it has been concluded that n-type electronic conduction is important under reducing conditions and therefore that the material acts as a mixed conductor. The acceptor doping appears insignificant for the conductivity and defect structure. It remains unclear, however, whether this reflects incomplete dissolution - and in that case where and in what phase the excess exists – or whether the dissolved amount is in minority or has entered in a different way than assumed.

The $p(H_2O)$ and $p(O_2)$ dependencies have been modeled assuming that protons are charge compensated by oxygen interstitials and that the conductivity has contributions from protons and minority electrons. On this basis, the activation enthalpies of partial proton and electron conductivities have been determined.

From thermogravimetry versus temperature at constant $p(H_2O)$ = 0.1 atm the standard entropy and enthalpy of hydration into protons and oxygen interstitials in TiP_2O_7 were found to be −147 ± 6 J/mol K and −40 ± 4 kJ/mol, respectively, at low temperature and −185 ± 13 J/mol K and −77 ± 15 kJ/mol, respectively, at high temperature. By combining thermodynamics from thermogravimetry and conductivity the apparent enthalpy of proton migration was $\Delta H_{m,H+}$ = 79 ± 3 kJ/mol at 500−700 °C and 61 ± 5 kJ/mol at 700−1000 °C, while the apparent mobility pre-exponential was $\mu_{0,H+}$ = 470 ± 150 cm^2 K/Vs at low temperatures and 58 ± 30 cm^2 K/V s at higher temperatures.

Acknowledgements

The authors thank Dr. Laurent Jantsky, UiO for lattice parameter calculations. The PhD scholarship for V.N. has been granted by the FUNMAT@UiO program at the University of Oslo.

References

[1] H. Iwahara, T. Esaka, H. Uchida, and N. Maeda, "Proton Conduction in Sintered Oxides and its Application to Steam Electrolysis for Hydrogen Production," *Solid State Ionics*, **3-4**, 359-363 (1981).

[2]W. K. Lee, A. S. Nowick, and L. A. Boatner, "Protonic Conduction in Acceptor-Doped $KTaO_3$ Crystals," *Solid State Ionics*, **18-19**, 989-993 (1986).

[3]T. Norby and P. Kofstad, "Electrical Conductivity and Defect Structure of Y_2O_3 as a Function of Water Vapor Pressure," *J. Am. Ceram. Soc*., 67 [12] 786 -792 (1984).

[4]Y. Du and A. S. Nowick, "High-Temperature Protonic Conductors with Perovskite Related Structures," *Solid State Ionics*, **77**, 137-146 (1995).

[5]K. D. Kreuer, "Aspects of the Formation and Mobility of Protonic Charge Carriers and the Stability of Perovskite-type Oxides," *Solid State Ionics*, **125** [1-4] 285-302 (1999).

[6]S. M. Haile, D. A. Boysen, C. R. I. Chisholm, and R. B. Merle, "Solid Acids as Fuel Cell Electrolytes," *Nature (London)*, **410**, 910-913 (2001).

[7]T. Norby, M. Friesel, and B. E. Mellander, "Proton and Deuteron Conductivity in $CsHSO_4$ and $CsDSO_4$ by In Situ Isotope Exchange," *Solid State Ionics*, **77**, 105-110 (1995).

[8]A. Pawlowski and M. Polomska, "Fast Proton Conducting Hydrogen Sulphates and Selenates:Impedance Spectroscopy, Raman Scattering and Optical Microscope Study," *Solid State Ionics*, **176** [25-28] 2045-2051(2005).

[9]J. Otomo, N. Minagawa, C. Wen, K. Eguchi, and H. Takahashi, "Protonic Conduction in CsH_2PO_4 and its Composite with Silica in Dry and Humid Atmospheres," *Solid State Ionics*, **156** [3-4] 357-369 (2003).

[10]T. Norby and N. Christiansen, "Proton Conduction in Ca- and Sr-Substituted $LaPO_4$," *Solid State Ionics*, **77**, 240-243 (1995).

[11]K. Amezawa, H. Maekawa, Y. Tomii, and N. Yamamoto, " Protonic Conduction and Defect Structures in Sr-Doped $LaPO_4$," *Solid State Ionics*, **145** [1-4] 233-240 (2001).

[12]K. Amezawa, Y. Tomii, and N. Yamamoto, "High Temperature Protonic Conduction in $LaPO_4$ Doped with Alkaline Earth Metals,"*Solid State Ionics*, **176** [1-2] 135-141(2005).

[13]M. Nagao, T. Kamiya, P. Heo, A. Tomita, T. Hibino, and M. Sano, "Proton Conduction in In^{3+}-Doped SnP_2O_7 at Intermediate Temperatures," *J. Electrochem. Soc*., **153** [8] A1604-A1609 (2006).

[14]M. Nagao, A. Takeuchi, P. Heo, T. Hibino, M. Sano, and A. Tomita, "A Proton-Conducting In^{3+}-Doped SnP_2O_7 Electrolyte for Intermediate-Temperature Fuel Cells," *Electrochem. Solid-State Lett.*, **9** [3] A105- A109 (2006).

[15]A. Tomita, N. Kajiyama, T. Kamiya, M. Nagao, and T. Hibino, "Intermediate-Temperature Proton Conduction in Al^{3+}-Doped SnP_2O_7," *J.Electrochem. Soc.*, **154** [12] B1265-B1269 (2007).

[16]X. Sun, S. Wang, Z. Wang, X. Ye, T. Wen, and F. Huang, "Proton Conductivity of CeP_2O_7 for Intermediate Temperature Fuel Cells," *Solid State Ionics*, **179** [21-26] 1138-1141 (2008).

[17]Y. Li, T. Kunitake, Y. Aoki, and E. Muto, "Efficient, Anhydrous Proton-Conducting Nanofilms of Y-Doped Zirconium Pyrophosphate at Intermediate Temperatures," *Adv. Mater*., **20** [12] 2398-2404 (2008).

[18]V. Nalini, R. Haugsrud, and T. Norby, "High-Temperature Proton Conductivity and Defect Structure of TiP_2O_7," *Solid State Ionics*, **181** [11-12] 510-516 (2010).

[19]K. Amezawa, N. Takahashi, N. Kitamura, Y. Tomii, and N. Yamamoto, "High Temperature Protonic Conduction in $LaBO_3$ with the Aragonite-type Structure," *Solid State Ionics*, **175** [1-4] 575-579 (2004).

[20]N. Kitamura, K. Amezawa, Y. Tomii, and N. Yamamoto, "Protonic Conduction in Rare Earth Orthophosphates with the Monazite Structure," *Solid State Ionics*, **162-163**,161-165 (2003).

[21]B. H. Toby, "EXPGUI, A Graphical User Interface for GSAS," *J. Appl. Cryst*., **34** [2] 210-213 (2001).

[22]A. C. Larson and R. B Von Dreele, "General Structure Analysis System (GSAS)," Los Alamos National Lab. Report Laur, pp. 86-748 (2000).

[23]S. T. Norberg, G. Svensson, and J. Albertsson, "A TiP_2O_7 Superstructure," *Acta Cryst.*, **C57** [3] 225-227 (2001).

[24]R. C. Weast (Ed.), Handbook of Chemistry and Physics 69th ed., F-164, CRC Press, FL (1989).

[25]C. E. Bamberger and G. M. Begun, "Synthesis and Characterization of Titanium Phosphates, TiP_2O_7 and $(TiO)_2P_2O_7$," *J. Less-Common Metals*, **134** [2] 201-206 (1987).

[26]N. G. Chernorukov, M. I. Zhuk, and E. P. Moskvichev, "Thermal stability of disubstituted titanium phosphate monohydrate," *Tr. Khim. Tekh*., [3] 9-10 (1974).

[27]T. Norby, M. Widerøe, R. Glöckner, and Y. Larring, "Hydrogen in Oxides," *Dalton Trans*., [19] 3012-3018 (2004).

[28]T. Norby, "Perovskite Oxide for Solid Oxide Fuel Cells," T. Ishihara, ed., Springer, ISBN 978-0-387-77707-8, pp. 217-241 (2009).

[29]H. Fjeld, K. Toyoura, R.Haugsrud, and T. Norby, "Proton Mobility Through a Second Order Phase Transition:Theoretical and Experimental Study of $LaNbO_4$," *Phys. Chem. Chem. Phys*., DOI:10.1039/c002851g. (2010).

[30]Y. Larring and T. Norby, "Protons in $LaErO_3$," *Solid State Ionics*, **70-71**, 305-310 (1994).

[31]T. Oh, H. Yoon, and E. D. Wachsman, "Effect of Eu Dopant Concentration in $SrCe_{1-x}Eu_xO_{3-\delta}$ on Ambipolar Conductivity," *Solid State Ionics*, **180** [23-25]1233-1239 (2009).

Synthesis and electrical characterization of SnP_2O_7

Vajeeston Nalini, Laurent Jantsky, Reidar Haugsrud, Truls Norby

Manuscript.

V